CZECH TECHNICAL UNIVERSITY
IN PRAGUE

Faculty of Nuclear Sciences and Physical
Engineering
Department of Physics

Master's thesis

Production of charm mesons in STAR experiment

Bc. Zuzana Moravcová

Supervisor: doc. Mgr. Jaroslav Bielčík, PhD.
Consultant: Ing. Lukáš Kramárik

Prague, 2019

ČESKÉ VYSOKÉ UČENÍ TECHNICKÉ
V PRAZE
Fakulta jaderná a fyzikálně inženýrská
Katedra fyziky

Diplomová práce

Studium produkce půvabních mezonů v experimentu STAR

Bc. Zuzana Moravcová

Školitel: doc. Mgr. Jaroslav Bielčík, PhD.
Konzultant: Ing. Lukáš Kramárik

Praha, 2019

Prehlásenie:

Prehlasujem, že som svoju diplomovú prácu vypracovala samostatne a použila som len literatúru uvedenú v priloženom zozname.

Nemám závažný dôvod proti použitiu tohto školského diela v zmysle §60 Zákona č.121/2000 Sb., o práve autorskom, o právach súvisiacich s právom autorským a o zmene niektorých zákonov (autorský zákon).

V Prahe dňa

Název práce:
Studium produkce půvabných mezonů v experimentu STAR

Autor: Bc. Zuzana Moravcová

Obor: Experimentální jaderná a částicová fyzika
Druh práce: Diplomová práce

Vedoucí práce: doc. Mgr. Jaroslav Bielčík, Ph.D. Katedra fyziky, Fakulta jaderná a fyzikálně inženýrská, České vysoké učení technické v Praze
Konzultant: Ing. Lukáš Kramárik. Katedra fyziky, Fakulta jaderná a fyzikálně inženýrská, České vysoké učení technické v Praze

Abstrakt:
Štúdium kvark-gluónovej plazmy, hustej a horúcej jadrovej hmoty, v ktorej sa nachádzajú dekonfinované kvarky a gluóny, patrí medzi hlavné ciele Relativistického urýchľovača ťažkých jadier v Brookhavenskom národnom laboratóriu. Tento stav hmoty nemôžeme pozorovať priamo, ale len pomocou jeho prejavov ako je jadrový modifikačný faktor či eliptický tok. Nedávno sa však ukázalo, že azimutálne uhlové korelácie, ktoré sú v kvark-gluónovej plazme považované za prejav kolektívneho správania média, je možné merať aj v malých zrážkových systémoch ako p+p či p+Pb – je teda prítomný eliptický tok častíc. Preto je potrebné skúmať eliptický tok v malých systémoch a najmä určiť jeho pôvod, keďže zatiaľ nevieme, či v malých systémoch nemôže vzniknúť kvapôčka kvark-gluónovej plazmy, alebo ide len o korelácie nespôsobené kolektívnym správaním častíc.

V tejto práci bude predstavené meranie eliptického toku D^0 mezónu na experimente STAR v zrážkach d+Au pri energii $\sqrt{s_{\mathrm{NN}}} = 200$ GeV pomocou novej metódy Generic Framework. D^0 mezón je rekonštruovaný pomocou hadrónového rozpadu s použitím vylepšených rozhodovacích stromov, čo je algoritmus strojového učenia, v 3 intervaloch priečnych hybností: 1 – 2, 2 – 3 a 3 – 5 GeV/c so signifikanciou 5,18, 7,40 a 8,39. V rovnakých intervaloch bol taktiež vypočítaný eliptický tok tejto častice, a to 0,069, 0,204 a 0,530, avšak s veľkými nepresnosťami.

Klíčová slova: kvark-gluónová plazma, experiment STAR, pôvabné mezóny, eliptický tok, malé zrážkové systémy.

Title:
Production of charm mesons in STAR experiment

Author: Bc. Zuzana Moravcová

Specialization: Experimental nuclear and particle physics
Sort of project: Master's thesis

Supervisor: doc. Mgr. Jaroslav Bielčík, Ph.D. Department of Physics, Faculty of Nuclear Sciences and Physical Engineering, Czech Technical University in Prague
Consultant: Ing. Lukáš Kramárik. Department of Physics, Faculty of Nuclear Sciences and Physical Engineering, Czech Technical University in Prague

Abstract:
A study of quark-gluon plasma, the hot and dense nuclear matter made of deconfied quarks and gluons, is one of the main physics goals of the STAR experiment situated at the Relativistic Heavy-Ion Collider in the Brookhaven National Laboratory. As this state of matter cannot be observed directly, we use its signatures such as the nuclear modification factor or the elliptic flow to its examination. Recently, it has been shown that the elliptic flow considered to be a signature of collective behavior of the medium is measurable in small collision systems such as p+p or p+Pb as well. Therefore, it is important to investigate the elliptic flow in these systems and determine its origin as we do not know yet whether the it is caused by the presence of a quark-gluon plasma droplet.

This thesis is dedicated to the measurement of the elliptic flow of the D^0 meson in d+Au collisions recorded with the STAR experiment. The new method, Generic Framework, has been used for the flow analysis. The D^0 meson has been reconstructed via its hadronic decay channel using boosted decision trees, a machine learning algorithm which has been needed to suppress the significant combinatorial background. The reconstruction has been done in 3 bins of the candidate's transverse momentum: 1 – 2, 2 – 3 a 3 – 5 GeV/c with significance 5.18, 7.40, and 8.39, respectively. The same binning has been used for the elliptic flow calculation, the obtained result is 0.069, 0.204, and 0.530, however, with the large uncertainty.

Key words: quark-gluon plasma, STAR experiment, charm mesons, elliptic flow, small collision systems.

Acknowledgment

I would like to express my deepest gratitude to my supervisor, doc. Mgr. Jaroslav Bielčík, Ph.D. for his invaluable guidance on this thesis and on my whole research as a member of the STAR collaboration at the Czech Technical University in Prague.

My special thanks goes to my consultant, Ing. Lukáš Kramárik, for his advice, insightful comments, and friendly approach. Moreover, I would like to thank Ing. Katarína Křížková Gajdošová, Ph.D. and Ing. Vojtěch Pacík for their important help with troubles of the flow analysis.

I am grateful and happy to work in friendly and encouraging environment within the CTU and NPI teams of the STAR collaboration. A special thanks goes to the one and only team Hvězdička.

Additionally, I would like to thank the Department of Physics and the head of department, Ing. Martin Štefaňák, Ph.D., for providing a coffee machine in a student's room 13a. Our productivity would have been very limited without this device.

Finally, I would like to thank my family and friends for their endless support, especially to my parents who have been supporting my studies in Prague both emotionally and financially. It would not have been possible without you. Ďakujem.

Books and cleverness!
There are more important things
– friendship and bravery.

HERMIONE JEAN GRANGER

Contents

List of Figures

Introduction

This thesis is dedicated to the elliptic flow measurement of D^0 meson in d+Au collisions recorded with the STAR experiment in 2016. This topic is currently of a great interest as it has been shown that a strong collective flow, which has been observed in heavy-ion collisions and which is thought to originate from the presence of the quark-gluon plasma, can be measured in small collision systems as well, such as p+p or p+Pb. Thereore, it is very important to know where this flow comes from.

The first chapter introduces a reader to the quark-gluon plasma, the hot and dense medium in which quarks and gluons are no longer confied in hadrons. A short introduction of Standard model of particle physics is presented that summarizes elementary particles and forces. The phase diagram of nuclear matter which describes extreme conditions in which quark-gluon plasma occur is shown. The time-space evolution of the medium produced in a heavy-ion collision is presented. As the quark-gluon plasma cannot be observed directly, its signatures are explained once all variables important to their measurement are defined. Experimental results of multiple signatures are shown as well.

In the second chapter, the Brookhaven National Laboratory is introduced together with its facilities. The focus is on Relativistic Heavy Ion Collider complex, including all pre-acceleration phases from an ion source until a heavy ion gains its final energy. Subsequently, the only detector that currently takes data from RHIC, the STAR experiment, is presented. Three of its subdetectors – Heavy Flavor Tracker, Time Projection Chamber, and Time of Flight detector which are used in the analysis presented later in this thesis are described in detail.

As this thesis focuses on D mesons, the summary of their measurements in Au+Au collisions is presented in the third chapter. The reconstruction is described detailedly as it is very similar to the one presented in the analysis part of this work. Subsequently, two of quark-gluon plasma signatures are shown for these particles – the nuclear modification factor and the elliptic flow.

Finally, the fourth and last chapter of this thesis is dedicated to the measurement of elliptic flow of D^0 meson in d+Au collisions. The reconstruction of this particle was done using boosted decision trees, which is a machine learning algorithm used for gaining a higher particle yield or purity of the signal. The algorithm is described as well as its usage on experimental data. The elliptic flow is calculated using Generic Framework with multi-particle azimuthal correlation method. Individual steps are described in detail. At the end of the chapter, the result of this measurement is shown.

Statement of author's contribution

I have joined the STAR collaboration in 2016 as a student of the Czech Technical University in Prague under the supervision of doc. Mgr. Jaroslav Bielčík, Ph.D. A part of my bachelor and later on the research thesis was the reconstruction of $D^{\pm}$ meson in Au+Au collisions using multivariate data analysis techniques. This was one of the very first attempts of using machine learning algorithms in heavy flavor analyses which have became very popular. I have implemented Boosted decision trees from TMVA package within the ROOT framework in order to obtain higher significance in the reconstruction of $D^{\pm}$ meson. Until that moment, only unoptimized rectangular cuts were used for the reconstruction of $D^{\pm}$ meson in the STAR collaboration.

My diploma thesis is dedicated to the measurement of charm quark elliptic flow of D^0 meson in d+Au collisions recorded in the STAR experiment in 2016. In general, flow in small systems is one of the hottest topics of today's heavy-ion physics. The reconstruction of D^0 meson in d+Au collisions has been done in close collaboration with the consultant of this work, Ing. Lukáš Kramárik. I have written the software for the flow analysis using Generic framework as a first in heavy flavor physics working group in STAR. Moreover, I have presented results of this work, measurement of the elliptic flow of D^0 meson, at the STAR Collaboration Meeting in the Brookhaven National Laboratory in March 2019.

Furthermore, I have helped to develop the software for Roman Pots sub-system during a summer internship in Brookhaven National Laboratory in August 2017. As a member of the collaboration, I have taken shifts (2 weeks in both April 2018 and March 2019), where my main responsibility was checking the quality of the detector operation during the data

acquisition.

Besides STAR related activities, I have joined the CERN Summer Student Programme in summer 2018. My project has been dedicated to the analysis of cosmic rays with the Time Of Flight detector at the ALICE experiment. I have examined the time resolution in different levels of granularity with a goal of identifying potentially miscalibrated channels.

Chapter 1

Quark-gluon plasma

The following chapter describes the production and properties of the quark-gluon plasma. At the beginning, a summary of the elementary particles and fundamental forces is presented as an introduction to the selected topic. When heavy-ions collide, a hot and dense matter, the quark-gluon plasma, is produced. The production mechanism is described together with the time-space evolution of the hot matter. Subsequently, variables used in high-energy physics analysis are presented as these will be needed later on. Finally, as the QGP cannot be observed directly, its signatures are presented including the interaction of heavy quarks with the matter.

1.1 Standard Model

The matter around us is made up of molecules which are themselves made up of atoms. Every atom consists of a nucleus and an electron shell surrounding it. The nucleus contains nucleons, protons and neutrons. Nucleons, unlike the electron, which is an elementary particle, are composite bodies, made up of quarks and gluons. The proton is made from two u quarks and one d quark[1]. The aforementioned particles (the electron, u quark and d quark) along with the electron neutrino are the elementary particles of the first generation of the

[1]Besides three valence quarks, the proton consists of sea quarks and gluons.

generation	I	II	III
quark	u	c	t
	up	charm	top
mass [MeV/c^2]	$2.2^{+0.4}_{-0.5}$	$1\ 275^{+25}_{-35}$	$173\ 000^{+400}_{-400}$
electric charge [e]	2/3	2/3	2/3
quark	d	s	b
	down	strange	bottom
mass [MeV/c^2]	$4.7^{+0.5}_{-0.3}$	95^{+9}_{-3}	$4\ 180^{+40}_{-30}$
electric charge [e]	-1/3	-1/3	-1/3
lepton	e	μ	τ
	electron	muon	tau
mass [MeV/c^2]	0.5109989461(31)	105.6583745(24)	1 776.86(12)
electric charge [e]	-1	-1	-1
lepton	ν_e	ν_μ	ν_τ
	electron neutrino	muon neutrino	tau neutrino
mass [eV/c^2]	< 2	$< 0.19 \cdot 10^6$	$< 18.2 \cdot 10^6$
electric charge [e]	0	0	0

Tab. 1.1: Elementary particles – fermions. Spin of all listed fermions is $1/2\ \hbar$. Electric charge is a fraction of elementary charge e, $e = 1.602 \cdot 10^{-19}$ C [1].

Standard Model. Their charges and masses are in Table 1.1. In general, six types (flavors) of quarks exist, all of them with their properties are also in Tab.1.1.

At normal temperatures and densities[2], quarks cannot exist by themselves, they have to be confined within a hadron. A hadron, which is the collective term for a bound state of quarks, has two subcategories: a baryon (made from three quarks) and a meson (made from a quark and an antiquark). Every quark possesses the color charge (red, green or blue), consequent hadron is always color neutral ("white").

A quark from the second or third generation carries a quantum number related to its flavor, e.g. strange quark has strangeness ($S = -1$), charm quark has charm ($C = 1$), and so on. When a meson is made of a quark and an antiquark of the same flavor, we call the flavor hidden (e.g. J/ψ particle, made from $c\bar{c}$ pair, is a hidden charm meson). On the other

[2]The energy density in normal nuclear matter at zero temperature is ≈ 0.16 GeV/fm^3 (nucleon at rest) [2].

hand, when a particle has an anti-symmetric number of quarks and anti-quarks, we call it open flavor hadron (D^+ made from $c\bar{d}$ or Λ_c made from udc are open charm hadrons).

Collectively, particles with at least one heavy quark (c, b) are called heavy flavor particles. These cannot be observed directly as they decay very quickly. Therefore, we can only observe their decay products made from light quarks (u, d, s).

Particles are interacting with each other thanks to the fundamental forces, three of which are included in the Standard Model (SM). In the SM, the forces are carried by four types of force carriers (gauge bosons) with spin 1. The carrier of electromagnetic interaction described in quantum electrodynamics (QED) is the photon which is massless[3] and has zero electromagnetic charge. The gauge bosons of the strong interaction (quantum chromodynamics (QCD)) are gluons. These are also massless and electric-charge neutral, but they carry a color-charge. In addition to the color-charge, they carry also a different anti-color-charge. Quarks inside a hadron exchange gluons which are the reason for their confinement. Gluons carry almost the half of the proton momentum [2]. The strong interaction is approx. 10^2 times stronger than the electromagnetic one at the short distance, however, its range is very limited. The exchange of gluons between tightly packed protons is the reason why they are stable in the nucleus of an atom and are not repelled due to electromagnetic forces.

The carriers of weak interactions are $W^{\pm}$ and Z^0 bosons. While Z^0 is electrically neutral, W has charge 1 or -1. Their masses are $m_W = 80.379 \pm 0.012$ GeV/c^2 [1] and $m_Z = 91.1876 \pm 0.0021$ GeV/c^2 [1]. Since both are very heavy, only their decay products are observed.

The last particle of the SM is Higgs boso, with mass $m_H = 125.09 \pm 0.21 \pm 0.11$ GeV/c^2 [1] discovered in 2012 at experiments ATLAS and CMS in CERN. The Higgs boson is an excitation of the Higgs field. This field provides the mechanism by which the masses of particles are attained in the SM. It also describes the mass difference between massless photon and heavy W and Z bosons considering the unification of the electromagnetic and the weak interaction into the electroweak interaction.

[3]More precisely, the mass of photon is experimentally determined to be $< 10^{-18}$ eV/c^2 [1].

1.2 Quark-gluon plasma

When we put the matter in the extreme conditions, such as very high temperature (order of magnitude of 100 MeV) or very high densities (order of magnitude GeV/fm^3), hadrons dissolve into the quark-gluon plasma (QGP) as shown on phase diagram of nuclear matter in Fig. 1.1. Normal nuclear matter is situated in low temperature region ($T \approx 0$ eV) with baryon chemical potential $\mu_B = 0.93$ GeV [3]. The high density phase (low temperature, very high baryon chemical potential) is expected to be in the interior of neutron stars [2]. Heated-vacuum quark-matter phase (very high temperature, low baryon chemical potential) was produced at the Big Bang. Currently it can be produced at particle accelerators. Two types of phase transition occur between the hadronic gas and the QGP – the crossover and the first order transition. The former appears at rather high temperature and low baryon chemical potential while the latter with a discontinuity in energy density describes the behavior for rather lower energies and higher baryon chemical potential. The point in the phase diagram where two curves of phase transition meet is called the critical point, its coordinates are $\mu_B \approx 440$ MeV, $T_c \approx 170$ MeV.

1.2.1 Production of QGP

The new type of matter which consists of deconfined quarks and gluons and which behaves as a strongly interacting liquid can be artificially created in central heavy-ion collisions. The study of its properties, including the geometry of the phase transition lines and the exact position of the critical point, is the main focus of research conducted at the STAR experiment at the Relativistic Heavy Ion Collider (RHIC) and at the ALICE experiment at Large Hadron Collider (LHC). RHIC accelerator which is described in detail in section 2.2, has a special programme (Beam Energy Scan (BES)) to study the phase transition of nuclear matter. Chosen collision energies (down to 7.7 GeV) produced in Phase I are illustrated also in Fig. 1.1. Corresponding baryon chemical potentials are shown in Tab. 1.2.

The Phase II of Beam Energy Scan programme is scheduled to years 2019 and 2020. As

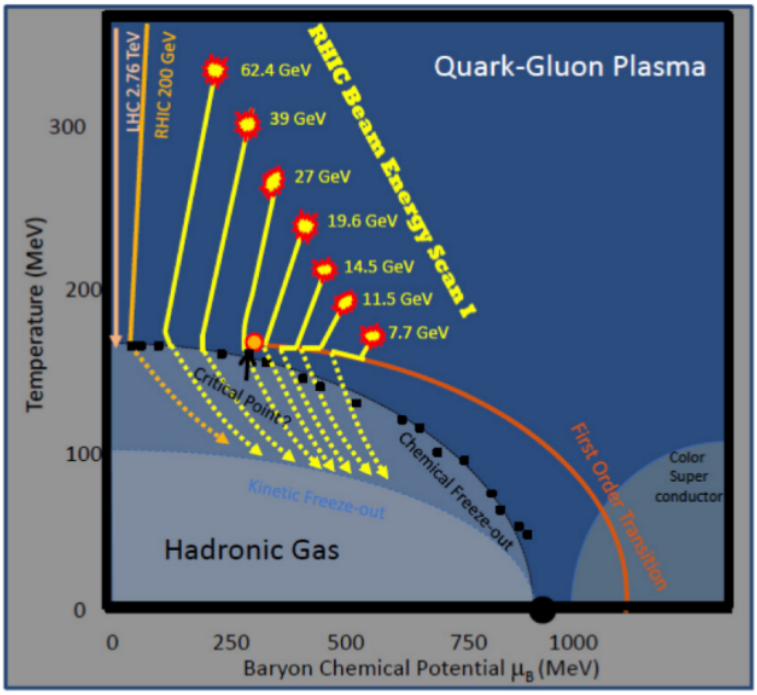

Fig. 1.1: Phase diagram of nuclear matter. Taken from [4].

$\sqrt{s_{\mathrm{NN}}}$ [GeV]	μ_B [MeV]
19.6	585
15.	625
11.5	670
7.7	720

Tab. 1.2: Centre of mass collision energy of Au+Au collision per nucleon pair $\sqrt{s_{\mathrm{NN}}}$ and corresponding baryon chemical potential μ_B created during the Beam Energy Scan programme Phase I at RHIC. Taken from [4].

the luminosity in collider mode of RHIC would not have been sufficient, the measurement in the area below 7.7 GeV (down to 3.0 GeV) will be obtained using the fixed Au target[4]. All energies of BES Phase II with corresponding baryon chemical potentials are listed in Tab. 1.3.

The time-space evolution of an ultrarelativistic heavy-ion collision is shown in Fig. 1.2, where z is the position along the beam axis (in the direction of initial movement of ions)

[4]In a collision of two identical particles with energy E, the centry of mass energy is $\sqrt{s_{\mathrm{NN}}} = 2E$. In fixed target experiment, $\sqrt{s_{\mathrm{NN}}} \approx \sqrt{2Em}$, where m is the mass of target particle.

$\sqrt{s_{\mathrm{NN}}}$ [GeV]	μ_B [MeV]	mode
19.6	205	collider
14.5	260	collider
11.5	315	collider
9.1	370	collider
7.7	420	collider
7.7	420	fixed target
6.2	487	fixed target
5.2	541	fixed target
4.5	589	fixed target
3.9	633	fixed target
3.5	666	fixed target
3.2	699	fixed target
3.0	721	fixed target

Tab. 1.3: Collision energy per nucleon pair $\sqrt{s_{\mathrm{NN}}}$ and corresponding baryon chemical potential μ_B created during the Beam Energy Scan programme Phase II at RHIC. Taken from [5].

and t is the time coordinate. Thanks to the relativistic effects, nuclei are contracted in the longitudinal direction, so they are colliding (in point $(z, t) = (0, 0)$) in the shape of thin disks.

Right after the collision the pre-equilibrium phase occurs and in the time $t \approx 1$ fm/c $= 3 \cdot 10^{-24}$ s after the collision quark-gluon plasma is created and local thermodynamic equilibrium is settled. Since the QGP has properties of a perfect liquid, the system in this stage and its evolution can be described by the relativistic hydrodynamic, more precisely the equation of state of the flowing matter [2]. Medium is expanding and cools down below the critical temperature T_c. The system reaches a state where the hydrodynamic description cannot be used anymore. The process of hadronization begins and quarks and gluons are being confined into hadrons.

After those processes, approximately after 10 fm/c after the collision, the chemical freeze-out occurs and inelastic collisions stop. Subsequent kinetic (also called thermal) freeze-out is taking place when elastic collisions cease as well. Created particles continue towards the detector where they are detected in the first detector at time $t \approx 4$ cm/c [6]. If a particle is too short-lived to pass all the way to the detector, only its decay products are detected.

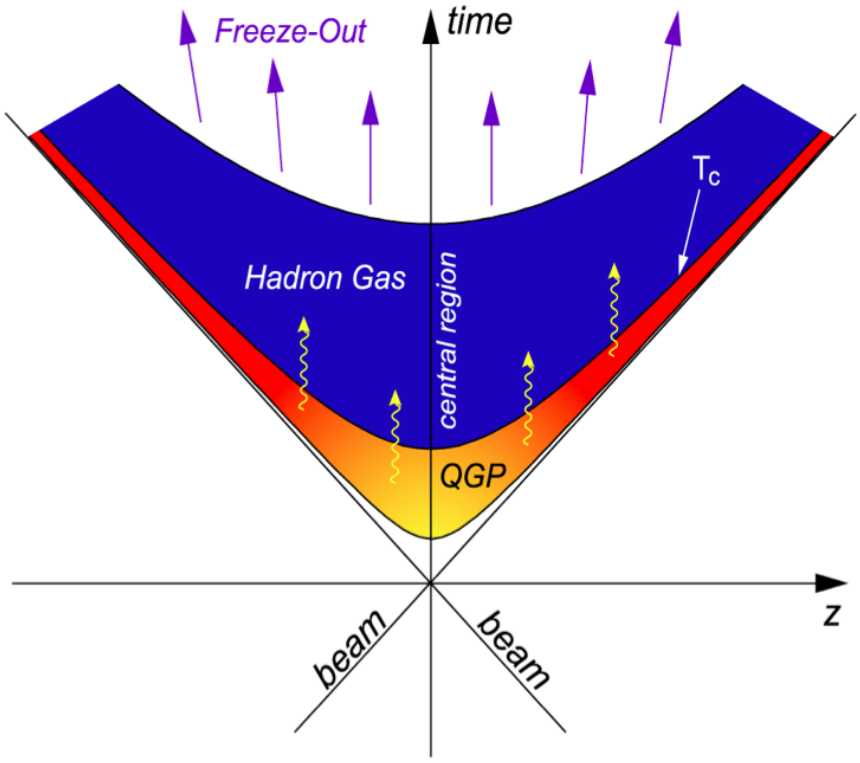

Fig. 1.2: Time-space evolution of an ultrarelativistic heavy ion collision. Taken from [7].

1.2.2 Variables used to study QGP

As is obvious from previous section, QGP cannot be observed directly. However, there are several phenomena connected with the production of QGP, such as jet quenching or collective flow of particles. To describe them, some variables need to be defined first.

First of all, particles in a collider are moving along z axis with almost speed of light. Therefore, we use transverse momentum $p_{\mathrm{T}} = \sqrt{p_x^2 + p_y^2}$, the component of momentum in the plane perpendicular to the initial movement of heavy ions, which is Lorentz invariant.

The center of mass energy, denoted $\sqrt{s}$, is the total energy available in collision experiment (in the center of mass frame). In heavy-ions experiments, we use $\sqrt{s_{\mathrm{NN}}}$, which is the center of mass energy per colliding nucleon pair.

Pseudorapidity describes the direction of the motion of the particle relative to the beam

axis as

$$\eta = -\ln\left[\tan\left(\frac{\theta}{2}\right)\right], \tag{1.1}$$

where θ is the angle between particle momentum $\vec{p}$ and the positive direction of the z axis. The illustration of the dependence of η at θ is shown in Fig. 1.3.

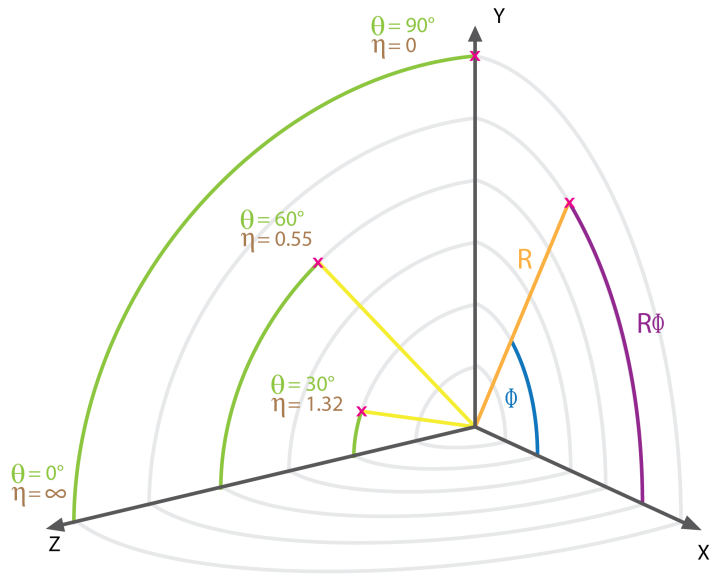

Fig. 1.3: Pseudorapidity η dependence on the angle θ between the momentum and the positive direction of the beam axis. Taken from [8].

Moreover, one needs to consider the size of the region of the nuclei overlap in the time of collision. Based on this, we classify collisions into several centrality classes. So called central collisions, or more precisely 0-10 % most central collisions, are when nuclei are colliding head to head. We can define an impact parameter b as a distance between the centers of colliding nuclei measured in plane perpendicular to the beam axis. Then for central collisions $b \sim 0$ fm. With increasing b, we note collisions semi-central (10-40 %) and subsequently semi-peripheral (40-70 %). When $b \sim 2R$, but still $b < 2R$, where R is the radius of colliding nucleus, we denote peripheral collisions (70-80 % most central collisions), and finally, when $b > 2R$, we speak about ultra-peripheral collisions.

A schematic view of a heavy-ion collision is shown in Fig. 1.4. On the left, the state

before the collision is shown, where heavy ions are Lorentz contracted[5], together with the impact parameter b. On the right, the state after collision is displayed. Nucleons that have collider at least once are called participants, others are called spectators.

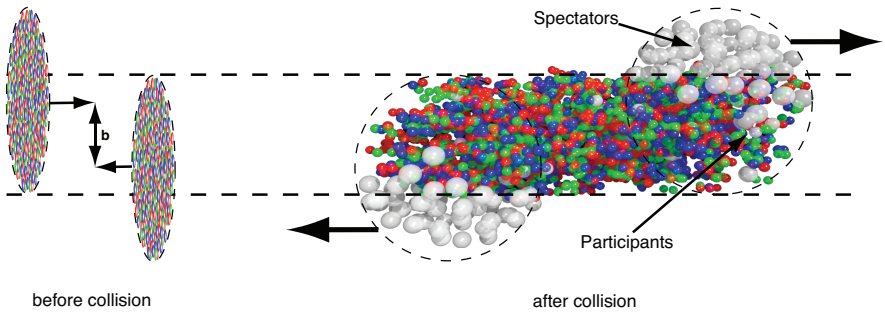

Fig. 1.4: Schematic view of a heavy ion collision. (Left:) Heavy ion just before collision, b is the impact parameter. (Right:) After collision, visualization of participants and spectators. Taken from [9].

Cross section of a collision as a function of multiplicity, number of produced charged particles, is shown in Figure 1.5, as well as classes of centrality and number of participants. As it is clear from the figure, the more collision is central, the more particles are produced.

Finally, luminosity is a characteristic property of a particle accelerator defined as

$$L = \frac{1}{\sigma} R, \tag{1.2}$$

where σ is the cross section and R is a reaction rate. For instance, the average luminosity in RHIC (Relativistic Heavy-Ion Collider) in 2016 was $L = 87 \cdot 10^{26}$ cm^{-2} s^{-1} [11]. The goal at this accelerator after 2021 is $L = 175 \cdot 10^{26}$ cm^{-2} s^{-1}. After integrating luminosity over a time period one can compare a performance of different accelerators. The integrated luminosity for different RHIC runs is shown in Tab. 2.1.

[5]In RHIC, Au nuclei are accelerated to the energy per nucleon 100 GeV. Unified atomic mass unit is u = 931.494 061(21) MeV/c^2 [1]. Then gamma factor, deduced from the formula $E = m\gamma c^2$ is ~ 107.35. We can derive from the definition of $\gamma = 1/\sqrt{1-v^2/c^2}$ that Au nuclei are moving with velocity $\sim 0.9999566\ c$. The atomic number of gold is $A = 197$, therefore we can deduce the radius of Au as $R = r_0 \sqrt[3]{A} = 6.98$ fm, where $r_0 = 1.2$ fm is proportionality constant. In xy plane, the diameter of Au nucleus is 13.96 fm while along the z axis, the diameter is $2R/\gamma = 0.13$ fm.

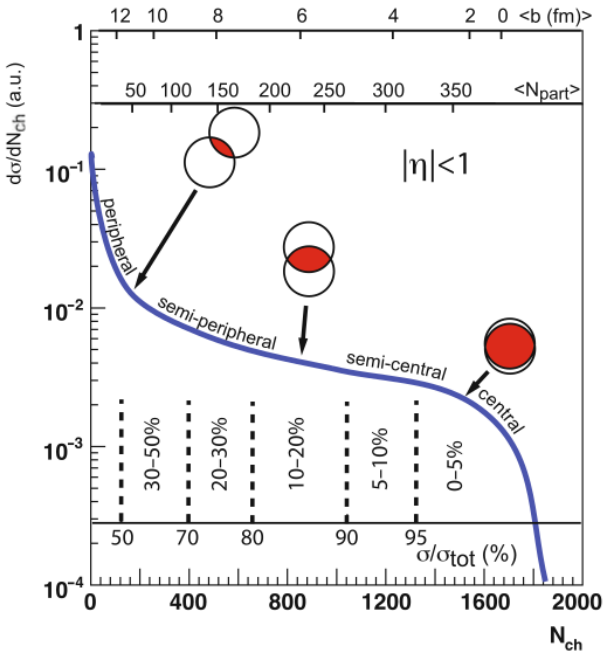

Fig. 1.5: Distribution of $^{d\sigma}/_{dN_{ch}}$ of a collision as a function of multiplicity with illustrated classes of centrality. Taken from [10].

1.2.3 Interactions of heavy quarks with matter and signatures of QGP

In proton-proton collisions, two back-to-back partons may be produced and subsequently hadronize to two jets with the same momentum (with an opposite direction). However, in heavy-ion collisions, especially in central ones, we can observe so called dijet asymmetry – one jet disappears, or has significantly smaller energy, or is much broader. This phenomenon, known as jet quenching, is explained by the fact that the fast parton produced in the initial hard scattering processes has to travel through medium (QGP). Therefore, it interacts with this hot and dense state of matter. As the total energy has to be conserved, the medium gains the energy lost by the parton. It is possible to observe this phenomena in two-particle azimuthal distribution that is shown in Fig. 1.6 for different collisions systems. While a back-to-back peak is present in small systems (p+p, d+Au), one of jest is significantly suppress in central Au+Au collisions.

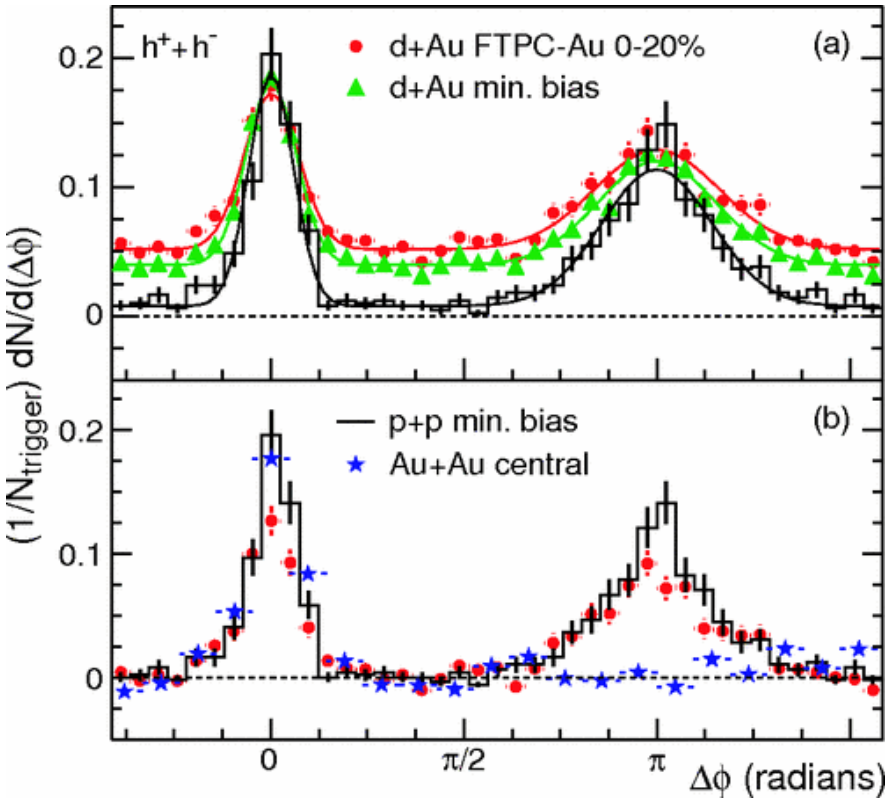

Fig. 1.6: Two-particle azimuthal distribution for p+p, d+Au, and Au+Au collisions at the STAR experiment. Only charged hadrons within $|\eta| < 0.7$ are shown. Taken from [12].

The interaction can be radiative or collisional – the former stands for radiating a gluon within the medium, the latter is for elastic scattering with other partons that are in the medium [2]. The collisional energy loss dominates in low energy region while the radiative energy loss is dominant for higher energies. Value of the energy where these two losses are equal is known as the critical energy E_c, e.g. $E_c = 19.42$ MeV for electron in copper [1].

However, the energy loss is different for heavy and light quarks as the gluon radiation is suppressed at $\theta < {}^{m}/_{E}$, where θ is angle between directions of the quark and the gluon, m is a mass of quark and E is its energy. This phenomenon is known as a dead-cone effect [13].

Moreover, the observed phenomenon of jet quenching depends on the location of produced partons with respect to the medium. Partons produced closed to the surface can still hadronize as two back-to-back jets. However, if one of two partons needs to pass a larger

path within the QGP, final-state jets may have different momentum and might be broader. A single jet is observed in a case when one of the partons lose all of the energy within the medium.

Another probe of existence of QGP, similar to previous one, is a study of particle yields. To compare those variables in proton (pp) or nuclei (AA) collisions, we define nuclear modification factor as

$$R_{\mathrm{AA}} = \frac{1}{\langle N_{bin} \rangle} \frac{\frac{\mathrm{d}N}{\mathrm{d}p_{\mathrm{T}}}|_{\mathrm{AA}}}{\frac{\mathrm{d}N}{\mathrm{d}p_{\mathrm{T}}}|_{\mathrm{pp}}}, \tag{1.3}$$

where $\frac{\mathrm{d}N}{\mathrm{d}p_{\mathrm{T}}}|_{\mathrm{AA}}$ and $\frac{\mathrm{d}N}{\mathrm{d}p_{\mathrm{T}}}|_{\mathrm{pp}}$ are particle yield in AA and pp collision, respectively. The ratio is scaled with mean value of binary collisions in heavy ion collision, $\langle N_{bin} \rangle$. Since particle yield varies significantly for different classes of centrality, it is useful to obtain R_{AA} independently for each class. Nuclear modification factor of D^0 meson for three centralities (0-10 %, 10-40 %, and 40-80 %) is shown in Figure 1.7. The data are from Au+Au collisions at STAR experiment at $\sqrt{s_{\mathrm{NN}}} = 200$ GeV.

The suppression the particle production is shown in 3 centrality classes (0-10 %, 10-40 %, and 40-80 %), and it is most significant in the 0-10 % of most central collisions. The suppression is very strong in low-p_{T} region ($R_{\mathrm{AA}} \approx 0.4$ for $p_{\mathrm{T}} = 1$ GeV/c), then in mid-p_{T} it raises until it peaks at $p_{\mathrm{T}} \approx 3$ GeV/c with $R_{\mathrm{AA}} \approx 0.7$. Subsequently, R_{AA} starts to fall again towards its minimum which is reached at $p_{\mathrm{T}} = 8$ GeV/c with $R_{\mathrm{AA}} \approx 0.2$.

The reconstruction was done on two different data sets – one from year 2014, another from a combination of years 2010 and 2011. The main difference is that in 2014, the Heavy Flavor Tracker detector was installed, which has significantly improved the tracking capability of the STAR detector. This sub-detector has helped reconstruct the secondary vertex as well which is crucial for heavy flavor oriented analyses. Therefore one can see the uncertainty of R_{AA} from 2014 is much smaller compared to 2010/2011 data-taking campaign.

The comparison of nuclear modification factor of D^0 meson can be made with data recorded with the ALICE experiment. In Fig. 1.8, R_{AA} of D mesons (D^0, D^+ and D^{*+}) in Pb-Pb collisions at $\sqrt{s_{\mathrm{NN}}} = 2.76$ TeV is shown for two different centrality classes. One can observe that the biggest suppression of particle production (the minimum value of R_{AA})

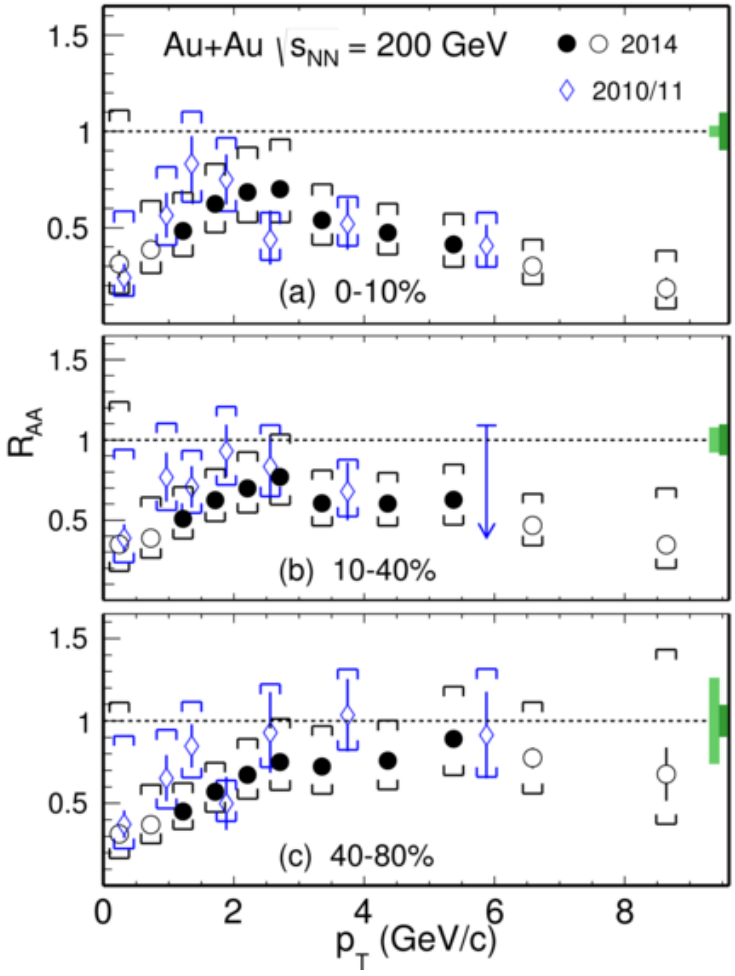

Fig. 1.7: Nuclear modification factor of D^0 for different centrality classes. Taken from [14].

is observed in the most central collision around $p_{\mathrm{T}} = 8$ GeV/c with the value of $R_{\mathrm{AA}} \sim 0.14$. With increasing p_{T}, R_{AA} slowly increases towards $R_{\mathrm{AA}} \sim 0.3$ for $p_{\mathrm{T}} = 30$ GeV/c. The particle production is less suppressed in semi-peripheral collisions.

We can also observe suppression of quarkonia, $c\bar{c}$ $(J/\psi, \psi')$ or $b\bar{b}$ $(\Upsilon, \Upsilon', \Upsilon'')$ mesons produced in hard processes. Quarkonia are a special type of mesons made of c or b quark and the antiquark of the same flavor, therefore there are among the heaviest mesons. Those particles are bound very strongly, and their radii are much smaller than those of other mesons.

The binding radius r_B of quarkonium is really important as it has a strong connection with

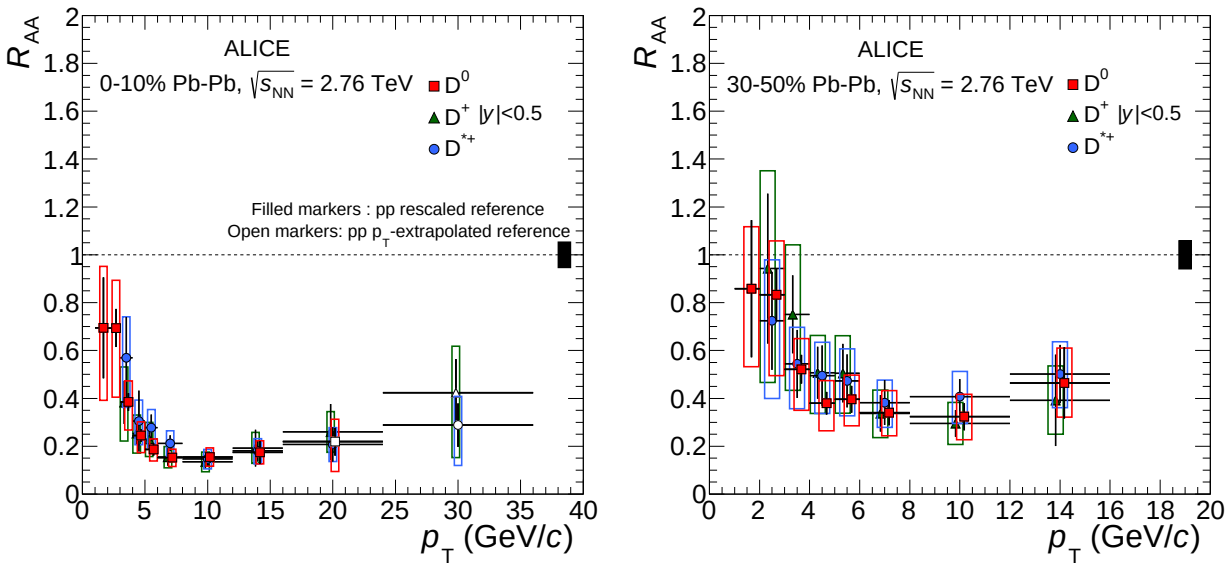

Fig. 1.8: Nuclear modification factor R_{AA} of D mesons (D^0, D^+ and D^{*+}) in Pb-Pb collisions at $\sqrt{s_{\mathrm{NN}}}$ = 2,76 TeV for two collision centrality classes. Taken from [15].

the "melting" temperature of this particle. In general, the deconfinement can be explained with the Debye screening of the quark color charge [16], the screening radius r_D is a decreasing function of temperature. For $r_D < r_B$, the confining (strong) force cannot hold quarks together anymore. As it was already said, the radius of quarkonium is smaller compared to the one of other mesons. Therefore higher temperatures might be needed to their dissociation. Their break up temperatures are e.g. $2.1T_c$ for J/ψ or $> 4T_c$ [17]. For their excited states, the dissociation temperatures are much closer to the critical temperature, e.g. $T_D = 1.16T_c$ for χ_c(1P). We can also deduce the temperature of the quark-gluon plasma by measuring the suppression of the different states.

Last but not least, QGP droplet is expanding very quickly after the heavy-ion collision which causes a collective motion of particles – flow. In central collisions, we can observe radial flow, caused by isotropic expansion, which affects the shape of particle spectra at low p_{T} by slightly increasing p_{T} of particles. This effect is larger for protons than for kaons which is larger than for pions. Mass dependency is observed in Fig. 1.9.

After high-energy heavy-ion non-central collision, particles are pushed out of the system

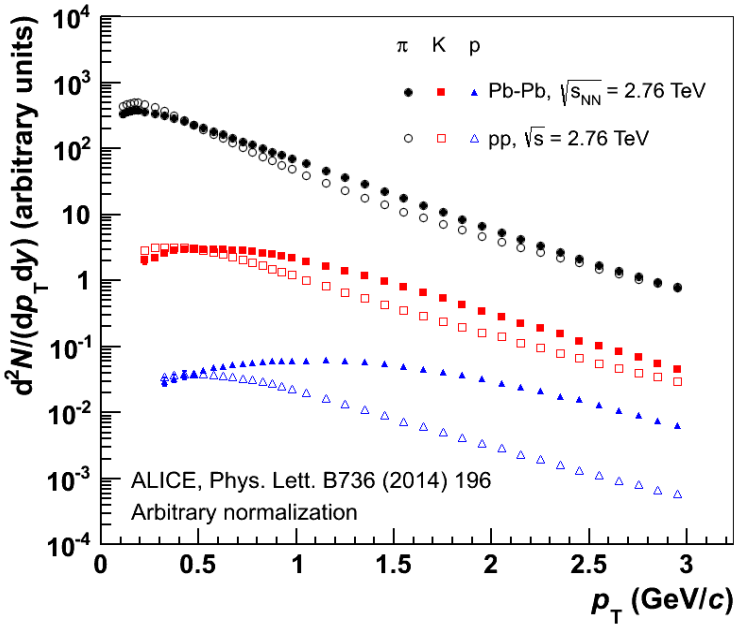

Fig. 1.9: Particle spectra as a function of p_{T} for protons, kaons and pions for two different collision systems. The radial flow caused by the QGP affects the shape of the spectra. Taken from [6].

in a preferred direction as the overlap of colliding nuclei is anisotropic (almond-like shape as shown in Fig. 1.10). This phenomenon is caused by the difference of pressure gradients – the one in xz plane is larger than in y direction. This spatial initial anisotropy is converted into momentum-space one which is measurable. Anisotropic flow is defined by coefficients v_n in the Fourier expansion of the azimuthal dependence of the invariant yield with respect to the reaction plane:

$$E\frac{\mathrm{d}^3N}{\mathrm{d}^3p} = \frac{1}{2\pi}\frac{\mathrm{d}^2N}{p_{\mathrm{T}}\mathrm{d}p_{\mathrm{T}}\mathrm{d}y}\left(1+\sum_{n=1}^{\infty}2v_n\cos(n(\phi-\Psi_R))\right), \tag{1.4}$$

where E, p_{T}, y and ϕ are energy, transverse momentum, rapidity and azimuthal angle of particle, respectively, and Ψ_R the reaction plane defined by the impact vector and initial movement of nuclei (xz plane in Fig. 1.10). Several coefficients (harmonics) v_n have specific names, such as directed (v_1) or elliptic flow (v_2). They quantitatively express the collective

expansion of the produced medium [18].

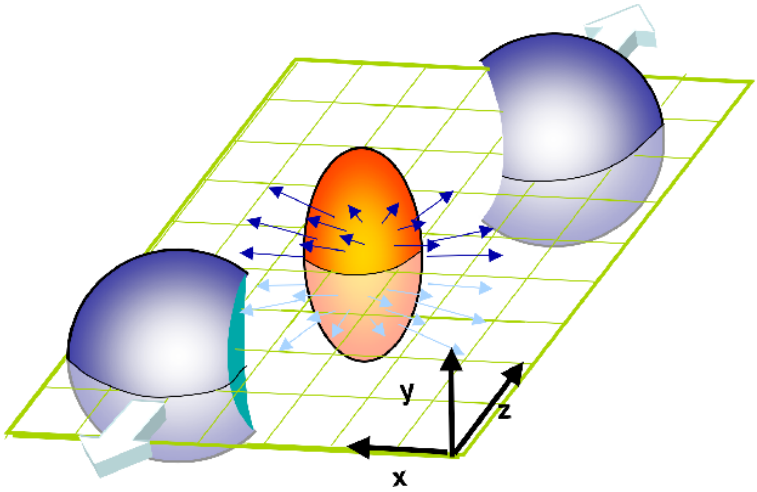

Fig. 1.10: Heavy-ion non-central collision. The reaction plane is shown in green. Taken from [19].

The elliptic flow of charged hadrons in Pb+Pb collisions at ALICE at $\sqrt{s_{\mathrm{NN}}} = 2.76$ TeV and in Au+Au collisions at STAR at $\sqrt{s_{\mathrm{NN}}} = 200$ GeV for three different collision centrality classes is shown in Figure 1.11. It can be seen that the flow coefficient decreases towards central collisions. This measurement also indicates that charm quark participates in the collective expansion of the system.

Moreover, the elliptic flow is shown in Fig. 1.12 for three different small collision systems – p+Au, d+Au, and ^{3}He+Au. All collisions are central at $\sqrt{s_{\mathrm{NN}}} = 200$ GeV recorded with the PHENIX experiment. The flow is measured for charged pions and for protons and antiprotons within $|\eta| < 0.35$ and compared to hydrodynamic calculations using the superSONIC model. In all three collision systems, the mass ordering is visible in $p_{\mathrm{T}} < 1.5$ GeV/c – heavier protons have smaller elliptic flow coefficient v_2 than pions. In p+Au collisions, the data and model are in a very good accordance for both protons and pions, the flow is comparable for both particles. Once a deuteron substitutes a proton in the collision, the model describes data only in low p_{T} region ($p_{\mathrm{T}} < 1.5$ GeV/c). In higher p_{T}, a hint of baryon-meson grouping is visible, however, the uncertainity is rather high. In ^{3}He+Au, the baryon-meson grouping is clear, but the model does not describe the elliptic flow of pions.

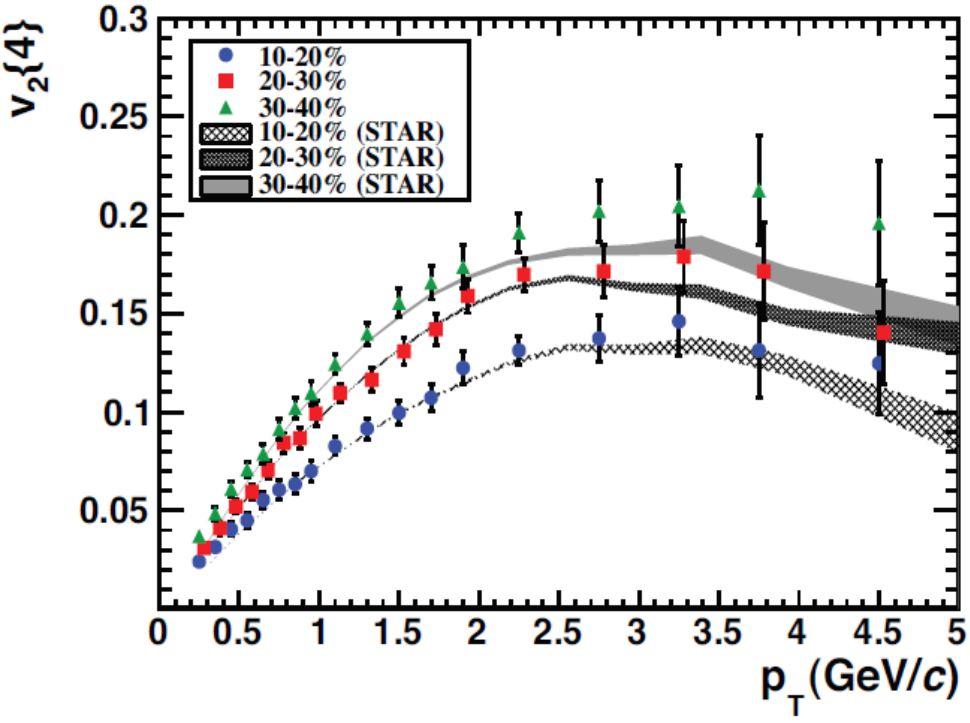

Fig. 1.11: Differential elliptic flow of charged hadrons for three different collision centrality classes. Colored symbols are data from Pb+Pb collisions at ALICE at $\sqrt{s_{\mathrm{NN}}}$ = 2,76 TeV, grey lines are from Au+Au collisions at STAR at $\sqrt{s_{\mathrm{NN}}}$ = 200 GeV. Taken from [20].

The elliptic flow of μ created from open heavy flavor decays ($c+b \to \mu$) in central (0-20%) d+Au collisions at $\sqrt{s_{\mathrm{NN}}} = 200$ GeV at the PHENIX experiment is shown in Fig. 1.13. The measurement was done in forward and backward region and is similar to the elliptic flow of charged hadrons. Both shown measurements indicate a non-zero flow of heavy flavors in small collision systems.

Besides these effects, additional ones are present – cold nuclear matter (CNM) effects, induced by the presence of nuclei in the initial-state [23]. They can be studied in proton-nucleus (pA) or deuteron-nucleus (dA) collisions. It is not possible to observe them in heavy-ion collisions as medium effects are much stronger. CNM effects can be quantified e.g. by nuclear modification factor R_{pA}, R_{dA}.

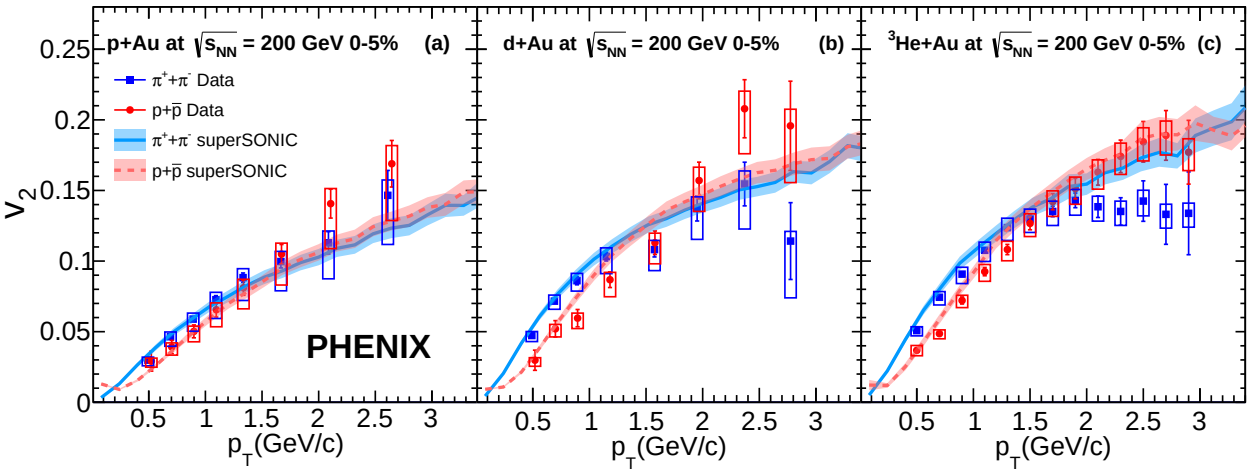

Fig. 1.12: Elliptic flow of pions and protons in p+Au, d+Au, and ^{3}He+Au collisions at $\sqrt{s_{\rm NN}}$ = 200 GeV at the PHENIX experiment compared with hydrodynamic calculations using the superSONIC model. Taken from [21].

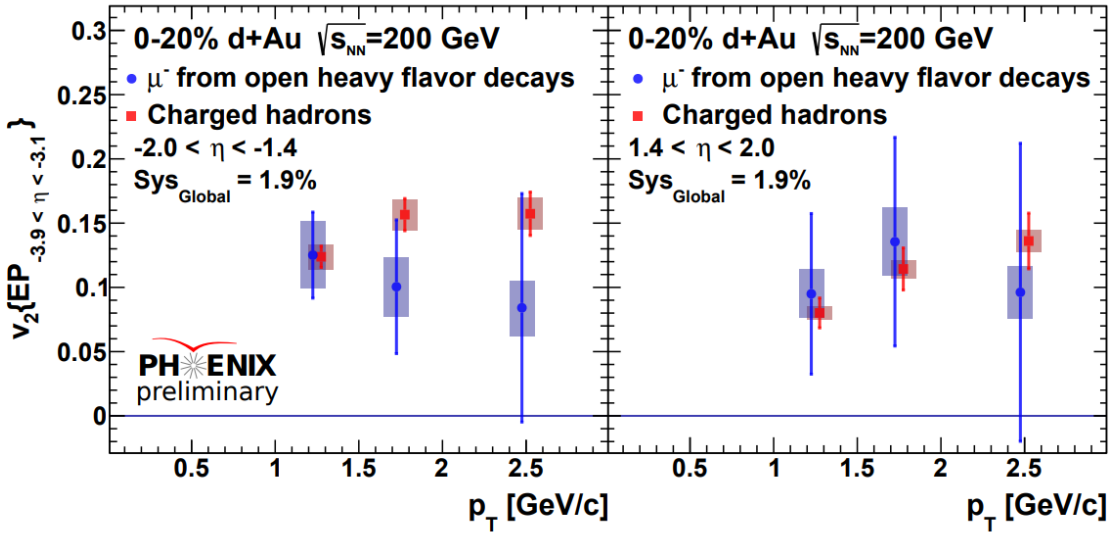

Fig. 1.13: Elliptic flow of $c + b \to \mu$ in d+Au collisions at $\sqrt{s_{\rm NN}} = 200$ GeV at the PHENIX experiment. Taken from [22].

Chapter 2

STAR experiment

The STAR experiment is installed in the Relativistic Heavy Ion Collider which is situated in the Brookhaven National Laboratory. Following chapter will introduce all of mentioned facilities.

2.1 Brookhaven National Laboratory

Situated in Upton, New York, Brookhaven National Laboratory (BNL) is one of the biggest scientific facilities in the United States of America. After World War II, in 1947, the Lab was opened in the former U.S. military base (Camp Upton) with the main purpose to study the atom and its energy for a peaceful application [24]. Nowadays it is a multipurpose research organization that connects thousands of scientists around the world. Together they received seven Nobel Prizes and many other awards and recognitions (as National Medal of Science, Enrico Fermi Award, Ernest Orlando Lawrence Memorial Award, etc.).

BNL's energy department studies generation, transmission, storage and end use of electric energy. Concerning the generation, the focus is on renewable sources (solar, wind, and nuclear power) without producing carbon dioxide that causes the climate change. BNL has its own photovoltaic plant, 32-megawatt Long Island Solar Farm, which is the largest in the Eastern U.S. To store the energy, advanced battery materials and superconducting magnets are being

developed here as well.

National Synchrotron Light Source II (NSLS-II), where electrons are accelerated almost to the speed of light at a curved trajectory producing synchrotron radiation in all wavelengths, is used to study structure of materials with nanoscale resolution, their chemical composition and magnetic properties. NSLS-II is a 3 GeV electron storage ring with circumference 792 m that started to operated in 2015. Its ancestor NSLS operated between 1982 and 2014. The research with these two facilities has helped to win two Nobel Prizes in Chemistry to:

- Roderick MacKinnon in 2003 *for structural and mechanistic studies of ion channels*,
- Venkatraman Ramakrishnan and Thomas A. Steitz in 2009 *for studies of the structure and function of the ribosome* [25].

The Center for Functional Nanomaterials is another department of BNL that studies proprieties of materials. In specialized laboratories, devices for nanoelectronics, nanophotonics, or biomedical engineering are being developed. Brookhaven Linac Isotope Producer, the high-energy medical particle accelerator, produces radioisotopes for diagnosis and disease treatment (targeted cancer therapy).

Brookhaven Lab is a member of both the Daya Bay Neutrino Experiment and the ATLAS Collaboration. The Lab also leads the development of 3 200 megapixels Large Synoptic Survey Telescope (that will be constructed on a mountaintop in Chile). On site of BNL, one can also find National Aeronautic and Space Administration (NASA) Space Radiation Laboratory that studies the effects of space radiation on cells and tissues with aim to reduce the risk for astronauts during long-term missions. Several scientists working in BNL won Nobel Prizes in Physics:

- Chen Ning Yang and Tsung-Dao Lee in 1957 *for their penetrating investigation of the so-called parity laws which has led to important discoveries regarding the elementary particles*,
- Samuel Chao Chung Ting in 1976 *for their pioneering work in the discovery of a heavy elementary particle of a new kind*,

- James Watson Cronin and Val Logsdon Fitch in 1980 *for the discovery of violations of fundamental symmetry principles in the decay of neutral K-mesons*,
- Leon M. Lederman, Melvin Schwartz, and Jack Steinberger in 1988 *for the neutrino beam method and the demonstration of the doublet structure of the leptons through the discovery of the muon neutrino*,
- Raymond Davis Jr. in 2002 *for pioneering contributions to astrophysics, in particular for the detection of cosmic neutrinos* [25].

2.2 Relativistic Heavy Ion Collider

The Relativistic Heavy Ion Collider, shown in Fig. 2.1, is an accelerator that can collide heavy ions or polarized protons at ultrarelativistic energies. As in the case of all high energy accelerators, particles need to be accelerated in several stages.

First of all, one needs the source of particles that will be accelerated. Until 2012, the ion source and the first pre-injectors were Hollow Cathode Ion Source and two Tandems Van de Graaf, respectively. This electrostatic accelerator facility could produce approximately 40 different ions from as light as hydrogen to as heavy as uranium. The necessity to transport the beam 860 m from Tandems to Booster was just one of many reasons to replace the source. Nowadays, Tandems Van de Graafs are used for applied research, e.g. in NASA Radiations Effects Facility.

After its development at BNL Collider-Accelerator Department, new pre-injector is being used, Electron Beam Ion Source (EBIS) with a laser ion source called LION, composed from a high-power pulsed laser with a solid target[1]. To become an adequate substitute of Tandems, EBIS is followed by Radio Frequency Quadrupole (RFQ) and a short Linac (linear accelerator). To compare LION and EBIS with their precursors, LION can switch between different species of ions very quickly. EBIS is more reliable and flexible, and since it is situated much closer to the subsequent facility, the transport line is only 30 m long. Additionally,

[1]In case of Au ions production, the target is 1-mm thick pad with area of 25×25 mm^2 [27].

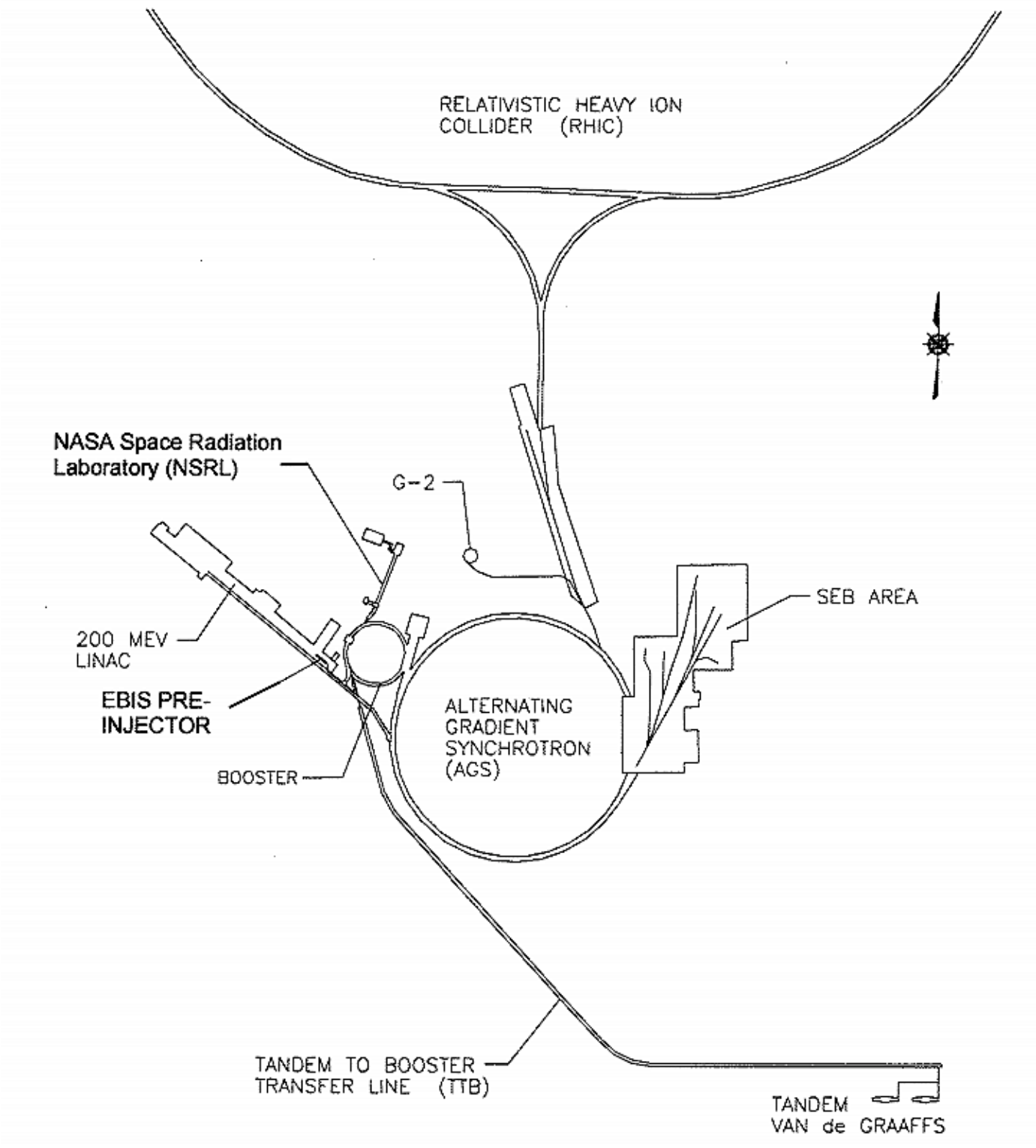

Fig. 2.1: The Relativistic Heavy Ion Collider and its preaccelerators. Taken from [26].

the injecting energy and intensity of ions are higher, so the injection is easier, with a smaller loss. Tandems can only produce negative ions, therefore before being injected to Booster, electrons have to be stripped away from them. This is done by a passage through a carbon stripping foil. On the other hand, LION can directly produce ions with desired charge state [26]. Moreover, LION can produce ions of noble gases needed to NASA Space Radiation Laboratory science programs.

After being produced in LION, positive ions with charge +1 go to EBIS where their charge is multiplied to 2, 32, and 39 for ^{3}He, Au, and U, respectively [28] and their output energy per nucleon is 16.24 keV/u. Afterwards ions go to RFQ via the Low Energy Beam Transport (LEBT) where are accelerated to 314.72 keV/u. Ions continue through Medium Energy Beam Transport (MEBT) to Interdigital-H (IH) 4-metres-long Linac where they are further accelerated to 2 MeV/u which is a minimal energy to enter the next stadium, the Booster. As EBIS complex produces short pulses (10-40 μs) with high intensity ($3.2 \cdot 10^9$ ions per pulse for Au^{32+}), the injection to the Booster is shorter in comparison with the injection with Tandems.

The injection to Booster, the circular accelerator with circumference 201.78 m [29], is done using the High Energy Beam Transport (HEBT). In Booster, built in 1991 to improve the operation of Alternating Gradient Synchrotron (AGS), gold ions are further accelerated to energy per nucleon 70 MeV/u. After leaving the Booster (thanks to kicker magnet), charge of ions increase (to 77 for gold ions) as they pass the stripping foil and lose electrons. Subsequently they are transferred into the AGS, circular accelerator with 4-times larger circumference as the Booster, 807.12 m.

After being kicked from AGS with energy approx. 10 MeV/u, ions enter 770-metres-long AGS-to-RHIC transfer line [30]. At its begging, the stripping foil, which takes away two last electrons from gold ions (producing final ions, Au^{79+}), is situated. When ions are closer to RHIC, a switch dipole is installed to direct beams into one of two RHIC rings, and finally, ions are injected to either clockwise (blue) or counterclockwise (yellow) ring (thanks to four vertical kicker magnets that inject bunch onto circulating orbit). In RHIC, 3834-metres-long

Run	species	total particle energy [Gev/nucleon]	total delivered luminosity $\cdot 10^{-9}$ [b^{-1}]
Run-14	Au + Au	7.3 + 7.3	44 200
	Au + Au	100.0 + 100.0	43.9
	He + Au	103.5 + 100.0	134
Run-15	*p* + *p*	100.2 + 100.2	0.382
	p + Au	103.9 + 98.6	0.001
	p + Al	103.9 + 98.7	0.003
Run-16	Au + Au	100.0 + 100.0	52.2
	d + Au	100.7 + 100	289
	d + Au	31.3 + 31.1	44.0
	d + Au	9.9 + 9.8	7.2
	d + Au	19.6 + 19.4	19.5
Run-17	*p* + *p*	254.9 + 254.9	0.579
	Au + Au	27.2 + 27.2	477 000
	p + *p*	254.9 + 254.9	0.00136
Run-18	Zr + Zr	100.0 + 100.0	3.9
	Ru + Ru	100.0 + 100.0	4.0
	Au + Au	13.5 + 13.5	282 000
	Au + **Au**	3.85	54 000
	Au + **Au**	26.5	35 000
Run-19	Au + Au	9.8 + 9.8	
	Au + **Au**	9.8	
	Au + Au	7.3 + 7.3	
	Au + **Au**	7.3	
	Au + **Au**	31.2	

Tab. 2.1: Summary of RHIC Runs. Bold means runs with a fixed Au target, italic runs with polarized beams. Run number is identified with the year of data-taking campaign (e.g. Run-14 is from 2014). Taken from [31].

collider, heavy ions gain the final energy per nucleon, up to 100 GeV/u.

The summary of consecutive stages of ionization and acceleration are shown in Figure 2.2 together with a maximum energy, number of ions per pulse and efficiency for every stage of the gold ions acceleration.

RHIC complex can accelerate and collide different pairs of ions as Au^{79+}, U^{92+}, Zr^{40+}, Ru^{44+}, or Cu^{29+}. It is also possible to produce asymmetrical collisions by colliding e.g. deuterium with the gold ions. Summary of RHIC runs since 2014 is in the Table 2.1, all runs can by found online at [31].

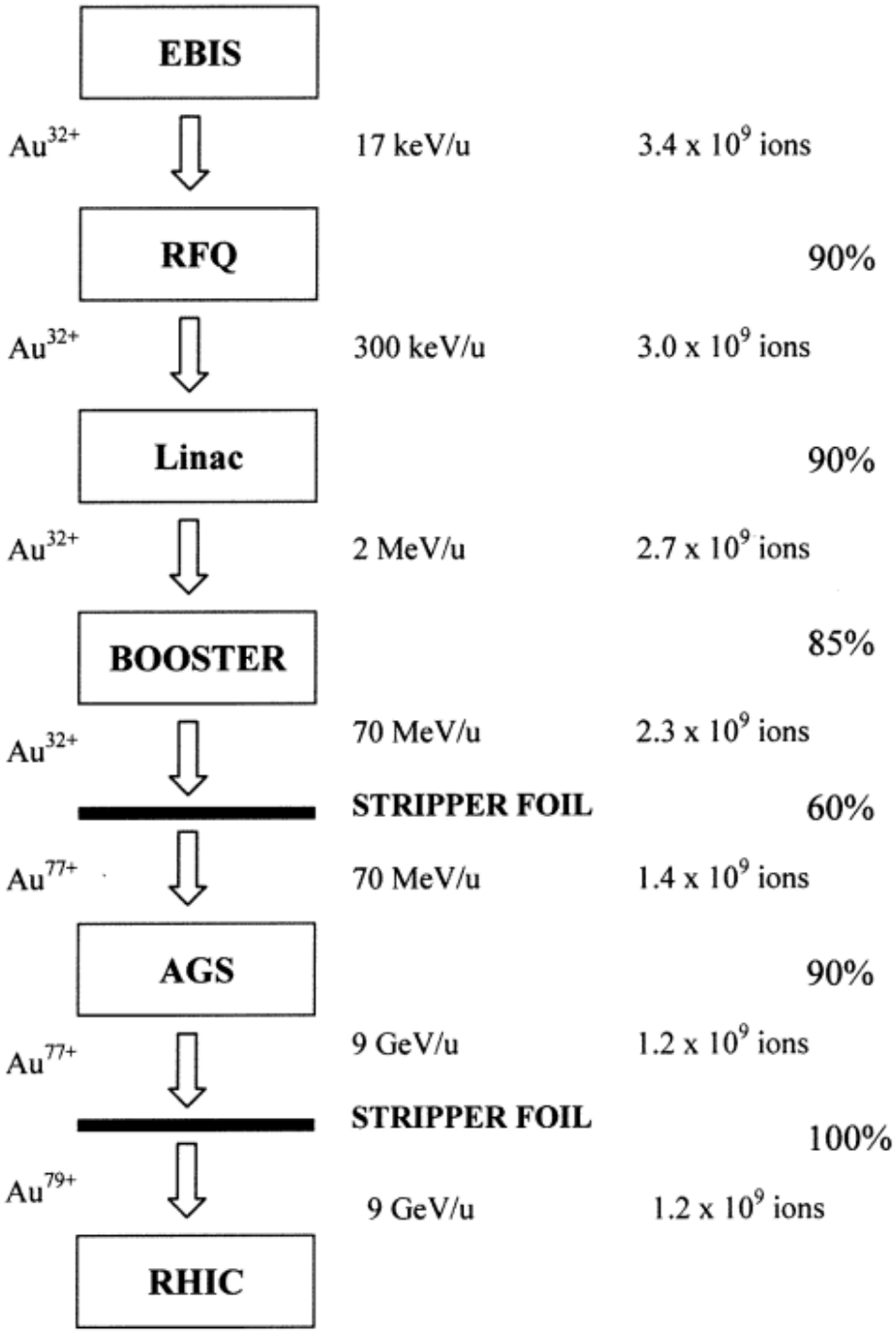

Fig. 2.2: Schematic of RHIC preacclereators. Taken from [26].

2.2. RELATIVISTIC HEAVY ION COLLIDER

RHIC is the only collider in the world that operates with polarized protons with the same direction of spin. The purpose of that kind of collisions is to study the spin of proton. The Optically Pumped Polarized Ion Source (OPPIS) creates $9 \cdot 10^{11}$ polarized H^- in a short pulse (300 μs) [32].

Hydrogen ions are accelerated to 200 MeV by RFQ and Linac. Afterwards they are stripped, hence they are polarized protons while entering the Booster. There they are accelerated to 1.5 GeV and transferred to AGS, where the acceleration continue until 25 GeV. Since during acceleration a depolarization occurs, a partial Siberian Snake is installed on AGS[2]. Beams are then injected to RHIC, where two full Siberian Snakes are located on opposite sides of the collider, and are further accelerated up to 500 GeV.

As already mentioned, RHIC has two independent rings, clockwise (blue) and counter-clockwise (yellow), with total six intersections between them. When one identify the circuit with a clock, intersections are placed on all even numbers and the injection is near 6 o'clock, as illustrated in Figure 2.3.

Experiments PHOBOS and BRAHMS have ended the data collection in 2005 and 2006, respectively. The focus of PHOBOS has been the new physics while BRAHMS (Broad Range Hadron Magnetic Spectrometer) has measured charged hadrons to study proprieties of highly excited nuclear matter produced in heavy ion collisions.

Experiment PHENIX (Pioneering High Energy Nuclear Interaction eXperiment) has finished data taking in 2016. Currently a new experiment sPHENIX is being developed. The new detector will be completed in 2022 and will start physics data taking at the beginning of 2023. It will focus on study of jets and beauty quarkonia, including the current-day questions regarding the perfect fluidity of the quark-gluon plasma [34]. While physics goals of PHENIX and STAR experiments are similar, thus study of quark-gluon plasma, PHENIX was designed to measure direct probes in heavy ion collisions (electrons, muons, photons).

[2]Siberian Snake is a device that rotates spin 180° around a horizontal axis. Since the rotation from the Snake is larger than the one caused by depolarizating resonances, spin remains stable.

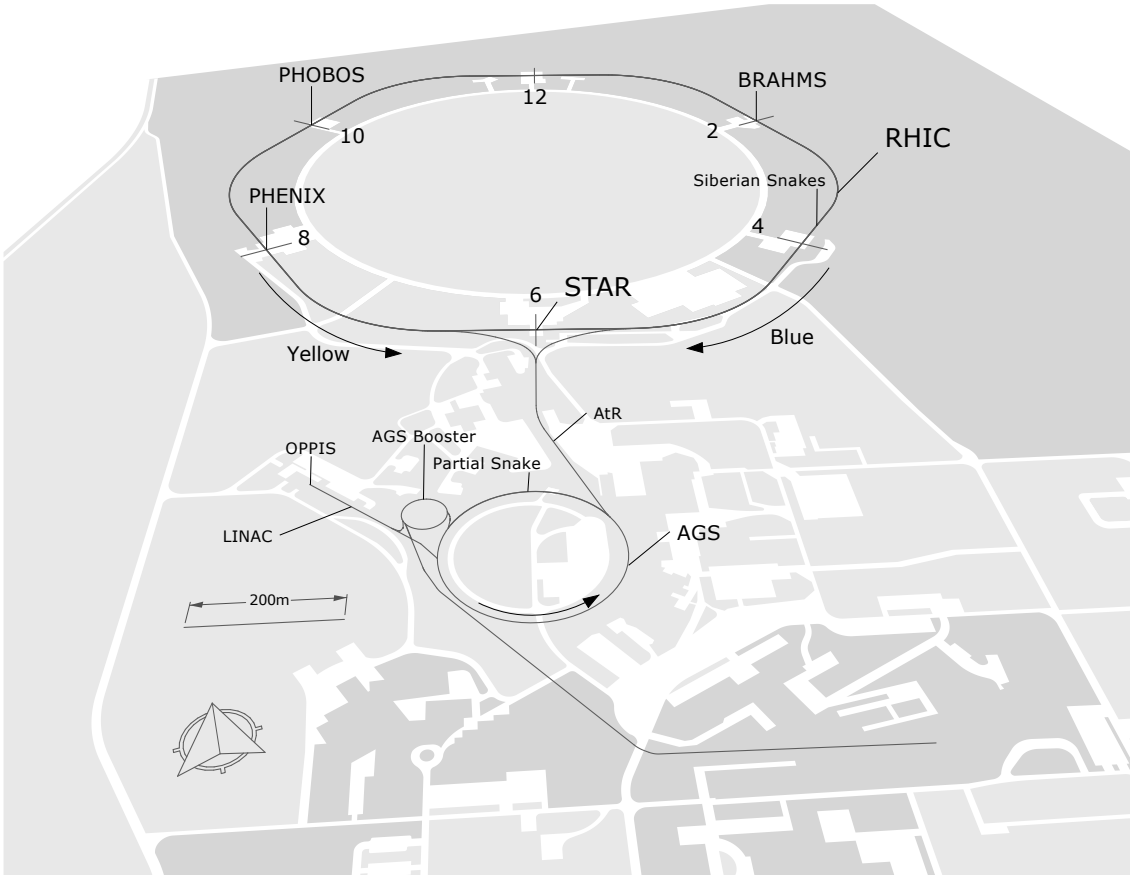

Fig. 2.3: RHIC preacclereators and intersection points. Taken from [33].

2.3 STAR experiment

The following chapter is dedicated to the STAR detector (Solenoidal Tracker at RHIC), shown in Figure 2.4, which is constructed to study formation and proprieties of quark-gluon plasma via measurement of particle production over a large solid angle. One of the physics goals of STAR experiment is to investigate the phase transition of nuclear matter for different collision energies and baryon chemical potential as shown in Fig. 1.1 and Tab. 1.2. Phase II of Beam Energy Scan programme is scheduled until 2020.

STAR consists of multiple detectors with different characteristics and purposes, e.g. high precision tracking, momentum analysis or particle identification. Only detectors used in the analysis which is described in this thesis will be introduced.

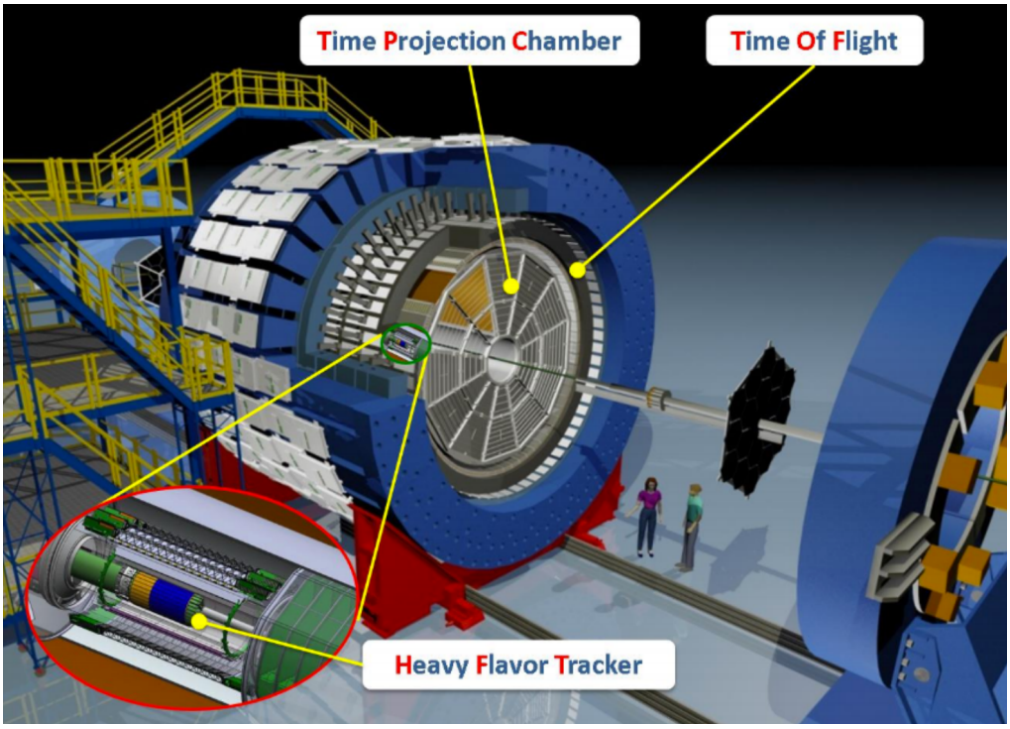

was

Fig. 2.4: STAR detector with selected subdetectors. Taken from [35].

The name of detector has connection with its main component - solenoidal magnet producing uniform magnetic field (0.5 T). The solenoid has interior and outside diameter 5.24 m and 5.94 m respectively, and is 6.2 m long [36].

Data collected by STAR are subsequently analyzed by the STAR collaboration consisting of scientists from 14 different countries. They are divided into five physics working groups with focus on a specific topic:

- bulk correlations,
- heavy flavor,
- jet-like correlations,
- light flavor spectra and peripheral collisions,
- spin.

2.3.1 Heavy Flavor Tracker

Being installed as the closest to the beam pipe, Heavy Flavor Tracker (HFT) is the first detector that particles hit which is strongly connected with the physics purpose of this detector - very precise measurement of heavy flavor production by reconstructing secondary vertices. Such measurement is very important as heavy quarks are commonly used for studying QGP. However, heavy particles decay very quickly compared to most of light ones, therefore the exact position of decay vertices of heavy flavor particles displaced from the primary vertex is very needed information [37]. The resolution of HFT is shown in Figure 2.5.

HFT was built and installed for RHIC Run 14 and removed two year afterwards. The design was made to have the best possible position resolution and consists of three subdetectors: Silicon Strip Detector (SSD), Intermediate Silicon Tracker (IST) and PIXEL (PXL) detector.

PIXEL detector is located closest to the beam pipe and uses state-of-the-art ultra-thin CMOS Monolithic Active Pixel Sensors (MAPS). It has 10 sectors with 4 ladders each, from which one is 2.9 cm from the center of the detector and three on the outer layer, 8.2 cm from the center. The total hit resolution is 6.3 μm. Since it is very close to the beam pipe, the detector was developed to be as resistant to the radiation damage as possible.

IST and SSD are made from single-sided double-metal silicon pad sensors and double-sided silicon strip sensors, respectively. Their position resolution is 170 μm, 20 μm in the $r \times \phi$ direction and 1.8 mm, 740 μm in the z direction.

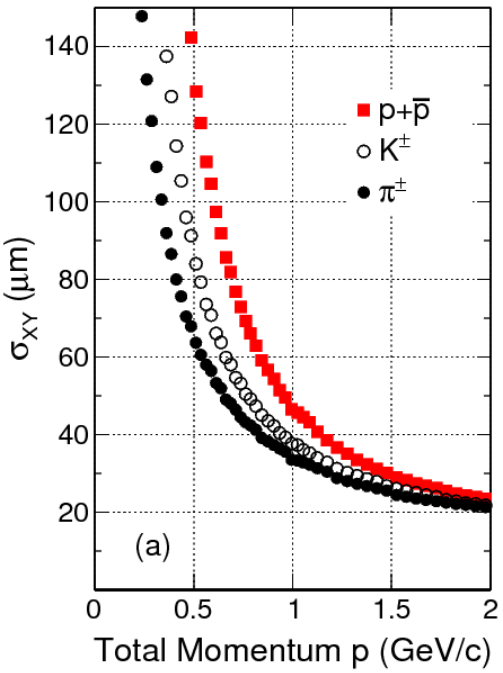

Fig. 2.5: Resolution of Heavy Flavor Tracker detector. STAR, Au+Au collisions at $\sqrt{s_{\mathrm{NN}}} =$ 200 GeV and centrality 0-80%. Taken from [38].

2.3.2 Time Projection Chamber

Time Projection Chamber (TPC), often called a heart of STAR, is its main tracking detector – it records the tracks of charged particles and also measures their momenta and charge based on the curvature of the trajectory, since charged particles in a magnetic field is moving on a circular path. Momenta are measured over a range of 100 MeV/c to 30 GeV/c [39].

TPC can identify particles in the momentum range from 100 MeV/c to 1 GeV/c. Particle identification (PID) by TPC is done by measuring the ionization energy loss of the particle with the use of Bethe-Bloch formula which gives the specific energy loss of charged particle

in homogeneous medium:

$$-\left\langle \frac{\mathrm{d}E}{\mathrm{d}x} \right\rangle = 2\pi N_A r_e^2 m_e c^2 \frac{Z}{A}\frac{z^2}{\beta^2}\left[\ln\frac{2m_e c^2\beta^2\gamma^2 W_{\max}}{I^2} - 2\beta^2 - \delta(\beta\gamma)\right], \tag{2.1}$$

where N_A is Avogadro's number ($N_A = 6,022 \cdot 10^{23}$ mol^{-1}), r_e is classical electron radius ($r_e = 2,81 \cdot 10^{-15}$ m), m_e is mass of electron ($m_e = 0,511$ MeV/c^2), c is speed of light in vacuum ($c = 299792458$ m·s^{-1}), Z and A are atomic and mass number of the absorber, respectively, z and v are charge and speed of the particle, $\beta = \frac{v}{c}$ and $\gamma^{-1} = \sqrt{1-\beta^2}$ are relativistic factors, I is mean ionization and excitation potential, $W_{\max}$ is magnetic kinetic energy which can be imparted in one collision and δ is density correction which is needed for highly relativistic velocities. The $\mathrm{d}E/\mathrm{d}x$ resolution depends on the gas and the pressure inside the chamber.

In the physics data analysis, the PID using the specific energy loss $\mathrm{d}E/\mathrm{d}x$ is done using the comparison of the expected value for a particle with the measured value. Then, an analyzer can choose the interval of the standard deviation in which he or she will consider this particle identified. For instance, the requirement on reconstructed kaons can be $|n\sigma_K| < 3$. The PID capability of TPC is shown in Fig. 2.6a.

Concerning the acceptance of TPC, it covers full azimuthal angle (2π) and pseudorapity $|\eta| < 1$, which is assured by its 4.2 m long and 4 m diameter barrel shape.

The volume of TPC is filled with P10 gas (90% argon, 10% methane). When the primary particle is passing through this gas, it is ionizing its molecules, creating electron-ion pair. Subsequently, secondary electrons are drifting towards readout located at the both ends of the chamber. The position resolution is limited with a diffusion of drifting electrons. The x, y position (so those in a transversal plane) are determined by the position of cluster where the charge was collected, the z coordinate is based on drifting time of secondary electrons from the point of origin to the anode. Since we measure the drifting velocity of electrons in the filling gas, we can determine the z position.

The inner sectors of TPC (iTPC) were recently upgraded. The new parts of detector have extended the track pseudorapidity acceptance to $|\eta| < 1.5$. This upgrade also increases

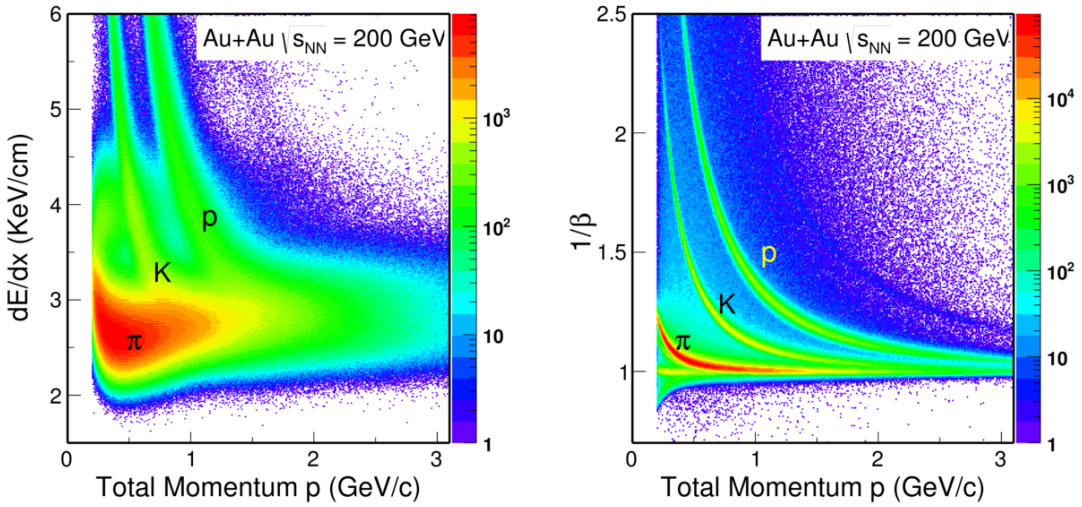

(a) $^{dE}/_{dx}$ from TPC. (b) $^{1}/_{\beta}$ from TOF.

Fig. 2.6: Particle identification capability as a function of particle momentum. STAR detector, Au+Au collisions at 200 GeV. Taken from [14].

the resolution in both $\mathrm{d}E/\mathrm{d}x$ and momentum and improves the acceptance of low momenta tracks [40]. iTPC has started taking data for RHIC Run 19 in 2019.

2.3.3 Time of Flight detector

Since the average proton transverse momentum in heavy ion collision is approximately 0.9 GeV/c, the TPC detector is not sufficient for the particle identification with the upper limit of 1 GeV/c. To extend the range of possible identification of particles with higher p_{T}, the barrel Time of Flight (TOF) was installed in 2010 [41]. As suggested by its name, TOF identifies particle based on the time of light inside the detector. For relativistic particles, where $E \simeq pc >> m_i c^2$, the separation power of TOF can be counted as

$$\Delta t = \frac{Lc}{2p^2}(m_1^2 - m_2^2), \tag{2.2}$$

where L is distance between TOF counters and the beam pipe (starting time is measured with other parts of the STAR detector, the Vertex Position Detector), p momentum (known

from TPC) and m_1, m_2 are the masses of two particles to be distinguished. The present capability of kaon separation is possible from ~ 0.6 GeV/c to ~ 1.7 GeV/c, while the upper limit for proton is ~ 3.0 GeV/c. The resolution is shown in Figure 2.7.

Since the trajectory of particle Δs is also known from TPC, with Δt known from TOF and relation

$$\beta = \frac{v}{c} = \frac{\Delta s}{\Delta t}\frac{1}{c}, \tag{2.3}$$

one can deduce the mass of the particle as

$$m = \frac{p}{c}\sqrt{\left(\frac{1}{\beta}\right)^2 - 1}. \tag{2.4}$$

Analogically to the TPC, the PID with TOF is done via the comparision of the expected and measured value. While the ALICE collaboration uses directly β, the STAR collaboration uses its inverse value, $1/\beta$. Thus, the identification is done as $|\Delta 1/\beta| = |\Delta 1/\beta_{\text{expected}} - \Delta 1/\beta_{\text{measured}}|$. An analyzer chooses a maximum value, e.g. $|\Delta 1/\beta| < 0.03$. The PID capability is shown in Fig. 2.6b.

TOF covers the same psedurapidity acceptance as the TPC, $|\eta| < 1$, and full azimuthal angle 2π. It uses the multi-gap resistive plate chamber (MRPC) with resolution sub-one hundred picoseconds and total efficiency approximately 95%. To cover full outside surface of the detector, there are totally 3800 MRPC modules with 6 pairs of copper pads each, producing more than 23 000 channels to be read out.

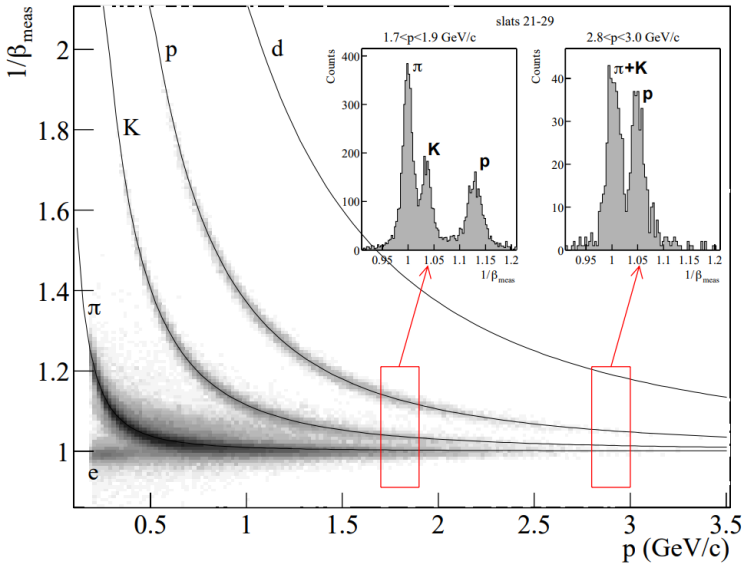

Fig. 2.7: Resolution of Time of Flight detector. Taken from [42].

Chapter 3

Measurement of D mesons at the STAR experiment

Open charm particles are a good probe of quark-gluon plasma and its whole evolution as heavy quarks are primarily produced in the initial stage of ultra-relativistic heavy-ion collision. Therefore, such measurement is important to study the hot medium and its properties.

The following chapter is dedicated to the summary of measurement of D^0 and $D^{\pm}$ mesons at the STAR experiment including their reconstruction, yield and nuclear modification factor. For D^0, the elliptic flow measurement is presented as well. The summary of properties of these particles is shown in Tab. 3.1.

meson	D^0	D^+
quark composition	$c\bar{u}$	$c\bar{d}$
mass [MeV/c^2]	1864.83 ± 0.05	1869.65 ± 0.05
mean life [s]	$(410.1 \pm 1.5) \cdot 10^{-15}$	$(1040 \pm 7) \cdot 10^{-15}$
$c\tau$ [μm]	122.9	311.8
Studied hadronic decay mode	$K^-\pi^+$	$K^-2\pi^+$
Its branching ratio [%]	3.93 ± 0.04	8.98 ± 0.28

Tab. 3.1: Properties of selected D mesons. Taken from [1].

Firstly, the event and track selection is shown for reconstruction of these particles as well as the raw yield extraction. Subsequently, the invariant yield is presented for both particles.

Finally, the nuclear modification factor and the elliptic flow are discussed together with the results of such measurements at other experiments.

3.1 Event and track selection

D mesons were reconstructed in Au+Au collisions recorded in 2014 and 2016, respectively, for D^0 ([14]) and $D^{\pm}$ ([43]). The heavy flavor analysis was possible thanks to the HFT detector that has significantly improved the tracking precision and secondary vertex reconstruction. The cut of the position of the collision primary vertex was 6 cm along the beam direction from the center of the detector, $|v_{z,(VPD)}| < 6$ cm. The Vertex Position Detector (VPD) was used to distinguish this distance. In order to make sure that the vertex was chosen correctly, an additional cut is applied to the vertex position – the difference between the vertex position (along beam line) measured with TPC and VPD has had to be less than 3 cm, $|v_{z,(TPC)} - v_{z,(VPD)}| < 3$ cm. After these selection criteria, $9 \cdot 10^8$ and $10.8 \cdot 10^8$ minimum bias triggered events are used for the reconstruction of D^0 and $D^{\pm}$, respectively.

In both selected analyses, daughter particles were required to have at least 20 hits in the TPC to obtain a good momentum resolution. High precision of the secondary vertex position is achieved requiring hits in both PIXEL layers of the HFT and at least one hit in the IST or SSD layers.

The particle identification (PID) was done using the specific energy loss $\langle {}^{dE}/_{dx} \rangle$ measured by TPC with the cut $|n\sigma_K| < 2$ and $|n\sigma_\pi| < 3$. Only if a track has matching hit in TOF, an additional cut on PID is used, $|\Delta {}^{1}/_{\beta}| < 0.03$, on both kaons and pions.

The pseudorapidity has to be within the kinematic acceptance of the detector. Therefore, tracks of daughter particles are required to satisfy $|\eta| < 1$. Additionally, transverse momentum of daughter particles has to be $p_T > 0.6$ GeV/c and $p_T > 0.5$ GeV/c for D^0 and D^+ candidates, respectively.

For D^0 reconstruction, following 6 topological variables (shown in Fig. 3.1) are used:

- Distance of the closest approach between two daughter tracks (DCA_{12}). The point

in the middle of this distance is also used to determine the secondary vertex of the collision (D^0 decay vertex).

- Decay length, the distance between primary and secondary vertices.
- Distance of the closest approach between the reconstructed D^0 candidate track and the primary vertex (DCA_{D^0}).
- Distance of the closest approach between decay products and the primary vertex (DCA_K, DCA_π).
- Cosine of the pointing angle θ, the angle between the Kπ pair reconstructed momentum and the vector connecting primary and secondary vertices.

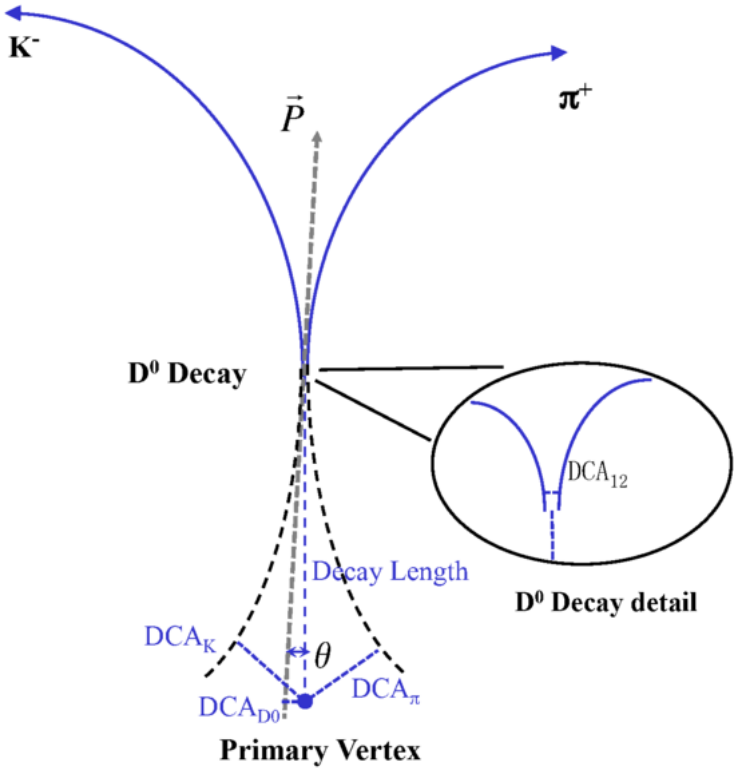

Fig. 3.1: Definition of topological variables for $D^0 \to K^-\pi^+$ decay. Taken from [14].

The set of cuts, obtained using Rectangular Cuts Optimization method implemented in TMVA package within the ROOT framework, has been chosen to gain the highest signal

significance. The tuning was done separately for different p_{T} and centrality bins of D^0 candidate. For instance, in 0-10% most central collisions with transverse momentum of D^0 candidate within the interval $1 < p_{\mathrm{T}} < 2$ GeV/c, used topological cuts are:

- $\mathrm{DCA}_{12} < 70$ μm,
- Decay length > 227 μm,
- $\mathrm{DCA}_{\mathrm{D}^0} < 40$ μm,
- $\mathrm{DCA}_{\mathrm{K}} > 82$ μm,
- $\mathrm{DCA}_{\pi} > 93$ μm,
- $\cos\theta > 0.95$.

Cuts for different p_{T} and centrality bins can be found in [14].

Topological variables for $\mathrm{D}^{\pm}$ reconstruction are analogical to D^0 reconstruction. However, as the former is a three-body decay, there are some differences. $\mathrm{DCA}_{\mathrm{pair}}$ is the longest of three lines connecting pairs Kπ, Kπ and $\pi\pi$ in the point of their closest approach. Creating a triangle from middle points of these lines, its longest side is denoted as Δ_m and will be used as a topological variables as well. The center of this triangle is the reconstructed secondary vertex. Afterwards, topological cuts for $\mathrm{D}^{\pm}$ reconstruction are:

- $\mathrm{DCA}_{\mathrm{pair}} < 80$ μm,
- $30 <$ Decay length < 2000 μm,
- $\Delta_m < 200$ μm,
- $\mathrm{DCA}_{\mathrm{K}} > 80$ μm,
- $\mathrm{DCA}_{\pi} > 100$ μm,
- $\cos\theta > 0.998$.

This set of cuts is for all p_{T} of $\mathrm{D}^{\pm}$ candidate and all collision centrality classes. Currently, the implementation of machine learning methods is in progress to obtain the highest possible significance in all p_{T} and collision centrality bins.

Last but not least, it is important to mention that the author of this thesis has contributed to the reconstruction of $\mathrm{D}^{\pm}$ meson in Au+Au collisions at the STAR experiment recorded in 2014. The main goal was to find $\mathrm{D}^{\pm}$ candidates using machine learning algorithms, mostly Boosted Decision Trees.

3.2 Raw yield extraction

Once the set of cuts has been applied, one can plot an invariant mass of D^0 and $\mathrm{D}^{\pm}$ candidate, which is the mass in the rest frame of this particle. It is obtain as a combination of momentum and energy of $\mathrm{K}\pi$ pairs and $\mathrm{K}\pi\pi$ triplets. The plot is done individually for correct-sign and wrong-sign combinations of pairs and triplets[1]. As in the D^0 analysis the statistics of background in peripheral collisions has not been not sufficient, mixed-event technique was used[2]. The invariant mass of pairs and triplets is shown in Fig. 3.2 and 3.3, respectively. The chosen p_{T} and centrality bin is shown in each figure. The peak in the area of the D^0 and $\mathrm{D}^{\pm}$ mass is clearly visible. The combinatorial background from wrong-sign combinations, shown in the figure, was normalized to match right-sign combinations.

Subsequently, the combinatorial background has been subtracted bin by bin, using the wrong-sign combinations of pairs/triplets. The raw yield is obtained by fitting the distribution of invariant mass of D^0 and $\mathrm{D}^{\pm}$ a Gaussian + linear function, where the latter is for the residual background. The position of the peak is as expected to be around the mass of candidate from [1].

[1]Correct-sign combinations are $\mathrm{K}^-\pi^+$ and $\mathrm{K}^+\pi^-$ for D^0 reconstruction and $\mathrm{K}^-\pi^+\pi^+$ and $\mathrm{K}^+\pi^-\pi^-$ for $\mathrm{D}^{\pm}$ reconstruction. All other combinations (2 for D^0, 4 for $\mathrm{D}^{\pm}$) are wrong-sign, i.e. these pairs or triplets cannot be decay products of D^0 or $\mathrm{D}^{\pm}$ and will be used for background estimation.

[2]Unlike-sign pairs from different events of similar characteristics have been added.

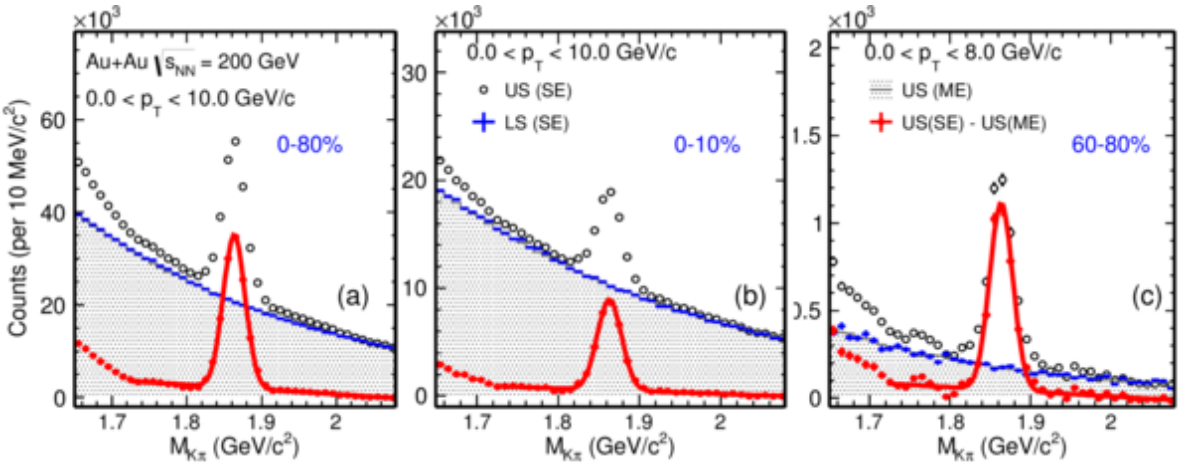

Fig. 3.2: Invariant mass M(Kπ) distribution for unlike- and like-sign pairs Kπ. Taken from [14].

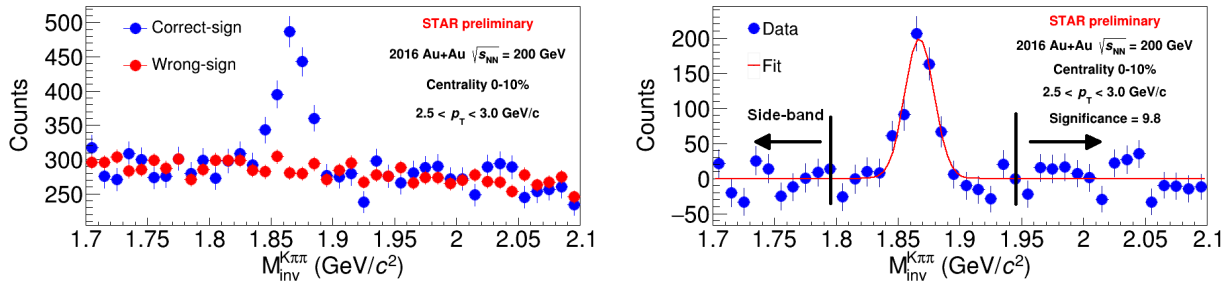

Fig. 3.3: Invariant mass M(K$\pi\pi$) distribution for correct- and wrong-sign triplets K$\pi\pi$. Taken from [43].

3.3 Invariant yield

The raw yield in each p_{T} and centrality bin has to be corrected if one wants to obtain a particle production invariant yield. The correction is done using the following formula:

$$\frac{\mathrm{d}^2N}{2\pi p_{\mathrm{T}}\mathrm{d}p_{\mathrm{T}}\mathrm{d}y} = \frac{N^{\mathrm{raw}}}{\mathrm{BR}\ N_{\mathrm{evt}} 2\pi p_{\mathrm{T}}\Delta p_{\mathrm{T}}\Delta y(\epsilon\ \times acc)}, \tag{3.1}$$

where N^{raw} and N_{evt} is a number of reconstructed D^0 counts and a total number of used events, respectively, BR is the decay branching ratio, and $(\epsilon\ \times acc)$ is a correction for the

detector efficiency and acceptance (including tracking efficiency, PID, vertex resolution, etc.). More details on corrections can be found in [14].

The corrected (invariant) spectra can be subsequently fitted with the Levy function

$$\frac{\mathrm{d}^2N}{2\pi p_\mathrm{T}\mathrm{d}p_\mathrm{T}\mathrm{d}y} = \frac{1}{2\pi}\frac{\mathrm{d}N}{\mathrm{d}y}\frac{(n-1)(n-2)}{nT(nT+m_0(n-2))}\left(1+\frac{\sqrt{p_\mathrm{T}^2+m_0^2}-m_0}{nT}\right)^{-n}, \tag{3.2}$$

where m_0 is the mass of D^0 ($\mathrm{D}^\pm$) and n, T and $\mathrm{d}N/\mathrm{d}y$ are free parameters. The invariant yield together with the Levy fit is shown in Fig. 3.4. Points in most of centrality classes are shifted for clarity (the scaling factor shown directly in the figure). The Levy fit describes the spectra with a good precision in all centrality bins.

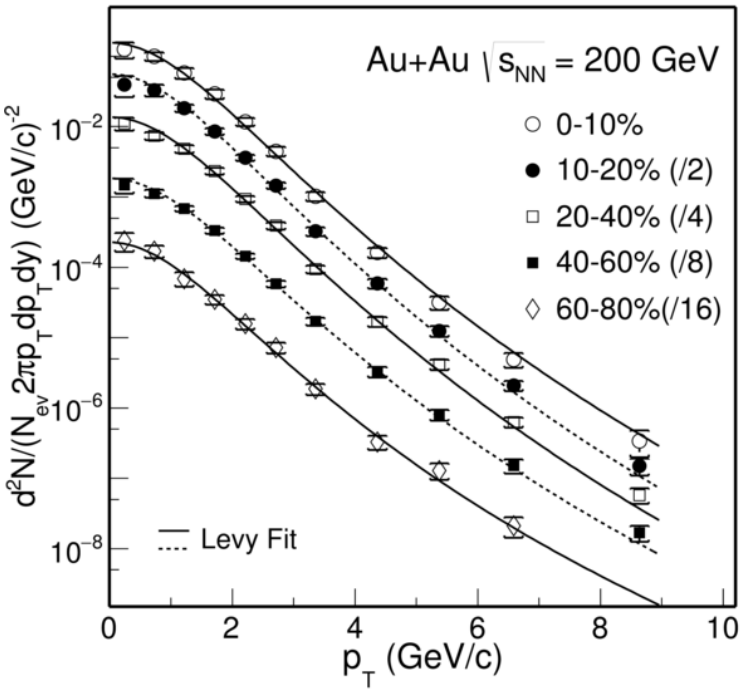

Fig. 3.4: D^0 invariant yield for different centrality classes as a function of transverse momentum. Taken from [14].

3.4 Nuclear modification factor

The nuclear modification factor R_{AA}, introduced in the first chapter, is defined using Eq. 1.3. This variable describes the modification of the production of the selected particle as a result of presence of the medium – the quark-gluon plasma. It compares yields of selected particle ($\mathrm{D}^0, \mathrm{D}^{\pm}$) in heavy-ion and proton-proton collision (scaled with a mean value of binary collisions in a heavy-ion collision). R_{AA} of D^0 was shown in the same section in Fig. 1.7. The result is compared with the one obtained from data-taking campaign 2010/2011.

R_{AA} of $\mathrm{D}^{\pm}$ meson together with D^0 is shown in Fig. 3.5 for 0-10% most central Au+Au collisions. Shapes of R_{AA} for both particles are consistent within the uncertainty. However, no information is available for $\mathrm{D}^{\pm}$ in the low-p_{T} region ($p_{\mathrm{T}} < 2$ GeV/c), as the yield has not yet been obtained because of very high combinatorial background. The greatest suppression is in rather high p_{T} for both D^0 and $\mathrm{D}^{\pm}$, with $R_{\mathrm{AA}} < 0.4$ for $p_{\mathrm{T}} > 6$ GeV/c.

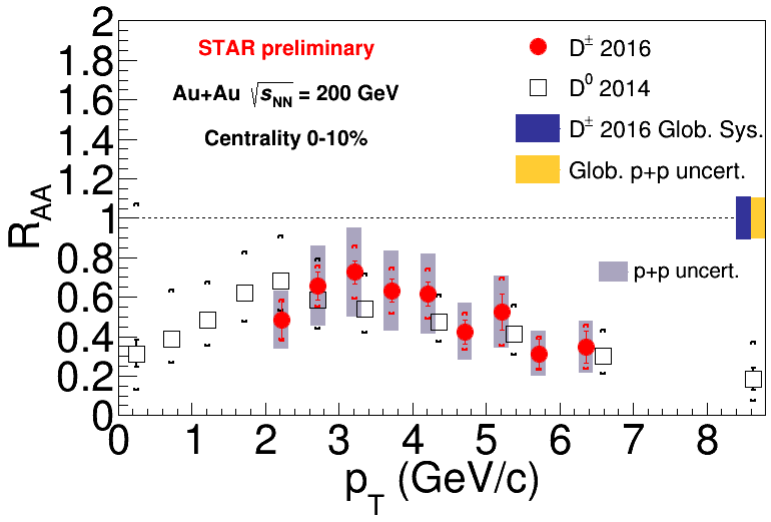

Fig. 3.5: Nuclear modification factor of D^0 and $\mathrm{D}^{\pm}$ mesons. Taken from [43].

The comparison with analysis of the data collected with ALICE experiment is presented in Fig. 3.6a. Shown D meson data-points are average of D^0, $\mathrm{D}^{\pm}$ and D^{*+}, measured with ALICE in Pb+Pb collisions at $\sqrt{s_{\mathrm{NN}}} = 2.76$ TeV. R_{AA} from both experiments is in a very good accordance in mid-p_{T}, values in the region $2 < p_{\mathrm{T}} < 4$ GeV/c are consistent within

the uncertainty. The trend is similar for high-p_{T} region ($p_{\mathrm{T}} > 4$ GeV/c), however, the suppression of D mesons reconstructed with the ALICE experiment is stronger compared to STAR expriment. This may be caused by the higher density and temperature of the QGP.

The comparison with the LBT (Linearized Boltzmann Transport calculation) and Duke models is shown in Fig. 3.6a as well. Data and shown models are in a good accordance within the uncertainty.

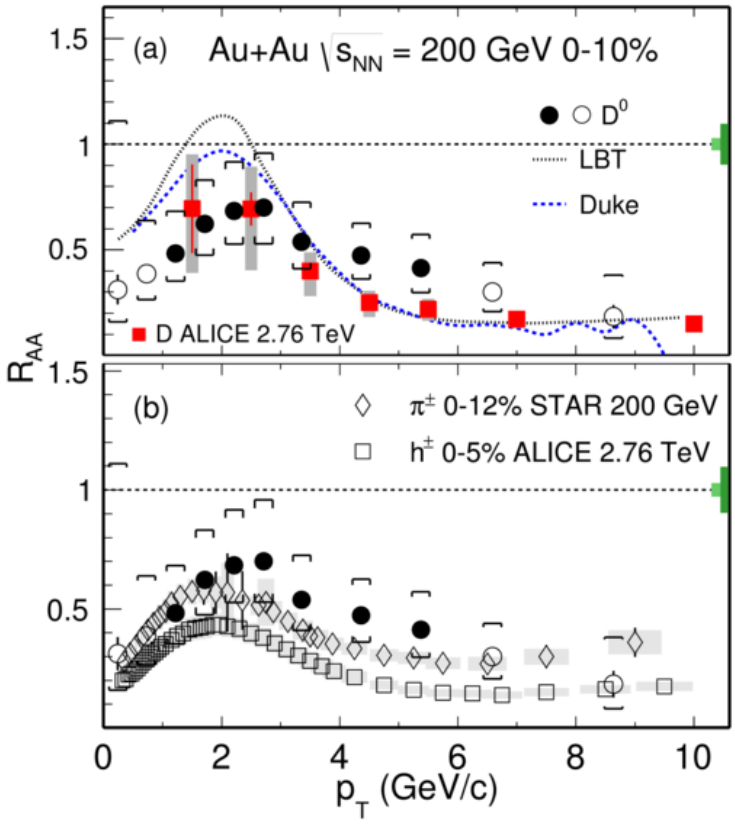

Fig. 3.6: Nuclear modification factor of D^0 from STAR and ALICE experiments. Taken from [43].

In the lower part of Fig. 3.6, one can find the comparison of R_{AA} of D^0 meson with R_{AA} of both charged pions from STAR and charged hadrons from ALICE at 200 GeV and 2.76 TeV, respectively, in central collisions. These results are accordant within the uncertainty with R_{AA} of D^0 and $\mathrm{D}^{\pm}$, trend is the same for both light hadrons and heavy D^0 meson. However,

in mid-p_T ($2 < p_T < 6$ GeV/c), the suppression is stronger for light particles, but remains consistent within uncertainties. The greatest suppression ($R_{AA} \approx 0.2$) is in the high-p_T region ($p_T > 8$ GeV/c).

3.5 Elliptic flow of D^0 meson

The elliptic flow measurement described in the following section, originally from [38], is for D^0 meson only, as such a measurement has not yet been done for $D^{\pm}$ meson at the STAR experiment. The event and track selection and PID cuts are the same as in the previous section of this chapter, however, topological cuts are slightly different as a different TMVA setup has been used.

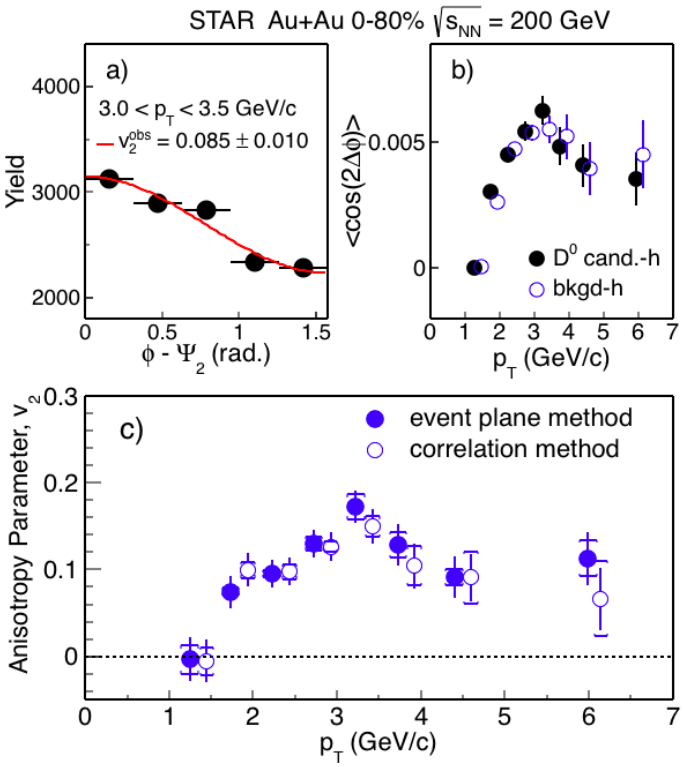

Fig. 3.7: a) Yield of D^0 as a function of $\phi - \Phi_2$. b) Correlations between D^0/background and charged hadrons. c) Elliptic flow of D^0 meson as a function of transverse momentum obtained with two different methods. Taken from [38].

Two independent methods were used to calculate the elliptic flow v_2 – the event plane method and the correlation method. In the former, the event plane (estimated reaction plane) is obtained from all tracks reconstructed in TPC but D^0 candidate daughter particles. To reduce non-flow effects, tracks for the event plane reconstruction were divided into two samples (sub-events) based on their pseudorapidity, a forward sample ($0.025 < \eta < 1$) and a backward one ($-1 < \eta < -0.025$). Particles with $-0.025 < \eta < 0.025$ were excluded. As only particles from opposite hemispheres were correlated, between each pair of particles there is a η-gap $|\Delta\eta| > 0.05$.

D^0 candidates are splitted to azimuthal angle bins relative to the event plane $\phi - \Psi_2$, where Ψ_2 is the second order event plane angle. The distribution of $\phi - \Psi_2$, shown in Fig. 3.7a, is fitted with the function $A(1 + 2v_2 \cos(2(\phi - \Phi_2)))$ with A as a normalization parameter. Final v_2, shown in Fig. 3.7c, is obtained from the fit result with additional scaling with $\langle 1/R \rangle$, where R is the event plane angle resolution.

The detailed description of the correlation method is shown in the section 4.2, therefore, only the crucial part of the D^0 flow analysis with such a method will be described here. The elliptic flow is calculated for unlike- and like-sign Kπ combinations separately, charged hadrons are used as a reference. The η-gap is the same as in the first method, 0.05. The result is obtained using the elliptic flow value of both unlike-sign (US) and like-sign (LS) combinations together with their yields as

$$v_2 = \frac{N_{\mathrm{US}}\ v_2^{\mathrm{US}} - N_{\mathrm{LS}}\ v_2^{\mathrm{LS}}}{N_{\mathrm{US}} - N_{\mathrm{LS}}}. \tag{3.3}$$

The final elliptic flow is shown in Fig. 3.7c. The points of the correlation method are shifted to the right for a better visibility. One can see that the elliptic flow obtained from both methods is consistent within the uncertainty.

Finally, the elliptic flow v_2 (from the event plane method) of D^0 meson is compared with v_2 of light hadrons Λ, Ξ^-, and K_s measured with the STAR experiment in semi-central Au+Au collisions at 200 GeV in Fig. 3.8a. In low p_{T} region ($p_{\mathrm{T}} < 2$ GeV/c), one can observe a hadron mass ordering. As D^0 is the heaviest from shown particles, it has the lowest v_2,

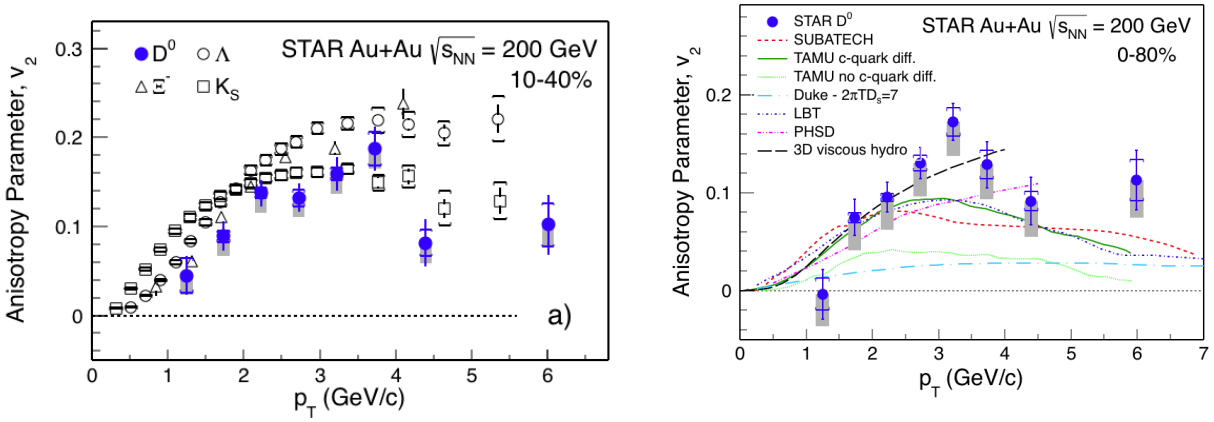

(a) Comparison with light hadrons.

(b) Comparison with models.

Fig. 3.8: Elliptic flow of D^0 meson as a function of transverse momentum compared with different particles and models. Taken from [38].

which is in good accordance with the theory. For $p_{\mathrm{T}} > 2$ GeV/c, it is possible to observe baryon-meson grouping (D^0 and K_s are mesons while Λ and Ξ^- are baryons). In general, it is possible to say that the elliptic flow of D^0 in Au+Au collisions is significant and comparable with light hadrons flow.

Figure 3.8b is dedicated to the comparison of elliptic flow v_2 of D^0 meson with different models (SUBATECH, TAMU, Duke, LBT, PHSD, 3D viscous hydro). TAMU model with no charm quark diffusion and Duke model do not describe the data, other models are consistent with it within the uncertainty in region $p_{\mathrm{T}} < 4$ GeV/c.

Chapter 4

Measurement of elliptic flow of D^0 meson in d+Au collisions

The first chapter of this thesis was dedicated to quark-gluon plasma and its signatures in the heavy-ion collision. It was shown that light flavor and open-charm hadrons exhibit a large collective flow in such collisions. This was believed to be a clear signature of the QGP and was considered to be a phenomenon connected exclusively with the heavy-ion collisions. However, in recent years, flow-like azimuthal particle correlations have been observed in the small colliding systems, such as the pp and p+Pb, as well. As the correlation is similar to the one measured in heavy-ion collisions, it is important to find out whether a QGP droplet is present in small collision systems as well. However, the significant difference between LHC and RHIC small collisions systems is the energy of the collision which is different in magnitude.

The topic of the following chapter is dedicated to the reconstruction of D^0 meson in d+Au collisions at $\sqrt{s_{\mathrm{NN}}} = 200$ GeV with the STAR experiment and subsequent calculation of the elliptic flow of this particle. The goal is to find out if the flow is present in this collision system. If so, it is important to find out its origin as at this collision energy, the presence of QGP droplet is rather improbable. The flow can be caused e.g. by cold nuclear matter effects. Moreover, it is known that the small systems are dominated by non-flow.

Firstly, the reconstruction of D^0 in d+Au collisions is presented. As the combinatorial background presence was rather high, it was crucial to use machine learning algorithms to improve topological reconstruction. We have decided to use boosted decision trees implemented in TMVA package within the ROOT framework. The description of the algorithm is shown together with its training and application phase.

Once the D^0 candidates are identified, it is possible to measure their elliptic flow. We have decided to use the multi-particle correlation method together with generic framework because of a non-uniformity of φ distribution. A detailed description of the calculation is shown later in the chapter. Finally, the elliptic flow as a function of particle transverse momentum is shown. For the lack of statistics, it is dificult to make any physical conclusions from the calculated flow as the uncertainty is very high.

Last but not least, it is important to emphasize that while the author of this thesis has had the biggest contribution in the elliptic flow measurement, the reconstruction of D^0 meson was done in a close collaboration with the consultant of this work.

4.1 Reconstruction of D^0 meson in d+Au collisions using boosted decision trees

In order to reconstruct the D^0 meson in d+Au collisions, we have decided to use the same decay channel ($D^0 \rightarrow K^-\pi^+$ with branching ratio 3.93 ± 0.04 % [1]) and the same topological variables as have been used for the analogical analysis in Au+Au collisions at the STAR experiment from data recorded in 2014 [14]. Nevertheless, all of the important information will be provided in this section as well. D^0 in this section will represent both D^0 meson and $\overline{D^0}$ anti-meson as the analysis was done for both of these particles in the same time (without discriminating if it is a particle or an antiparticle).

4.1.1 Event and track selection

The dataset used for the reconstruction of D^0 meson was approximately $3.5 \cdot 10^8$ minimum

bias d+Au events at $\sqrt{s_{\mathrm{NN}}} = 200$ GeV collected with the STAR experiment in 2016. To make sure that we can use the full potential of the particle reconstruction within the detector, we have required the collision to be located in the central part of the detector – the vertex had to be less than 6 cm in beam direction from the center of the STAR detector, $|v_z| < 6$ cm. Additionally, a cut on correlation of primary vertices reconstructed independently with the Time Projection Chamber and the Vertex Position Detector was 3 cm, $|v_{\mathrm{z,(TPC)}} - v_{\mathrm{z,(VPD)}}| < 3$ cm. Both these cuts are the same as in D^0 reconstruction in Au+Au collisions from 2014.

The key role in this analysis was held by the Heavy Flavor Tracker which was a part of the STAR detector complex in 2014 – 2016. This detector has significantly improved the tracking capability of STAR and has helped to distinguish between primary and secondary vertices of the collisions, which is crucial for heavy flavor analyses. The D^0 meson was reconstructed without this detector from data recorded with the STAR experiment in 2010 and 2011. However, the efficiency of the reconstruction is much smaller.

To have a high quality of recorded tracks, we have required to have hits in both PIXEL layers and a hit in one of the IST or SSD layers. More details about layers of the HFT are shown in the section 2.3.1 of this thesis.

Moreover, at least 15 hits in the TPC were required for the track reconstruction. Daughter particles (Kπ pairs, decay products of D^0) were also required to be within the geometrical acceptance of the detector with the track pseudorapidity cut $|\eta| < 1$. Transverse momentum of daughter particles had to follow $p_{\mathrm{T}} > 0.15$ GeV/c.

For particle identification (PID), two detector systems were used – TPC and TOF, their PID capability in d+Au collision is shown in Fig. 4.1. Both distributions are in a good accordance with PID capability in Au+Au collisions (Fig. 2.6). Using TPC, where the PID is done using the specific energy loss $\langle {}^{dE}/_{dx} \rangle$, the condition a kaon and a pion had to follow was $|n\sigma_K| < 2$ and $|n\sigma_\pi| < 3$, respectively. Both kaons and pions had to follow $|\Delta {}^{1}/_{\beta}| < 0.03$ cut only and if only the TOF information was available. We have decided to use this approach (denoted Hybrid TOF) as we lost too much of good candidates when the TOF matching was always required (Strict TOF).

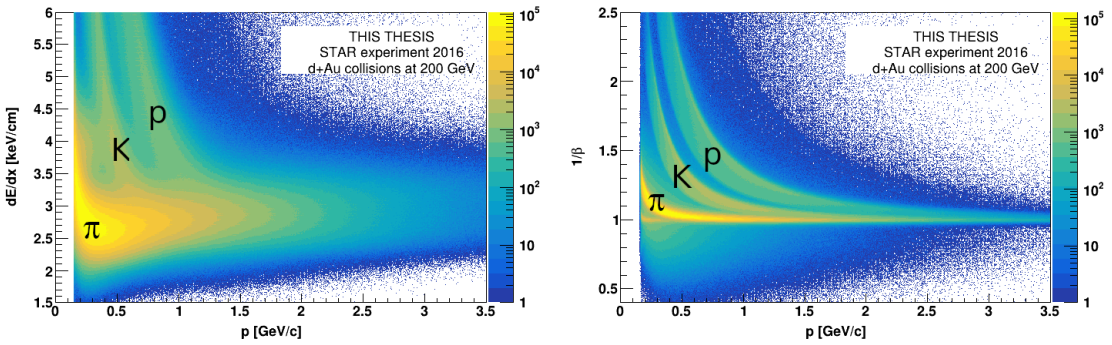

(a) $^{dE}/_{dx}$ from TPC. (b) $^{1}/_{\beta}$ from TOF.

Fig. 4.1: Particle identification capability as a function of particle momentum. STAR detector, d+Au collisions at 200 GeV.

Distributions of transverse momentum p_T for all charged kaons and pions that were properly reconstructed and identified is shown in Fig. 4.2.

We have chosen the same set of topological variables used for the D^0 reconstruction as were used in the analogical analysis in Au+Au collisions, thus:

- Distance of the closest approach between two daughter tracks (DCA_{12}).
- Decay length.
- Distance of the closest approach between the reconstructed D^0 candidate track and the primary vertex (DCA_{D^0}).
- Distance of the closest approach between decay products and the primary vertex (DCA_K, DCA_π).
- Cosine of the pointing angle θ ($\cos\theta$).

All these variables are shown in Fig. 3.1.

The reconstruction of D^0 was done using a set of rectangular cuts optimized with TMVA (Toolkit for Multivariate Data Analysis). Algorithms of this methods are used to try different sets of cuts where cut-points are random. Then, the best set is chosen based on background

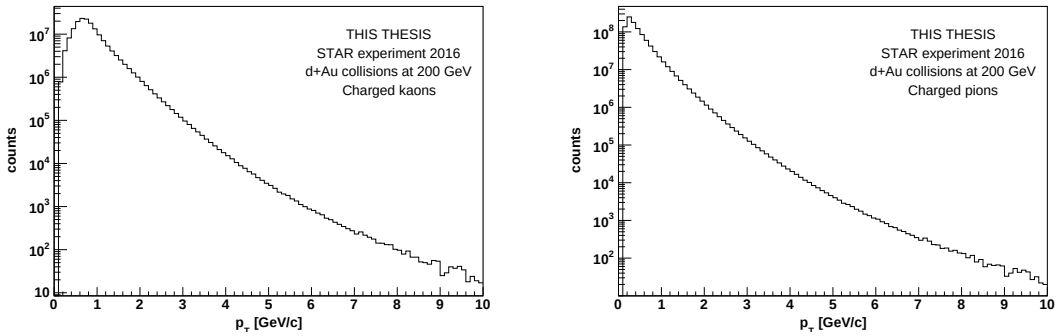

(a) Kaons. (b) Pions.

Fig. 4.2: Distribution of transverse momentum p_{T} for charged kaons and pions. STAR detector, d+Au collisions at 200 GeV.

rejection for a given signal efficiency [44]. As this method uses only one hyper-cube out of the multivariate phase space, we have decided to reconstruct D^0 with Boosted Decision Trees instead.

4.1.2 Boosted decision trees

4.1.2.1 General introduction

In general, the aim of a machine learning algorithms used for the classification in particle physics is to make a function $f : \mathbb{R}^d \to \mathbb{R}^N$, where $N << d$. Most common classification in particle reconstruction is assigning events to two disjoint sets – signal and background. Let $\vec{x} \in \mathbb{R}^d$ be inputs, $\vec{y} \in \mathbb{R}^N$ outputs, and f shall be the response function. During a training phase of supervised machine learning process, output is known to a given input – we provide pairs $\{\vec{y}, \vec{x}\}$. Later on, in the application phase, $\vec{y}$ will be assigned to $\vec{x}$.

In terms of D^0 reconstruction in d+Au collisions, $d = 6$, as we are using 6 topological variables to distinguish weather a Kπ pair originates from D^0 decay or not, $N = 1$, and the response function is defined to be 1 for pure signal (ideal case) and -1 for pure background. We want the algorithm to predict whether the pair with unknown origin is signal or background.

For this task, we have used Boosted decision trees from TMVA package within the ROOT

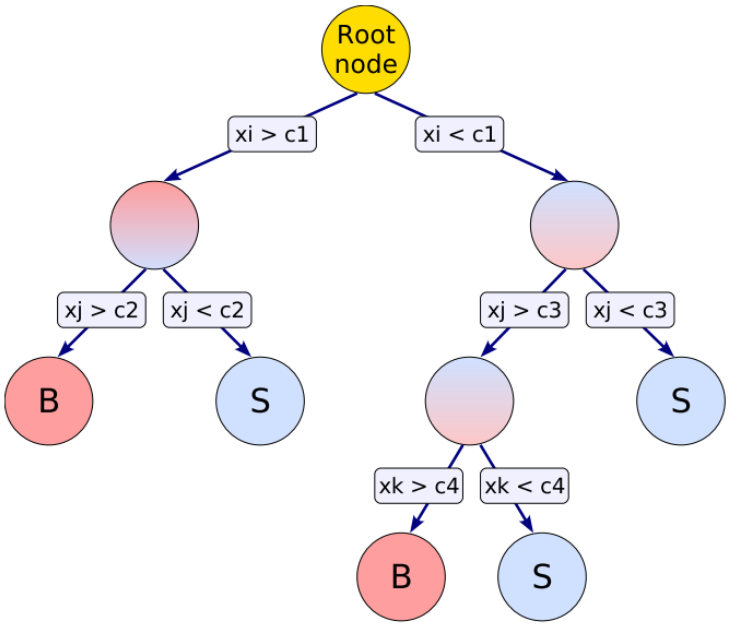

Fig. 4.3: Binary decision tree. Taken from [44].

framework. A binary decision tree is shown in Fig. 4.3. At the beginning, all data (events, pairs) are stored in the root node. Subsequently, they are divided based on a single variable cut into two disjoint sets. In the next step, either a different discriminating variable is used, or the same one with a different cut value. Also, the dividing can stop in every node once the data stored in this node are signal or background only, such node is then called a leaf. The maximum depth of a tree is the maximum number of cuts from the root node to a leaf node. If there is a limit on the maximum depth, the leaf node is called signal or background based on the majority of training events that are within it.

A tree created like this is easy to understand thanks to its similarity to standard rectangular cuts. However, a single tree is unstable with respect to the training sample. Therefore, boosting algorithm is added – we use several trees instead of just one. Additionally, event weights are applied. It has been shown that this algorithm works the best for a big amount of rather shallow trees. The most used boosting in TMVA is AdaBoost (Adaptive Boost) in which weights are higher for event misclassified in a previous tree. The response function is then a weighted average of responses over all of the trees.

With boosting applied, the straightforwardness of a single decision tree is lost. Nevertheless, what is gained is the stability with respect to fluctuations in the training sample. As it was already stated, only one hypercube of the whole phase space is used when using a rectangular cuts, but the whole phase space is divided into hypercubes when using boosted decision trees. Each hypercube is assigned to be signal- or background-like.

4.1.2.2 Training phase

Once the important notions and the main ideas have been presented, the reconstruction of D^0 meson using boosted decision trees can be described. The same set of 6 topological variables was used as in the reconstruction with rectangular cuts. The training was done separately for 3 p_T bins, based on p_T of D^0 candidate (combined p_T of Kπ pair) – $1 < p_T(D^0) < 2$, $2 < p_T(D^0) < 3$, and $3 < p_T(D^0) < 5$ GeV/c. The following set of pre-selection cuts were used on tracks and chosen topological variables:

- $DCA_{12} < 200$ μm,
- $5 <$ Decay length < 2000 μm,
- $DCA_{D^0} < 500$ μm,
- $DCA_K > 20$ μm,
- $DCA_\pi > 20$ μm,
- $\cos\theta > 0.5$.

After several tests of the algorithm performance, boosted decision trees within TMVA were used with 400 trees with the maximum depth of 3 for the first p_T bin ($1 < p_T(D^0) < 2$ GeV/c), 350 trees with the maximum depth of 4 for the second one ($2 < p_T(D^0) < 3$ GeV/c), and 300 trees with the maximum depth of 3 for the last used p_T bin ($3 < p_T(D^0) < 5$ GeV/c). The boosting method was AdaBoost.

For the training, one needs two datasets with same distributions, one for signal and one for background. The signal sample originates from data-driven fast simulator. The $D^0 \to K^-\pi^+$

decays were generated by PYTHIA and kinematical variables were smeared according to the detector response to be consistent with d+Au collisions recorded with the STAR experiment in 2016. Background sample comes from wrong-sign pairs from the same dataset as is used for the analysis – d+Au collisions recorded in 2016 with the STAR experiment.

Distribution for all 6 variables used for the BDT training in the first p_{T} bin ($1 < p_{\mathrm{T}}(\mathrm{D}^0) < 2$ GeV/c) is shown in Fig. 4.4. It can be seen that while the distribution of $\cos\theta$ is almost uniform for the background sample, the data is situated around 1 for the signal sample as the law of the momentum conservation has to be followed. For other variables, or for $\cos\theta$ closer to the peak, it would be hard to choose the optimal cut value as distribution of both signal and background are similar. This can serve as another reason why the multivariate analysis is crucial to reconstruct D^0 with a high significance.

The correlations of input variables (obtained independently for signal and background samples) are shown in Fig. 4.5. It can be seen that for Kπ pair that originates from D^0 decay, the decay length strongly correlates with both $\mathrm{DCA}_{\mathrm{K}}$ and DCA_{π}. Nevertheless, BDT method is not affected by the correlation between input variables.

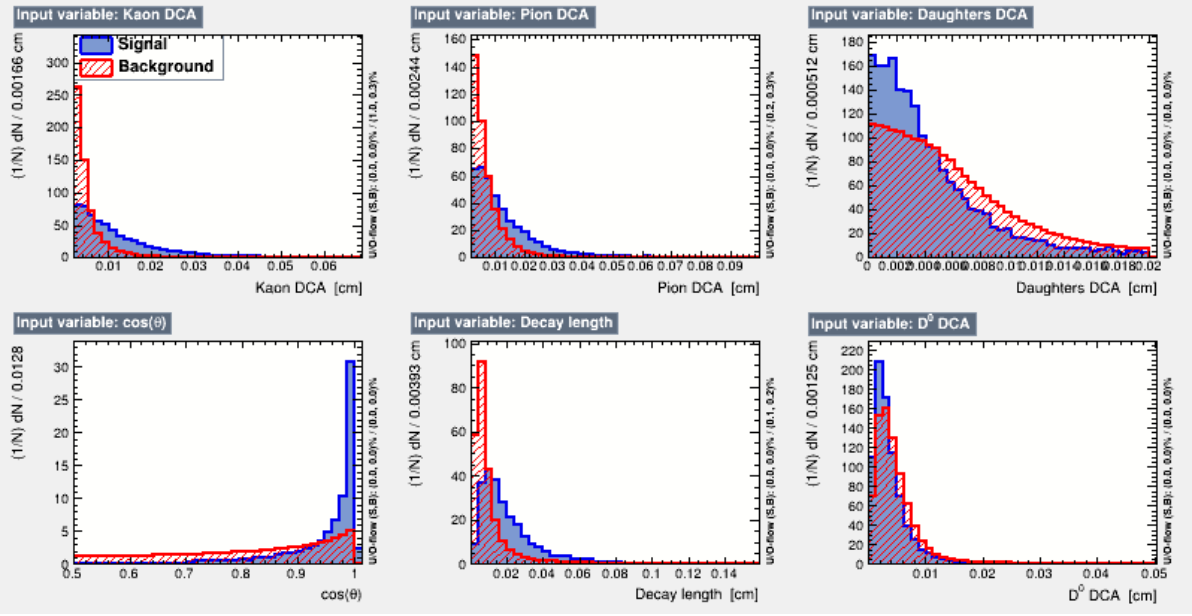

Fig. 4.4: Distribution of input variables for BDT training for D^0 reconstruction in the p_{T} bin $1 < p_{\mathrm{T}}(\mathrm{D}^0) < 2$ GeV/c.

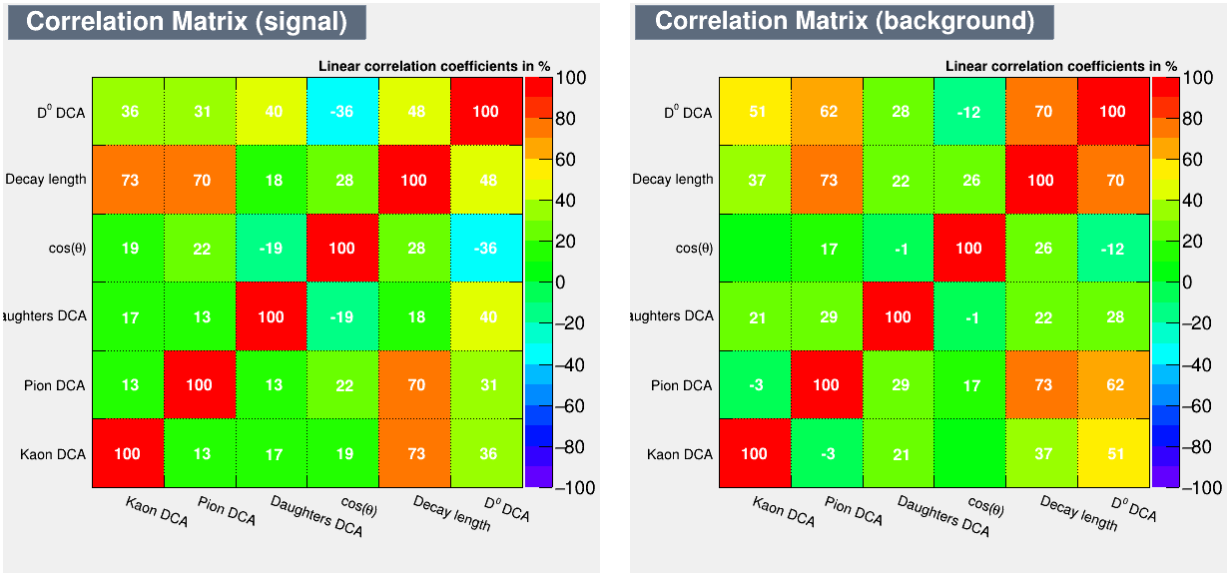

Fig. 4.5: Correlation matrices for signal and background in the training phase of BDT for D^0 reconstruction in the p_T bin $1 < p_T(D^0) < 2$ GeV/c.

Before the application, it is important to make sure that produced trees are not over-trained, as that would negatively influence the performance of the algorithm. One randomly selected part of the data is used for the training, the remaining data is used for the testing of produced trees. During the testing phase, it is crucial to know of which event is signal and which comes from background as this will help evaluate the method's performance.

The distribution of BDT response function for signal and background superimposed for test and training sample is shown in Fig. 4.6. It can be seen that the distribution for both test and training sample is in a very good accordance for signal and background.

Subsequently, one needs to choose a BDT cut value for the application phase. Later on, only events with BDT response higher than the cut value will be used for the D^0 reconstruction and the flow analysis. However, the optimal cut value deduced from TMVA depends on the signal-to-background ratio in data that will be analyzed. This can be seen in Fig. 4.7, where cut efficiencies and optimal cut values are shown for signal-to background ratios 1:1, 1:10, 1:100, and 1:1000. It can be observed that the optimal cut value function changes significantly for selected ratios.

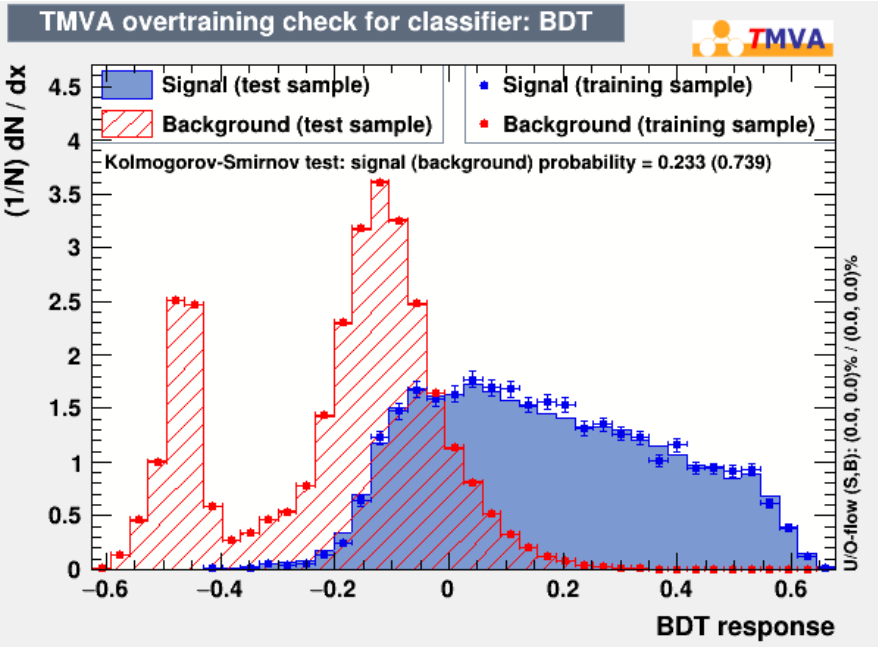

Fig. 4.6: BDT response function distribution for training and testing sample for D^0 reconstruction in the p_T bin $1 < p_T(D^0) < 2$ GeV/c.

There are several methods how to choose the optimal ratio without blindly guessing. However, they are just rough estimation, and can be strongly biased. For this reason, we have decided to find the optimal cut value in the application phase.

4.1.2.3 Application phase

Trained BDT algorithm was applied to both like- and unlike-sign Kπ pairs with varying BDT cut value. The invariant mass distribution of Kπ pairs is shown in Fig. 4.8a for $1 < p_T(D^0) < 2$ GeV/c. The shown distribution is for BDT cut value 0.365. Using this cut, we can obtain the highest signal significance.

Like-sign pairs are subtracted from unlike-sign ones, and subsequently, the distribution is fitted with Gaussian + linear function as shown in Fig. 4.8b. For each such distribution with different BDT cut value, the significance is calculated as $S/\sqrt{S+2B}$, where S and B is number of signal and background pairs, respectively. This value is obtained with bin counting in the region $\pm 3\sigma$ around the Gauss mean.

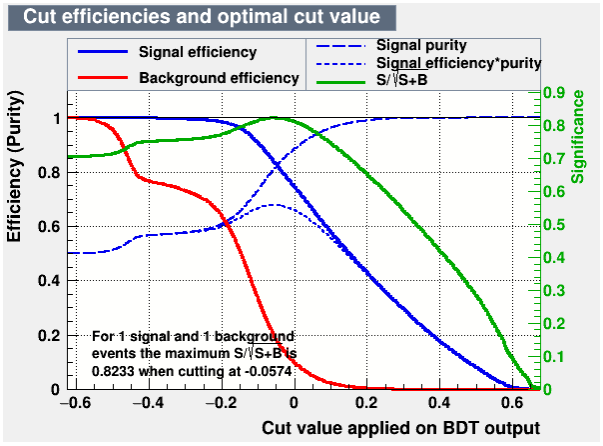

(a) Sig:Bkg - 1:1.

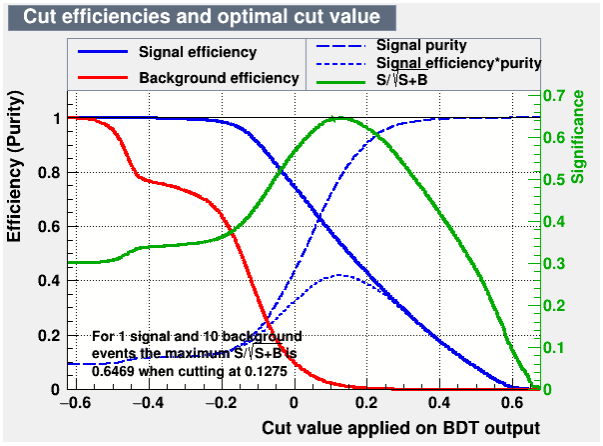

(b) Sig:Bkg - 1:10.

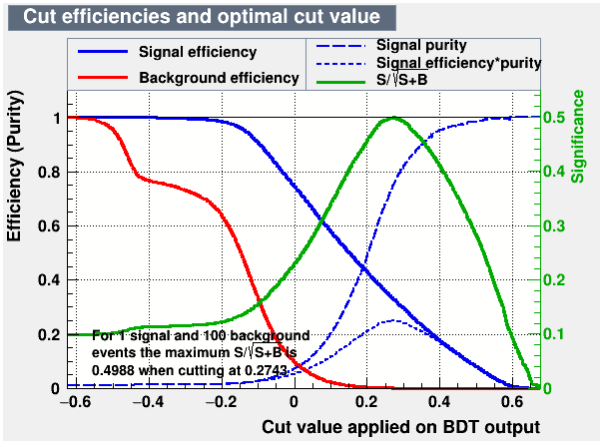

(c) Sig:Bkg - 1:100.

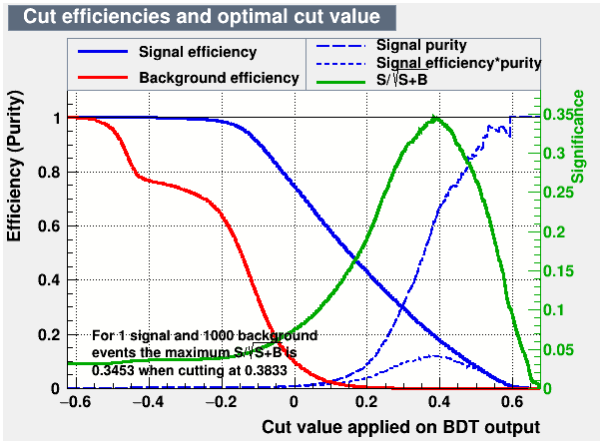

(d) Sig:Bkg - 1:1000.

Fig. 4.7: Cut efficiencies and optimal cut value plots from the training of TMVA for $D^{\pm}$ analysis in the p_T range $2 - 2.5$ GeV/c for different ratios of signal and background.

Analogically, we have obtained the invariant mass distributions of Kπ pairs for $2 < p_T(D^0) < 3$ and $3 < p_T(D^0) < 5$ GeV/c shown in the appendix in Fig. A.1 and A.2.

For the flow analysis, we have chosen rather loose cuts (0.21, 0.2, and 0.22 for each p_T bin in increasing order of $p_T(D^0)$, respectively), as the higher yield was more important than the purity of the signal. The distribution for both US and LS Kπ pairs and the subtracted distribution together with the fit is shown in Fig. 4.9 for p_T bin $1 < p_T(D^0) < 2$ GeV/c. Distributions for other p_T bins are shown in the appendix in Fig. A.3 and A.4.

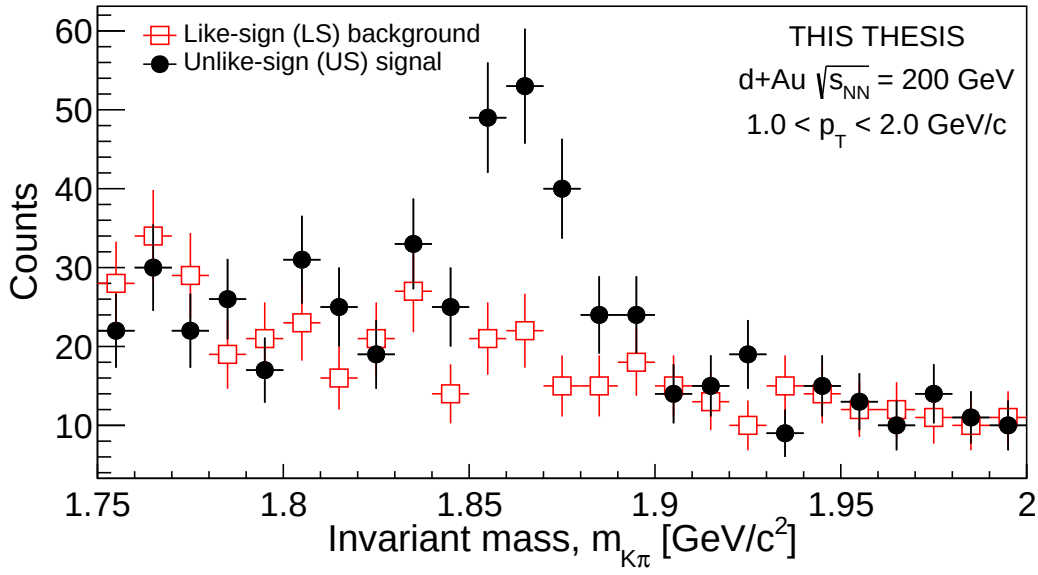

(a) Unlike- and like-sign Kπ pairs.

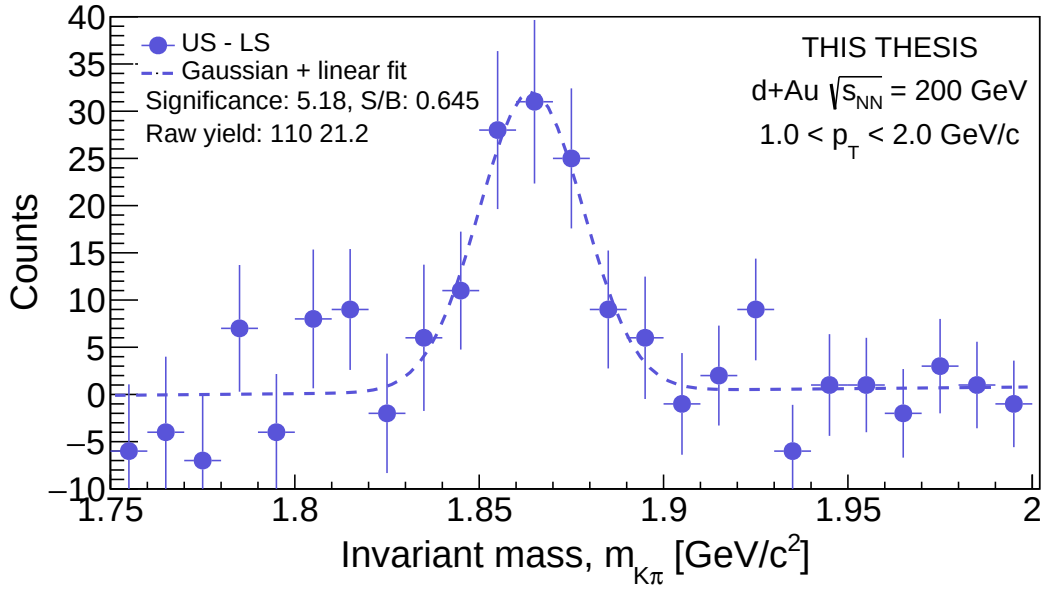

(b) Subtracted distribution together with the fit with Gaussian + linear function.

Fig. 4.8: Distribution of invariant mass of Kπ pairs in the p_{T} bin $1 < p_{\mathrm{T}}(\mathrm{D}^0) < 2$ GeV/c with BDT cut value 0.365.

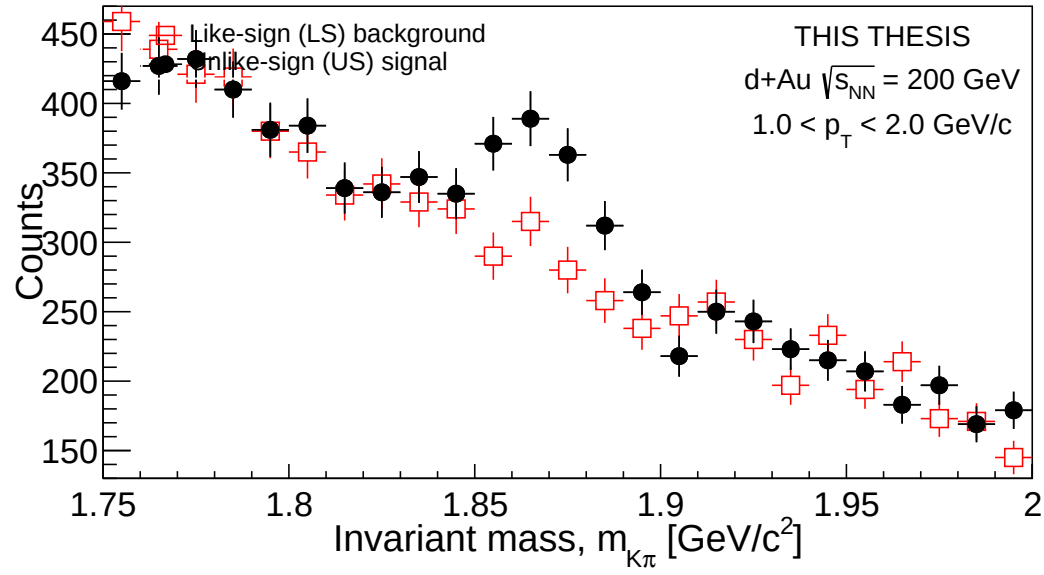

(a) Unlike- and like-sign Kπ pairs.

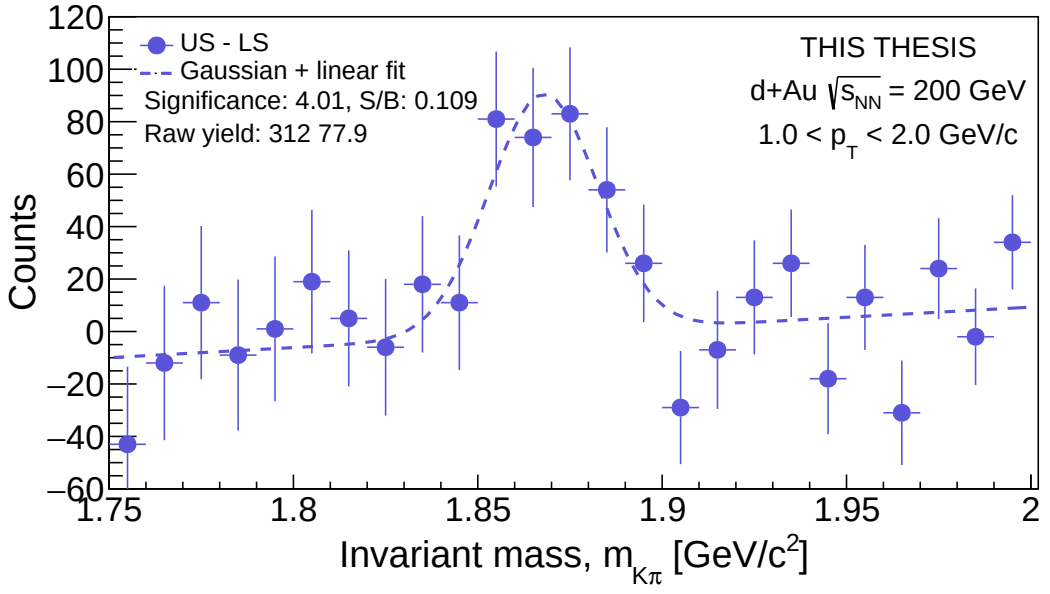

(b) Subtracted distribution together with the fit with Gaussian + linear function.

Fig. 4.9: Distribution of invariant mass of Kπ pairs in the p_{T} bin $1 < p_{\mathrm{T}}(\mathrm{D}^0) < 2$ GeV/c with BDT cut value 0.21.

4.2 Multi-particle correlation method with Generic Framework

Measurement of the anisotropic flow in heavy-ion collisions is usually connected with one of the following methods – event plane method or multi-particle correlation one. The former one is limited by the multiplicity of events – the resolution of the event plane (estimated reaction plane) is a function of this event characteristic. In d+Au collisions, the multiplicity is not sufficient for using such method. Moreover, small systems are known for being dominated by non-flows effects (a flow-like signal caused by non-collective behavior of the system). For these reasons, we have decided to use the latter one, multi-particle correlation method.

The multi-particle azimuthal correlations and cumulants are obtained using direct calculations [45]. During the analysis, a problem with non-uniform detector acceptance has occurred – to fix this problem, we have decided to use the Generic Framework [46]. The main difference between these methods is that instead of classical flow vector Q_n defined as

$$Q_n = \sum_{k=1}^{M} e^{in\varphi_k}, \tag{4.1}$$

where M is the numer of particles, n the harmonic and φ_k the azimuthal angle of the k-th particle. The Generic Framework uses following weighted Q-vector

$$Q_{n,p} = \sum_{k=1}^{M} w_k^p e^{in\varphi_k}. \tag{4.2}$$

As the Q-vector of charged hadrons will be used as a reference for the measurement of elliptic flow of D^0 meson, it is important to exclude daugter particle tracks (to avoid autocorrelations) in the Q-vector production.

The weight in general can be a function of various variables, $w = w(\varphi, p_T, \eta, \mathrm{PID}, ...)$. In following text, all particle weights are φ-weights, and are used, as already stated, to fix the detector acceptance problem.

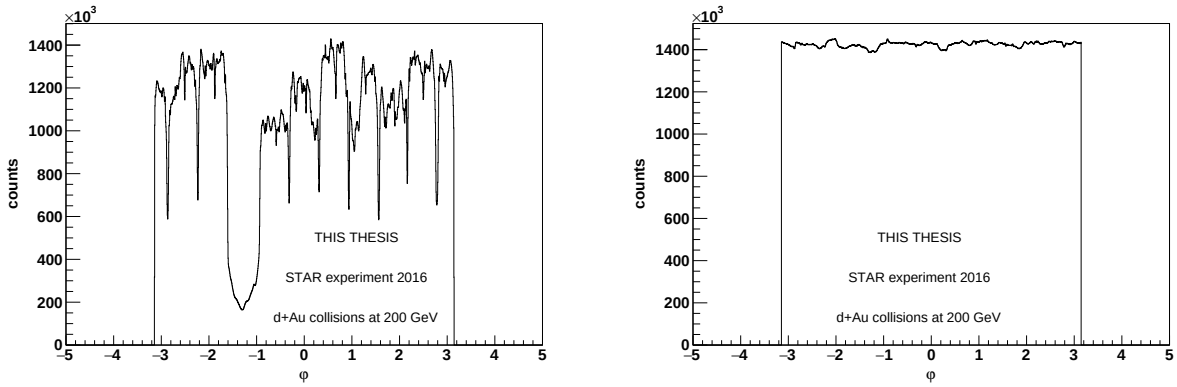

(a) Before. (b) After.

Fig. 4.10: Distribution of φ of charged hadrons before and after particle weights have been applied.

The distribution of azimuthal angle φ of all charged hadrons from the examined dataset is shown in Fig. 4.10a where the non-uniformity can be easily seen. More significant than the lack of entries in between individual sectors of TPC is a enormous drop of entries between $-2 < \varphi < -1$. This hole is caused by a dead sector in HFT during the data-taking campaign in 2016. Weights used in this analysis are obtained after the first loop over data as

$$w(\varphi) = \frac{N^{max}}{N(\varphi)}, \tag{4.3}$$

where N is a number of entries in selected φ bin and N^{max} is the maximum entries in a φ bin (from non-weighted distribution).

In the second loop over data, the histogram of φ distribution is filled with weights to check if the non-uniformity is reduced. The obtained distribution is shown in Fig. 4.10b, therefore we do not need to worry anymore about this problem.

Further improvement can be accomplished using two-dimensional particle weights which are also η dependent, $w = w(\varphi, \eta)$. However, the non-uniformity in η is not that significant as in φ. Eq. 4.3 then becomes

$$w(\varphi, \eta) = \frac{N^{max}}{N(\varphi, \eta)}. \tag{4.4}$$

Distribution of φ vs. η is shown in Fig. 4.11. Another possible improvement is to assign particle weights (1D or 2D) for each physics run separately.

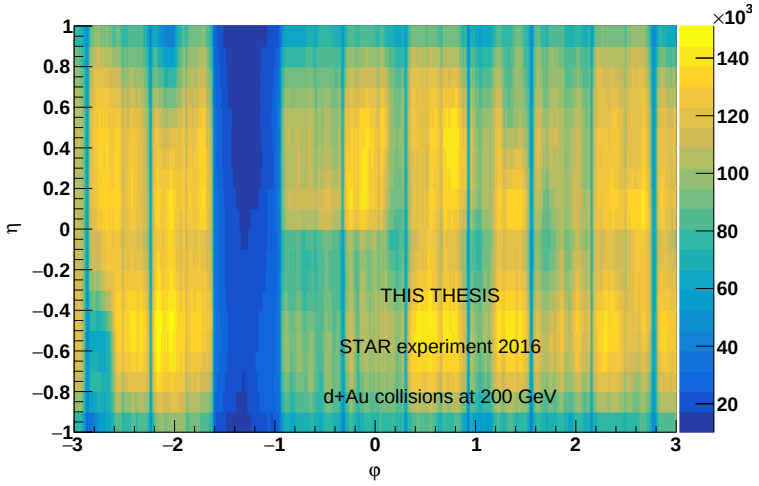

Fig. 4.11: Distribution of φ vs. η of charged hadrons.

In general, one can use use flow Q-vectors to calculate different harmonics using multi-particle correlations. Mixed ones are needed for order higher than 2.[1] However, the analysis described in this thesis is focused on elliptic flow ($n = 2$) with two-particle correlation, therefore only relations used later on will be presented. Generalization can be found in aforementioned papers.

Two-particle correlation expressed in terms of non-weighted Q-vectors is defined as

$$\langle 2 \rangle_2 = \frac{|Q_2|^2 - M}{M(M-1)}. \tag{4.5}$$

Once weights are applied, the expression is modified to

$$\langle 2 \rangle_{2,2} = \frac{Q_{2,1}Q_{-2,1} - Q_{0,2}}{Q_{0,1}^2 - Q_{0.2}}. \tag{4.6}$$

From the definition of the Q-vector, one can easily deduce $Q_{-2,1} = Q_{2,1}^*$.

Subtracted terms of previous formulas are to avoid autocorrelations. However, another

[1] For instance, 4-particle cumulant is defined as $c_n\{4\} = \langle\langle 4 \rangle\rangle - 2 \cdot \langle\langle 2 \rangle\rangle^2$.

approach was chosen, so-called subevent method, which additionally reduce non-flow effects which is really important in measurement of flow in a small system.

Using a sub-event method, Q-vectors are constructed independently for forward ($\eta > 0$) and backward ($\eta < 0$) samples. Moreover, to increase the correctness of the measurement, we have excluded particles with $|\eta| < 0.075$, producing η-gap $|\Delta\eta| > 0.15$. Two-particle correlation is then computed as

$$\langle 2 \rangle = \frac{Q^F_{2,1} \cdot Q^B_{-2,1}}{Q^F_{0,1} \cdot Q^B_{0,1}}, \tag{4.7}$$

where Q^F and Q^B are flow Q-vectors of forward and backward sample, respectively.

In the following step, two-particle correlation is averaged over all events[2]

$$\langle\langle 2 \rangle\rangle = \sum_{i=1} \frac{W_i \langle 2 \rangle_i}{W_i} = c_2\{2\}. \tag{4.8}$$

In this analysis, no event was superior to another one, hence no event weights have been applied (more precisely, $W_i = 1,\ \forall i$). For multi-particle correlation, an expression of multi-particle cumulant becomes more complicated, however, for this two-particle case, the event-averaged two-particle correlation is equal to the two-particle cumulant $c_2\{2\}$.

Finally, it is possible to obtain the reference flow as

$$v_2^{\text{ref}} = \sqrt{c_2\{2\}}. \tag{4.9}$$

In Fig. 4.12, the elliptic flow of all charged hadron as a function of multiplicity[3] is shown. It is important to mention that only a few entries were available for higher multiplicity. The flow without using Generic Framework is shown as well (in red). It can be seen that the usage of φ weights was important as it has significantly shifted v_2^{ref} towards lower values.

The obtained reference flow is compared with the flow of charged hadrons in p+Pb colli-

[2]Averaging was done using ROOT's TProfile.

[3]The multiplicity used here is the reference multiplicity of global tracks, obtained as mPicoEvent→grefMult. It is a sum of all global tracks with $|\eta| < 0.5$.

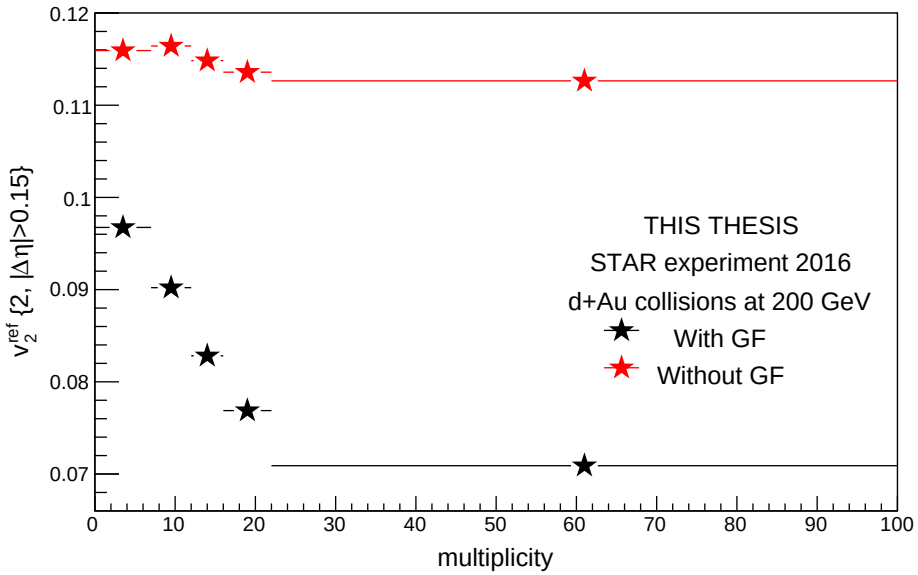

Fig. 4.12: Reference flow (charged hadrons).

sions at $\sqrt{s_{\mathrm{NN}}} = 5.02$ TeV recorded with the ALICE experiment [47]. To make the data more comparable, we have applied an additional cut on p_{T} of charged hadrons ($p_{\mathrm{T}} < 3.0$ GeV), as hadrons recorded with ALICE follow $0.2 < p_{\mathrm{T}} < 3.0$ GeV. This should reduce non-flow effects originating in jets. Additionaly, we have significantly increased the η-gap to $|\Delta\eta| > 1.0$, as ALICE analyses uses $|\Delta\eta| > 1.4$. However, the multiplicity in collisions recorded with the ALICE experiment is much higher, thus results cannot be compared in the whole range. The value obtained with the STAR experiment in the highest multiplicity bin is in good accordance with ALICE data. However, it is important to emphasize no correction of multiplicity value has been applied on shown STAR data-points. Moreover, collision energies differ in magnitude. Therefore, higher values in low multiplicites are probably caused by non-flow effects.

The cumulant used later on is only a number ($c_2\{2\} = 0.0852 \pm 0.0001$) as in chosen dataset the statistics was insufficient for dividing the analysis for smaller samples (based on the event multiplicity) – only p_{T} binning has been applied.

The calculation of differential flow is the next step in the flow analysis. In the first step, we have calculated the reference flow from reference particles (all charged hadrons). On

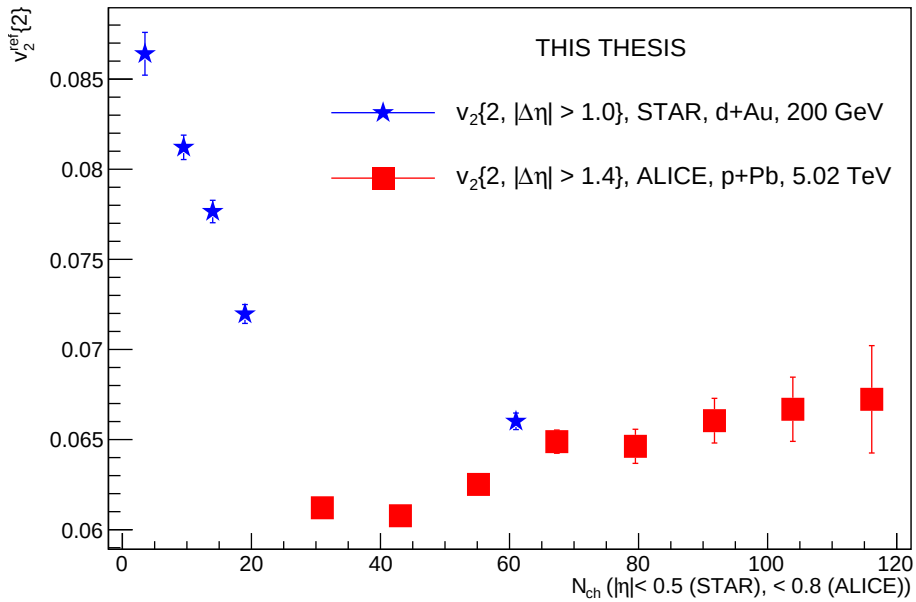

Fig. 4.13: Reference flow of charged hadrons from STAR and ALICE experiments.

the contrary, the differential flow of D^0 meson, or particle of interest (POI) in general, is calculated with respect to reference particles.

The flow p-vector of POIs is defined as

$$p_{n,p} = \sum_{j \in \mathrm{POI}}^{m} w_j^p e^{in\psi_j}, \tag{4.10}$$

where m is a number of POIs and ψ_j is used to label the azimuthal angle of a POI (the typical notation is ψ for POIs and φ for reference particles). In this analysis, the candidate-by-candidate approach has been chosen (instead of event-by-event) in accordance with the measurement of elliptic flow of D^0 in Au+Au collisions at the STAR experiment.

Subsequently, one can calculate the differential two-particle correlation (the following formula is used within the sub-event method) as

$$\langle 2' \rangle = \frac{p_{2,1}^F \cdot Q_{-2,1}^B}{p_{0,1}^F \cdot Q_{0,1}^B}. \tag{4.11}$$

To emphasize what has been already stated, daughter particles of D^0 candidates are excluded from Q-vector calculation to avoid autocorrelations (in exactly this step).

Averaging over all events, one can get the differential cumulant as

$$\langle\langle 2' \rangle\rangle = \sum_{i=1} \frac{W_i \langle 2' \rangle_i}{W_i} = d_2\{2\}. \tag{4.12}$$

Finally, the measured differential flow of D^0 meson is obtained as

$$v_2\{2\} = \frac{d_2\{2\}}{\sqrt{c_2\{2\}}}. \tag{4.13}$$

If the analysis had been done for directly observable particles (e.g. pions, kaons, and protons), the elliptic flow obtained from Eq. 4.13 would have been the final result. Nevertheless, for the case of particles reconstructed from their decay products, a correction on presence of the combinatorial background has to be done in order to gain the desired result - elliptic flow of D^0 meson.

Two different approaches were used for this correction. In the first one (used e.g. in [48]), the differential flow $d_2\{2\}$ is calculated for each candidate and subsequently filled to a TProfile as a function of invariant mass m_{inv} of Kπ pair. This variable contains both true signal (sig) and some combinatorial background (bkg), therefore it is labeled total differential flow.

Subsequently, the distribution $d_2^{\mathrm{tot}}\{2\}(m_{\mathrm{inv}})$ is fitted fit the function

$$d_2^{\mathrm{tot}}\{2\}(m_{\mathrm{inv}}) = f^{\mathrm{sig}}(m_{\mathrm{inv}}) d_2^{\mathrm{sig}}\{2\} + f^{\mathrm{bkg}}(m_{\mathrm{inv}}) d_2^{\mathrm{bkg}}\{2\}(m_{\mathrm{inv}}), \tag{4.14}$$

where $f^{\mathrm{sig}}(m_{\mathrm{inv}})$ and $f^{\mathrm{bkg}}(m_{\mathrm{inv}})$ is a fraction of signal and background, respectively, obtained as

$$f^{\mathrm{sig}}(m_{\mathrm{inv}}) = \frac{N^{\mathrm{sig}}}{N^{\mathrm{sig}} + N^{\mathrm{bkg}}}. \tag{4.15}$$

In the fit, the differential flow of pure signal $d_2^{\mathrm{sig}}\{2\}$ is fixed while the one of background $d_2^{\mathrm{bkg}}\{2\}$ is a function of invariant mass (linear dependence on m_{inv}). It is possible to fit

$d_2^{\rm bkg}\{2\}(m_{\rm inv})$ from the wrong sign combination of daughter particles with a linear function and fix parameters when fitting $d_2^{\rm tot}\{2\}$ with Eq. 4.14, however, we have left these parameters free because of presence of statistical fluctuations.

Bearing in mind the imporance of $f^{\rm sig}(m_{\rm inv})$ and $f^{\rm bkg}(m_{\rm inv})$ in the fit of $d_2^{\rm tot}\{2\}(m_{\rm inv})$, it is crucial to examine into details Eq. 4.15. $N^{\rm sig}$ and $N^{\rm bkg}$ is a number of signal and background, respectively. This functions are obtained from fitting the histogram of invariant mass of Kπ pairs that make D^0 candidates. Generally in heavy flavour physics, a Gaussian function is used to fit the signal. Thus, the essential is to choose the right function to fit the background.

The background (like-sign combinations of Kπ pairs) was fitted with 6 different functions - polynomial of degree 1 to 5 and the exponential function, with likelihood method as a fitting option. The distribution of invariant mass integrated over all $p_{\rm T}$ bins is shown in Fig. 4.14 together with results of fit of all chosen functions. The decision was made based on (shown) $\chi^2/_{ndf}$ parameter[4] Tests were done for both different binning and different $p_{\rm T}$ bins of D^0 candidate.

Analogically, the signal distribution was fitted with aforementioned functions + the Gaussian. As the fluctuations might have occurred, no parameter was fixed during this fit. Combining both results (for different binning and fitting options), we have decided to use the exponential function to describe the background. The invariant mass distribution of unlike-sign Kπ pairs in the first $p_{\rm T}$ bin ($1 < p_{\rm T}(D^0) < 2$ GeV/c) is shown in Fig. 4.15 together with the fit result.

The function obtained from the fit was used together with Eq. 4.14 to fit the distribution of $d_2\{2\}$ as a function of Kπ pair invariant mass, shown in Fig. 4.16. The individual parts of the fit (signal and background) are shown as well. It can be seen that the function does not describe the data properly, the relative error of the fit is more than 100%.

To further explore this variable, the distribution of the differential flow of for both unlike- and like-sign Kπ pairs is shown in Fig. 4.17. No trend can be seen, the data points have

[4] $\chi^2/_{ndf}$ stands for the ratio of the chisquare distribution and number of degrees of freedom. Practically, we want this number to be as close to 1 as possible.

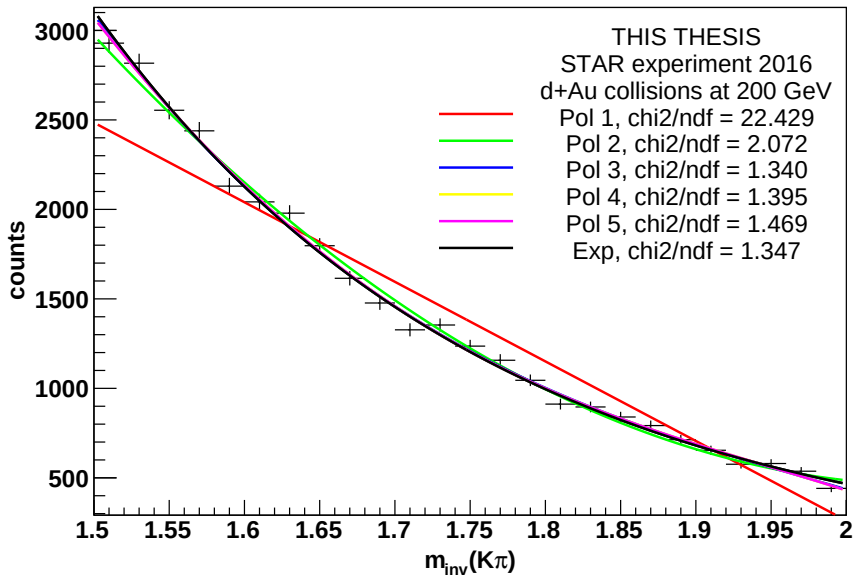

Fig. 4.14: Distribution of invariant mass of like-sign Kπ pairs with results of background fit.

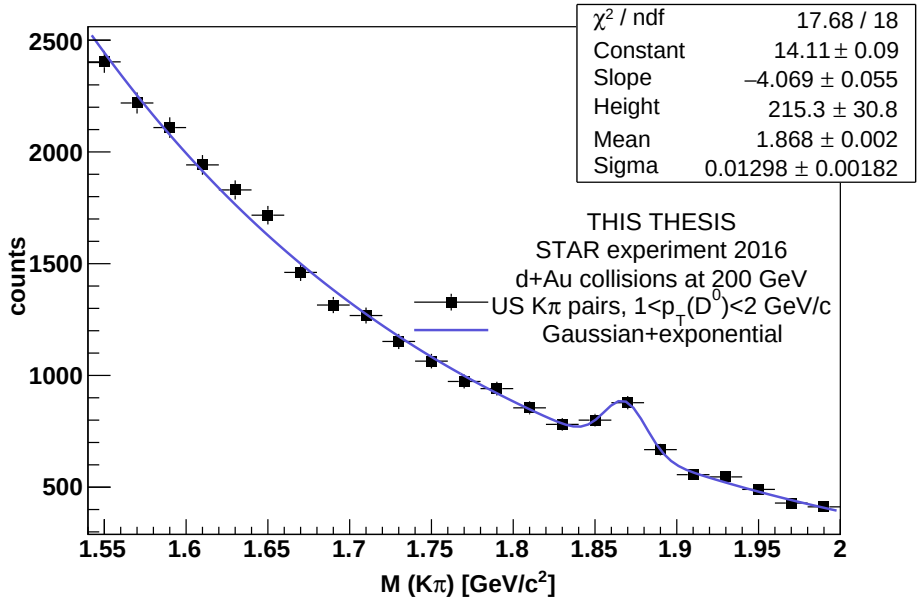

Fig. 4.15: Distribution of invariant mass of unlike-sign Kπ pairs together with a fit with Gaussian + exponential function in $1 < p_{\mathrm{T}}(\mathrm{D}^0) < 2$ GeV/c.

too large error bars, and there is no significant difference between unlike- and like-sign pairs. This is probably caused by very low available statistics, we had obtained only a very small

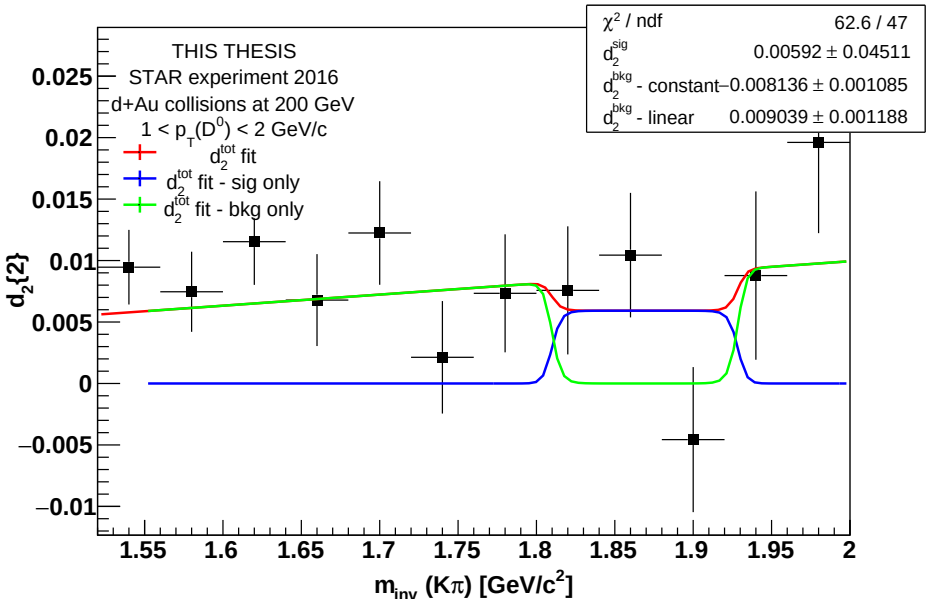

Fig. 4.16: Distribution of the differential flow of unlike-sign Kπ pairs in $1 < p_{\mathrm{T}}(\mathrm{D}^0) < 2$ GeV/c as a function of the pair invariant mass together with the fit.

amount of D^0 candidates.

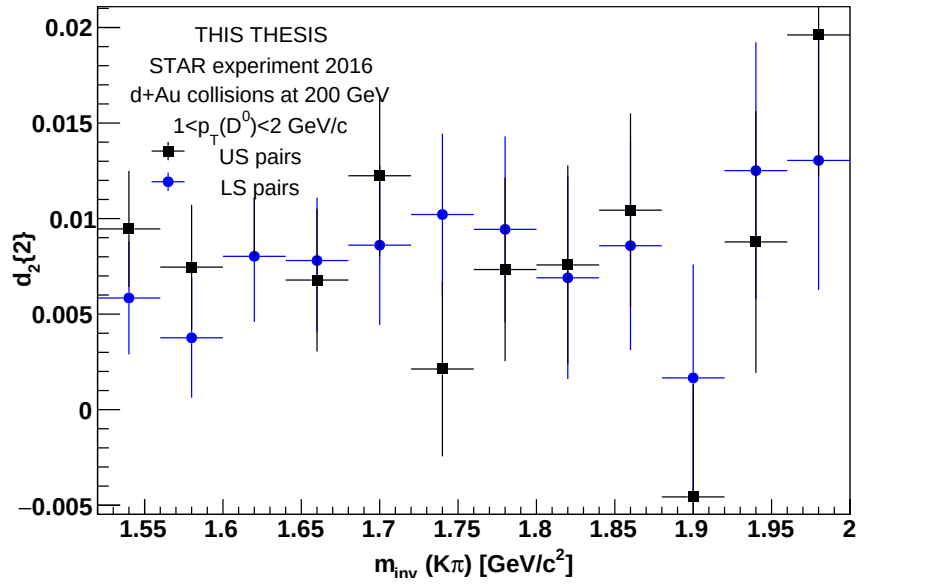

Fig. 4.17: Distribution of the differential flow of unlike- and like-sign Kπ pairs in $1 < p_{\mathrm{T}}(\mathrm{D}^0) < 2$ GeV/c as a function of the pair invariant mass.

The second approach that can be used to correct the presence of the residual background was used in D^0 analysis in Au+Au collisions at 200 GeV at the STAR experiment [38]. It uses values of $d_2\{2\}$ for both unlike- and like-sign combinations. The $d_2\{2\}$ for signal only is obtained as

$$d_2\{2\} = \frac{N_{\mathrm{US}}\, d_2^{\mathrm{US}}\{2\} - N_{\mathrm{LS}}\, d_2^{\mathrm{LS}}\{2\}}{N_{\mathrm{US}} - N_{\mathrm{LS}}}, \tag{4.16}$$

where US and LS stands for unlike- and like-sign charge combination pairs, respectively, and N_{US} and N_{LS} is a number of these pairs obtained from the integral of the Gaussian and the exponential function within $\pm 3\sigma$ around the mean value.

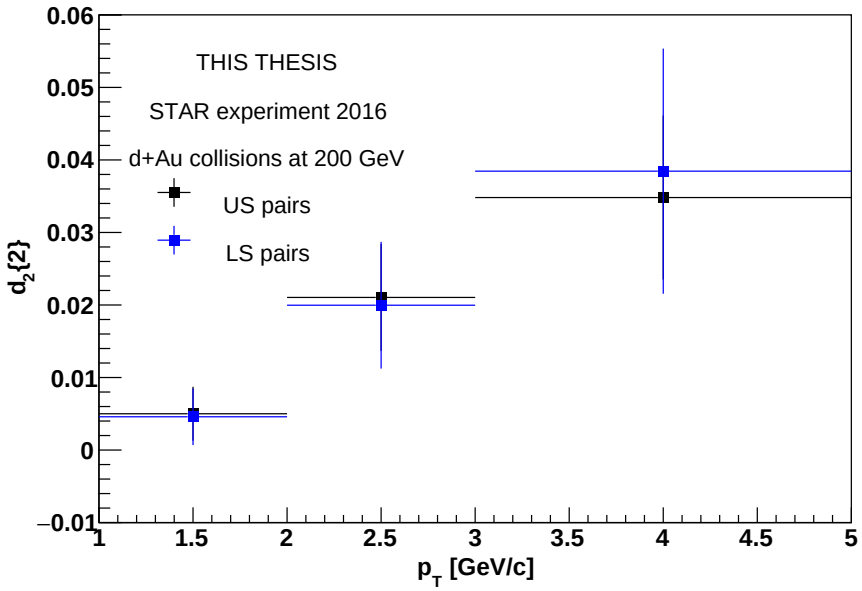

Fig. 4.18: The differential flow of unlike- and like-sign Kπ pairs as a function of $p_{\mathrm{T}}(\mathrm{D}^0)$.

The differential flow as a function of pair p_{T} for both unlike- and like-sign pairs is shown in Fig. 4.18. Only candidates within $\pm 3\sigma$ of the Gaussian mean from the fit of pair invariant mass were used to obtained these values.

Using Eq. 4.16, we have obtained the differential flow of D^0 meson. The uncertainty is combined from uncertainties of a number of signal, d_2^{US}, and d_2^{LS}, in analogy with [38]. The result for both methods is shown in Fig. 4.19. The uncertainty of the fitting method (from fitting d_2^{US} as a function of pair invariant mass) comes from the fit results.

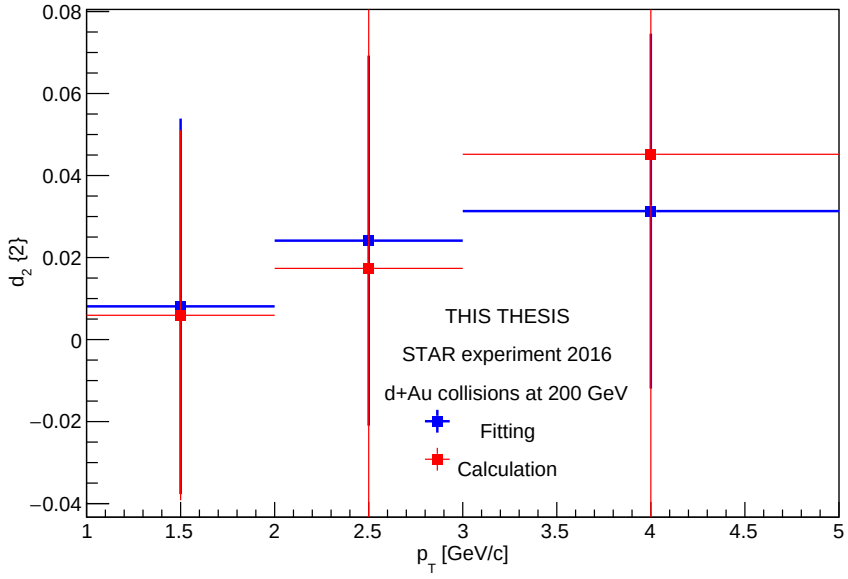

Fig. 4.19: The differential flow of D^0 meson obtained with two different methods as a function of p_{T}(D^0).

Values of both methods are in a very good accordance, however, their uncertainties are large, therefore it is not possible to make physics conclusions. As the fitting method has slightly smaller error bars, the final value of the elliptic flow has been obtained using differential flow from this method.

4.3 Elliptic flow of D^0 meson

Finally, the elliptic flow is shown in Fig. 4.20. It was obtained using Eq. 4.13, the uncertainty is combined from both differential and reference flow. In the calculation of errors, these two values were considered to be completely uncorrelated. Because of insufficient statistics, error bars are really big, with their relative values 762%, 408%, and 213%, respectively, for increasing p_{T} of the D^0. It is not possible to significantly improve this result without gaining more d+Au collisions or without a significant improvement of the signal-to-background ratio of D^0 candidates.

Nevertheless, in the first bin, the difference between d_2^{US} and d_2^{LS} is very small, causing the

value of $v_2\{2\}$ to be very close to 0,$v_2\{2\} = 0.069$ (the error is not considered). This result is similar to the elliptic flow of D^0 in Au+Au collisions at $\sqrt{s_{NN}} = 200$ GeV recorded with the STAR experiment in 2014 [38]. Data shown as well in Fig. 4.20 are for the centrality 0-80%. As the statistics has been much better compared to the analysis in d+Au collisions, calculated v_2 has much smaller uncertainty. The statistical error is in order of magnitude $v_2 = 0.01$. Therefore, error bars are not visible in this figure as the shown range is much larger.

The result in the first p_T bin is also similar to the one obtained by the CMS collaboration. The elliptic flow of the D^0 meson in p+Pb collisions at $\sqrt{s_{NN}} = 8.16$ TeV is shown in Fig. 4.21 together with the v_2 of light hadrons (K^s_0, Λ, Ξ^-, Ω^-). In the comparison between these two experiments, it is important to realize that the collision energy and the considered multiplicity is different in magnitude.

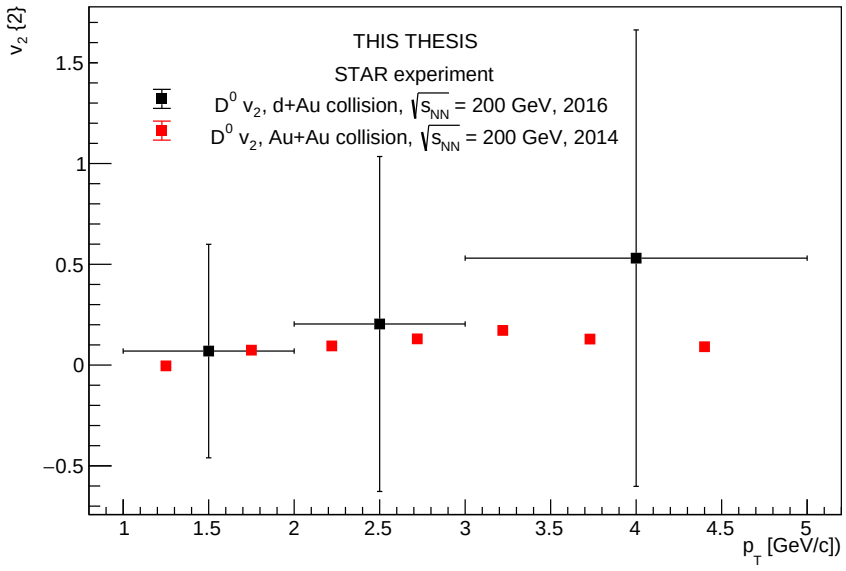

Fig. 4.20: The elliptic flow of D^0 meson as a function of $p_T(D^0)$ in d+Au and Au+Au collisions.

Moreover, the non-flow estimation has not been done in the presented analysis. It could be done with enlarging $|\Delta\eta|$, calculating a higher order of multi-particle correlation, or using a higher order of sub-event method. While we have used $|\Delta\eta| > 1.0$ in the comparison

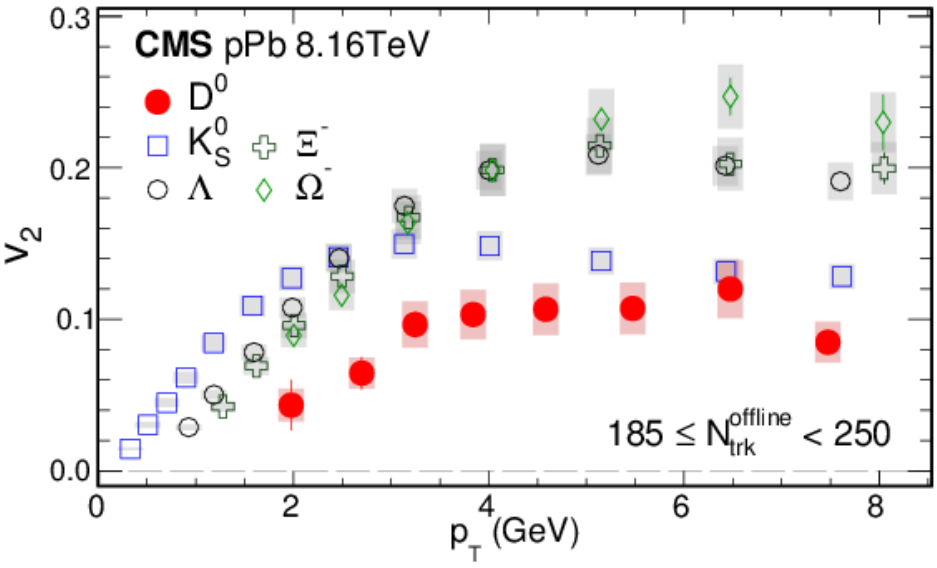

Fig. 4.21: The elliptic flow of D^0 meson compared with light hadrons in p+Pb collisions at $\sqrt{s_{\mathrm{NN}}} = 8.164$ TeV as a function of $p_{\mathrm{T}}(\mathrm{D}^0)$. Taken from [49].

with the reference flow measured with ALICE (Fig. 4.13), other parts of the analysis were calculated with $|\Delta\eta| > 0.15$ as the statistics was very low and we wanted to avoid losing more data. The further examination might be done concerning the optimal value of $|\Delta\eta|$. Analogically, a higher order of both multi-particle correlation and sub-event method is not possible because of the low statistics.

Conclusion

The aim of this thesis was to measure the elliptic flow of D^0 meson in d+Au collisions at $\sqrt{s_{\mathrm{NN}}} = 200$ GeV recorded with the STAR experiment in 2016. This currently hot topic is important as the elliptic flow which was believed to originate from the collective behavior of the medium after the heavy-ion collisions has been measured in small collisions systems such as p+p or p+Pb. Therefore it is important to investigate the origin of the flow in such systems to find out whether a quark-gluon plasma droplet is present or not. The multi-particle correlation method with generic framework has been used to fulfill this goal. The reconstruction of D^0 as well as the analysis method of flow signal is described in detail. The motivation of this analysis and the description of the STAR experiment is provided as well.

The reconstruction of D^0 meson has been done using its hadronic decay channel. Because of the significant presence of the combinatorial background, the boosted decision trees from TMVA package within the ROOT framework have been used. This machine learning algorithm has helped to essentially improve the signal significance. Its training has been done separately for in three bins of candidate's transverse momentum: 1 – 2, 2 – 3 a 3 – 5 GeV/c. The obtained significance has been 5.18, 7.40, and 8.39, respectively. A looser boosted decision trees cut value has been used for the flow analysis as the bigger data sample has been needed for such measurement.

Subsequently, the generic framework for the flow analysis using the multi-particle correlation method has been used. This approach was necessary because of the non-uniform detector acceptance. Firstly, the reference flow of charged particles has been calculated and is shown in this thesis as a function of the collision multiplicity. The result is in a good ac-

cordance in high multiplicity region with the result presented by the ALICE collaboration in p+Pb collisions. The differential flow of D^0 candidates, obtained with two different methods of combinatorial background subtraction, is shown and consistent within the uncertainty. However, uncertainties are huge because of the small data sample and the low signal-to-background ratio. This uncertainty has propagated to the final result of the elliptic flow od D^0 meson which has been obtained using both the reference and the differential flow calculated using the generic framework. Its final values is 0.069, 0.204, and 0.530, respectively, for all transverse momentum bins in increasing order. However, as stated, these results have a large uncertainty. A better result could be obtained with either a bigger data sample or with an improved signal-to-background ratio.

Additionally, the obtained result of the elliptic flow of D^0 meson in d+Au collisions at $\sqrt{s_{\mathrm{NN}}} = 200$ GeV at the STAR experiment has been compared to the same measurement in Au+Au collisions at $\sqrt{s_{\mathrm{NN}}} = 200$ GeV at the STAR experiment and with the elliptic flow of D^0 in p+Pb collisions at $\sqrt{s_{\mathrm{NN}}} = 8.16$ TeV at the CMS experiment. The result obtained in the first bin with the smallest candidate's transverse momentum (1 – 2 GeV/c) is similar to the both of these measurements. However, a conclusion cannot be made because of the present uncertainty.

It might be possible that in a high multiplicity p+Pb collision at the LHC at much higher energy a quark-gluon plasma droplet is created. However, the collision energy of d+Au collisions used for this analysis is lower in magnitude. Additionally, results obtained in this thesis are rather difficult for an interpretation as the uncertainty is too large. Therefore a final conclusion cannot be made out of the presented results.

The result of this work has been presented by the author at the STAR collaboration meeting in the Brookhaven National Laboratory in March 2019.

Bibliography

[1] M. Tanabashi et al. *The Review of Particle Physics.* Phys. Rev. D 98, C38, 2018.

[2] R. Vogt. *Ultrarelativistic Heavy-Ion Collisions.* Elsevier, 2007. ISBN 978-0-444-52196-5.

[3] R. Pasechnik and M. Šumbera. *Phenomenological Review on Quark-Gluon Plasma: Concepts vs. Observations.* Universe 2017, 3 no.1, 7.

[4] D. McDonald. *Overview of results from phase I of the Beam Energy Scan program at RHIC.* EPJ Web Conf., 95:01009, 2015.

[5] Z. Xu. *BUR 2019 and long-term plan.* STAR Collaboration Meeting, 2019.

[6] J. F. Grosse-Oetringhaus. *Introduction to Heavy-Ion Physics.* CERN Summer Student Lectures, 2018.

[7] P. Rosnet. *Quark-Gluon Plasma: from accelerator experiments to early Universe.* 2015. arXiv:1510.04200.

[8] T. Lenzi. *Development and Study of Different Muon Track Reconstruction Algorithms for the Level-1 Trigger for the CMS Muon Upgrade with GEM Detectors.* 2013.

[9] R. Snellings. *Elliptic Flow: A Brief Review.* New J. Phys., 13:055008, 2011.

[10] S. Sarkar et al. *The Physics of the Quark-Gluon Plasma: Introductory Lectures.* Springer Berlin Heidelberg, 2009. ISBN 978-3-642-02286-9.

[11] W. Fischer. *RHIC upgrades and capabilities for the next decade.* 2016. BNL-112754-2016-CP.

[12] J. Adams et al. *Evidence from d + Au measurements for final state suppression of high p(T) hadrons in Au+Au collisions at RHIC.* Phys. Rev. Lett., 91:072304, 2003.

[13] Yuri L. Dokshitzer et al. *On specific QCD properties of heavy quark fragmentation ('dead cone').* J. Phys., G17:1602–1604, 1991.

[14] J. Adam et al. *Centrality and transverse momentum dependence of D^0-meson production at mid-rapidity in Au+Au collisions at $\sqrt{s_{\rm NN}} = 200\,\text{GeV}$.* Phys. Rev., C99(3):034908, 2019.

[15] J. Adam et al. *Transverse momentum dependence of D-meson production in Pb-Pb collisions at $\sqrt{\rm s_{NN}} = 2.76$ TeV.* JHEP, 03:081, 2016.

[16] T. Matsui and H. Satz. *J/ψ Suppression by Quark-Gluon Plasma Formation.* Phys. Lett., B178:416–422, 1986.

[17] Helmut Satz. *Colour deconfinement and quarkonium binding.* J. Phys., G32:R25, 2006.

[18] W. Florkowski. *Phenomenology of Ultra-Relativistic Heavy-Ion Collisions.* Singapore, Singapore: World Scientific (2010) 416 p, 2010.

[19] U. Heinz. *The strongly coupled quark–gluon plasma created at RHIC.* Journal of Physics A: Mathematical and Theoretical, 42(21):214003, 2009.

[20] K. Aamodt et al. *Elliptic Flow of Charged Particles in Pb-Pb Collisions at $\sqrt{s_{\rm NN}} = 2.76\,\text{TeV}$.* Phys. Rev. Lett., 105:252302, 2010.

[21] A. Adare et al. *Measurements of mass-dependent azimuthal anisotropy in central p+Au, d+Au, and ^{3}He+Au collisions at $\sqrt{s_{_{NN}}} = 200$ GeV.* Phys. Rev., C97:064904, 2018.

[22] K. Nagashima. *PHENIX measurements of heavy quark anisotropic flow in Au+Au and d+Au collisions at $\sqrt{s_{\rm NN}}$=200 GeV.* PoS, HardProbes2018:166, 2018.

[23] A. Andronic et al. *Heavy-flavour and quarkonium production in the LHC era: from proton-proton to heavy-ion collisions.* Eur. Phys. J., C76(3):107, 2016.

[24] BNL. *Brookhaven National Laboratory.* https://www.bnl.gov. Online, accessed 14 April 2019.

[25] Nobelprize.org. *The official web site of the Nobel Prize.* https://www.nobelprize.org/. Online, accessed 14 April 2019.

[26] J. Alessi. *Electron Beam Ion Source (EBIS) pre-injector project - Conceptual Design Report.* 2005. BNL-73700-2005-IR.

[27] M. Okamura and T. Kanesue. *Commissiong of the Laser Ion Source for RHIC EBIS.* RIKEN Accel. Prog. Rep, 48, 2015.

[28] E. Beebe et al. *Reliable operation of the Brookhaven EBIS for highly charged ion production for RHIC and NSRL.* 2014. BNL-105887-2014-CP.

[29] W. Wong and Y. Y. Lee. *Design and construction status of the AGS Booster accelerator.* 1988. BNL-41030.

[30] W. W. Mackay et al. *AGS to RHIC transfer line: Design and commissioning.* Conf.Proc. C960610, 2376-2378, 1996.

[31] W. Fischer. *Run overview of the Relativistic Heavy Ion Collider.* http://www.agsrhichome.bnl.gov/RHIC/Runs/, 2018. Online, accessed 15 April 2019.

[32] I. Alekseev et al. *Configuration Manual Polarized Proton Collider at RHIC.* https://www.bnl.gov/cad/accelerator/docs/pdf/RHICPPCMan.pdf. Online, accessed 15 April 2019.

[33] BNL. *The STAR experiment.* https://www.star.bnl.gov. Online, accessed 14 April 2019.

[34] PHENIX Collaboration. *sPHENIX: An Upgrade Proposal from the PHENIX Collaboration.* 2014. arXiv:1501.06197.

[35] S. Radhakrishnan. *Measurements of open charm and bottom production in 200 GeV Au+Au collisions with the STAR experiment at RHIC.* Quark Matter Conference, 2018.

[36] STAR Collaboration. *STAR Project Conceptual Design Report Update.* https://www.star.bnl.gov/public/tpc/notebooks/StarCDR.pdf, 1993. Online, accessed 18 April 2019.

[37] D. Beavis et al. *The STAR Heavy Flavor Tracker - Technical Design Report.* https://drupal.star.bnl.gov/STAR/system/files/HFT_TDR_Final.doc, 2011. Online, accessed 20 April 2019.

[38] L. Adamczyk et al. *Measurement of D^0 azimuthal anisotropy at mid-rapidity in Au+Au collisions at $\sqrt{s_{\mathrm{NN}}} = 200\,GeV$.* Phys. Rev. Lett., 118(21):212301, 2017.

[39] STAR Collaboration. *The STAR Time Projection Chamber: A Unique Tool for Studying High Multiplicity Events at RHIC.* Nucl. Instrum. Meth., A499:659–678, 2003.

[40] STAR Collaboration. *Technical Design Report for the iTPC Upgrade.* https://drupal.star.bnl.gov/STAR/files/TDRiTPCUpgrade_final.pdf, 2015. Online, accessed 20 April 2019.

[41] STAR Collaboration. *Proposal for a Large Area Time of Flight System for STAR.* http://www.star.bnl.gov/~ruanlj/MTDreview2010/TOF_20040524.pdf, 2004. Online, accessed 20 April 2019.

[42] W. J. Llope et al. *The TOF p/p VPD Time-Of-Flight System for STAR.* Nuclear Instruments and Methods in Physics Research Section A: Accelerators, Spectrometers, Detectors and Associated Equipment, 522(3):252 – 273, 2004.

[43] J. Vaněk. *Production of $D^{\pm}$ Mesons in Au+Au Collisions at $\sqrt{s_{NN}}$ = 200 GeV measured by the STAR Experiment.* Quark Matter Conference, 2018.

[44] A. Hoecker et al. *TMVA 4: Toolkit for Multivariate Data Analysis with ROOT, Users Guide.* 2013. arXiv:0703039.

[45] A. Bilandzic et al. *Flow analysis with cumulants: Direct calculations.* Phys. Rev., C83:044913, 2011.

[46] A. Bilandzic et al. *Generic framework for anisotropic flow analyses with multiparticle azimuthal correlations.* Phys. Rev., C89(6):064904, 2014.

[47] S. Acharya et al. *Investigations of anisotropic flow using multi-particle azimuthal correlations in pp, p-Pb, Xe-Xe, and Pb-Pb collisions at the LHC.* 2019. arXiv:1903.01790.

[48] V. Pacík. *Elliptic flow coefficients of identified hadrons in pp and p-Pb collisions measured with ALICE* . Quark Matter Conference, 2018.

[49] A. M. Sirunyan et al. *Elliptic flow of charm and strange hadrons in high-multiplicity pPb collisions at $\sqrt{s_{\mathrm{NN}}}$ = 8.16 TeV.* Phys. Rev. Lett., 121(8):082301, 2018.

Appendix

The distribution of invariant mass of Kπ pair is shown for two different bins of D^0 candidate's transverse momentum: $2 < p_T(D^0) < 3$ GeV/c and $3 < p_T(D^0) < 5$ GeV/c. The first set of figures is with BDT cut selected to obtain the highest possible significance, the second one is used for the elliptic flow calculation (higher raw yield).

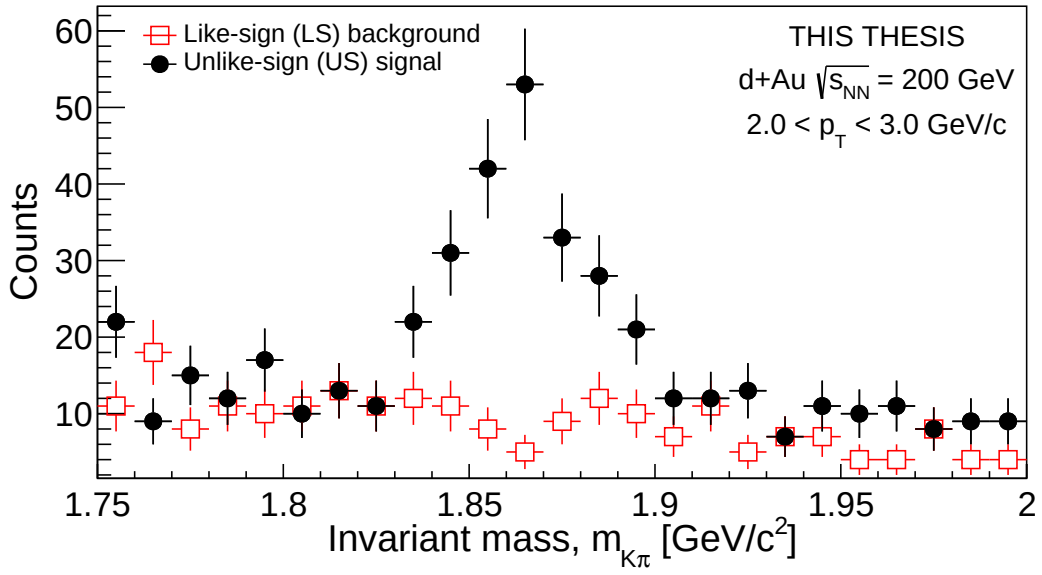

(a) Unlike- and like-sign Kπ pairs.

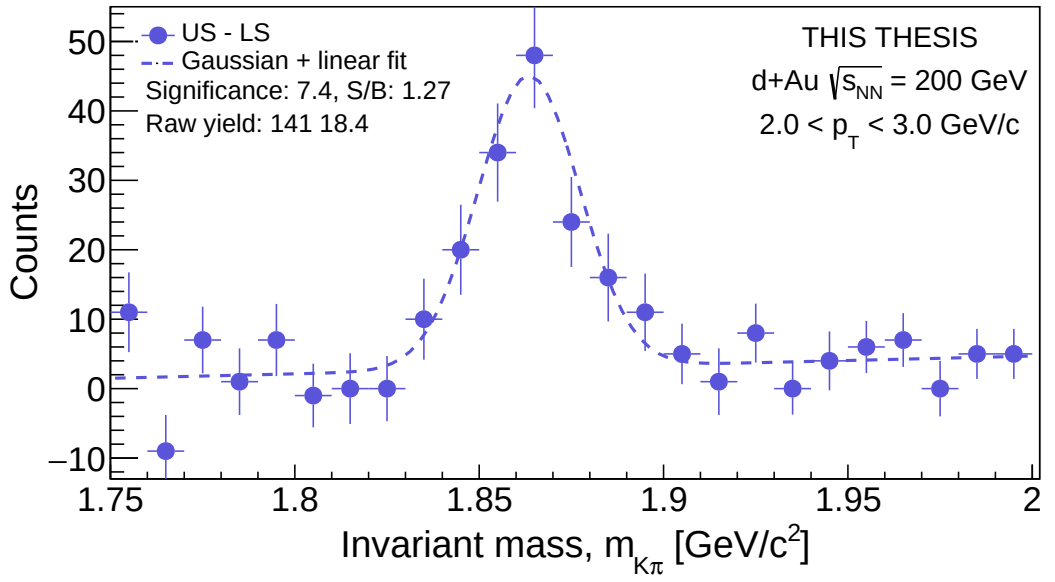

(b) Subtracted distribution together with the fit with Gaussian + linear function.

Fig. A.1: Distribution of invariant mass of Kπ pairs in the p_{T} bin $2 < p_{\mathrm{T}}(\mathrm{D}^0) < 3$ GeV/c with BDT cut value 0.299.

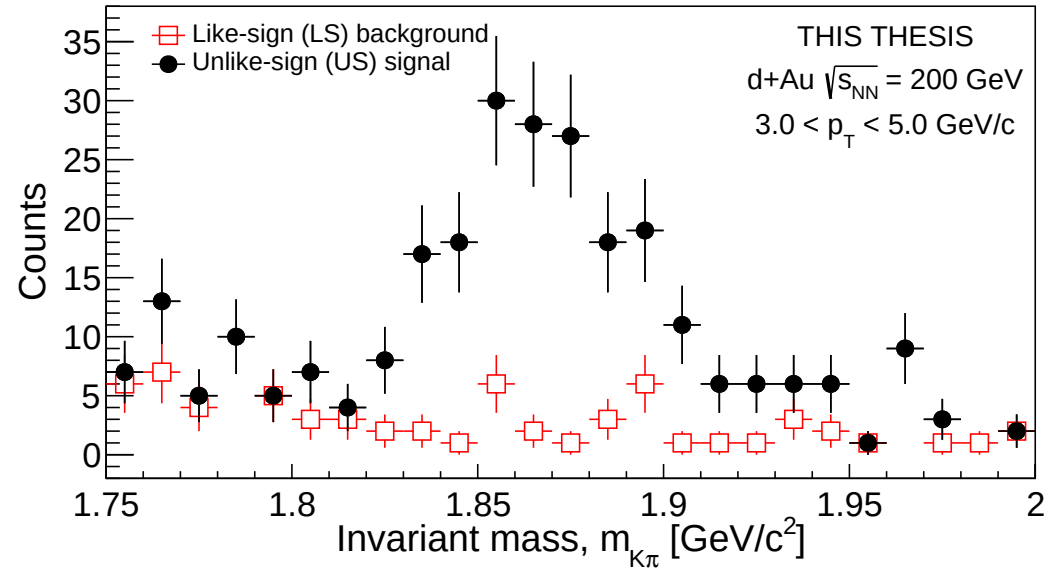

(a) Unlike- and like-sign Kπ pairs.

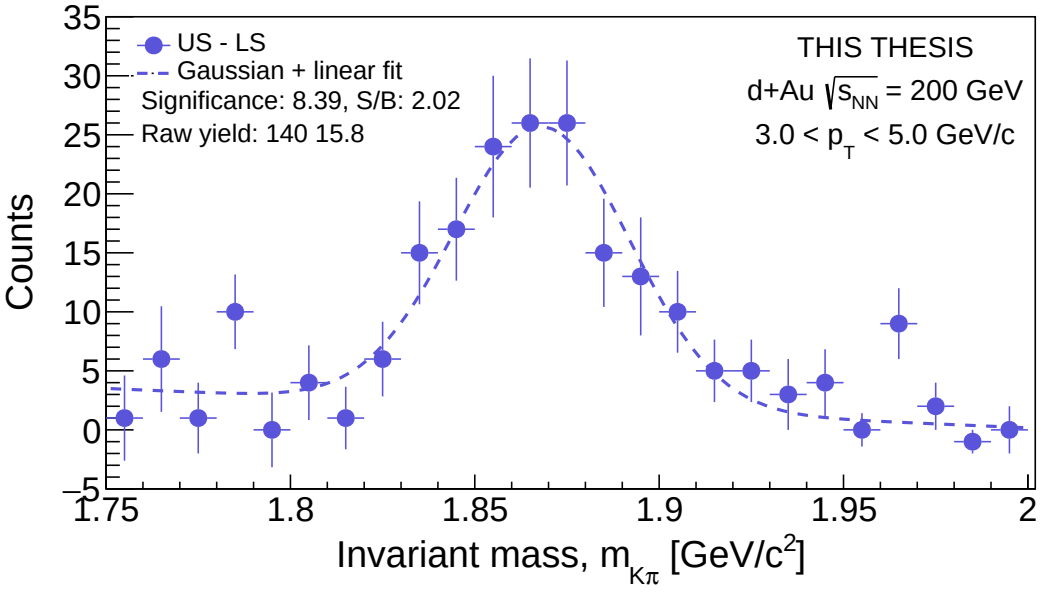

(b) Subtracted distribution together with the fit with Gaussian + linear function.

Fig. A.2: Distribution of invariant mass of Kπ pairs in the p_{T} bin $3 < p_{\mathrm{T}}(\mathrm{D}^0) < 5$ GeV/c with BDT cut value 0.288.

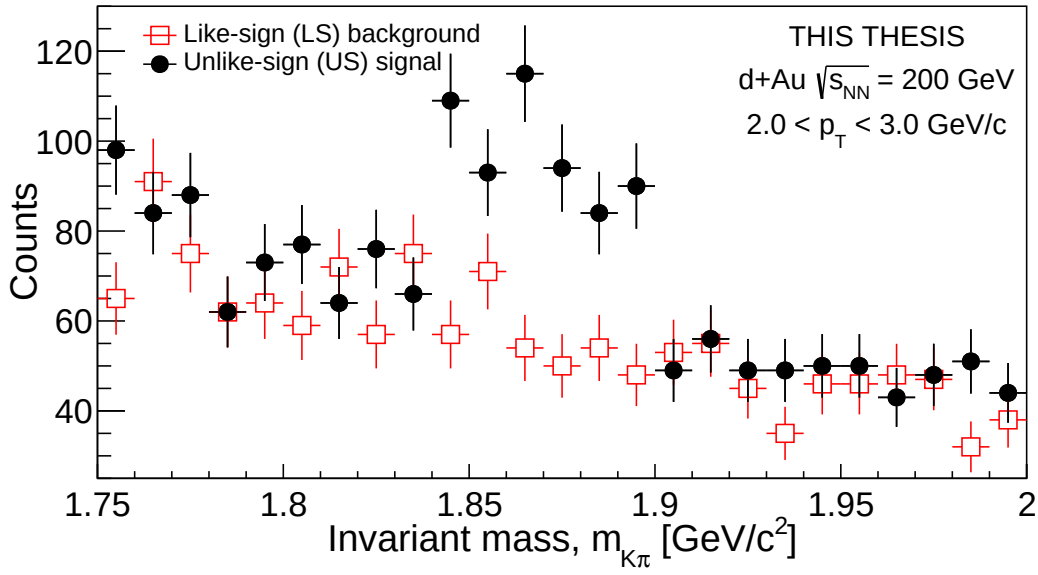

(a) Unlike- and like-sign Kπ pairs.

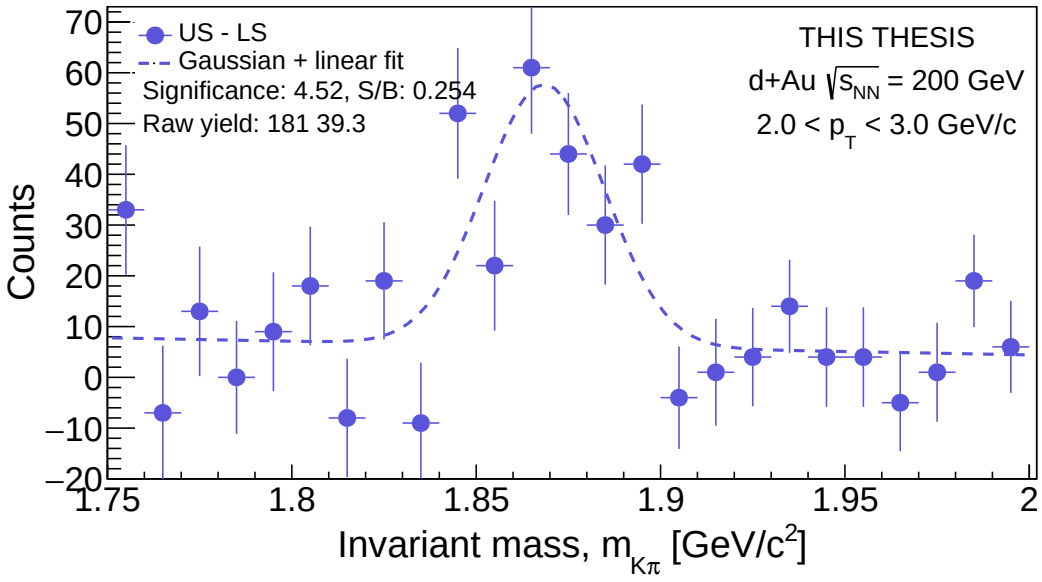

(b) Subtracted distribution together with the fit with Gaussian + linear function.

Fig. A.3: Distribution of invariant mass of Kπ pairs in the p_{T} bin $2 < p_{\mathrm{T}}(\mathrm{D}^0) < 3$ GeV/c with BDT cut value 0.2.

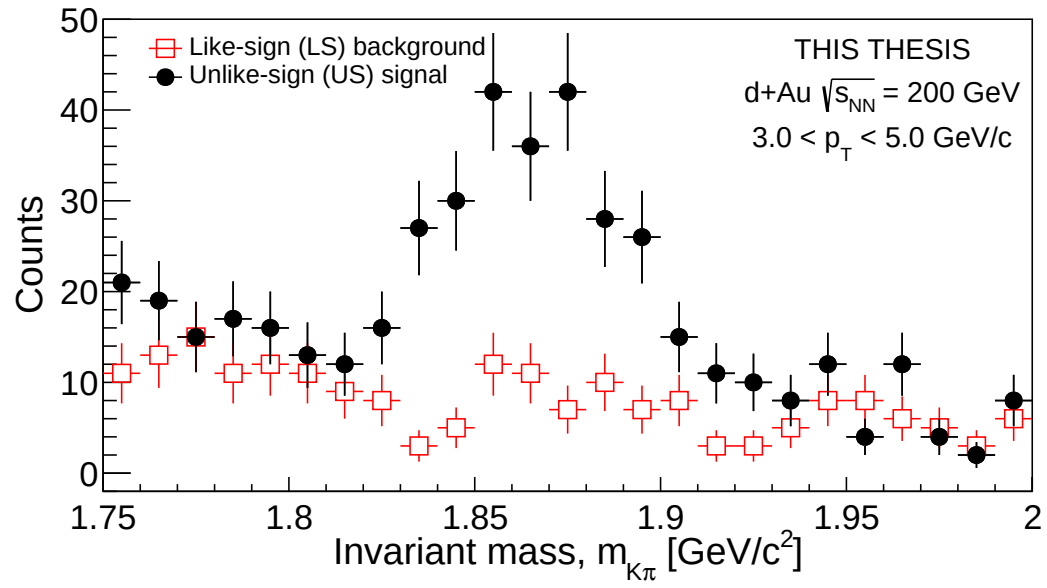

(a) Unlike- and like-sign Kπ pairs.

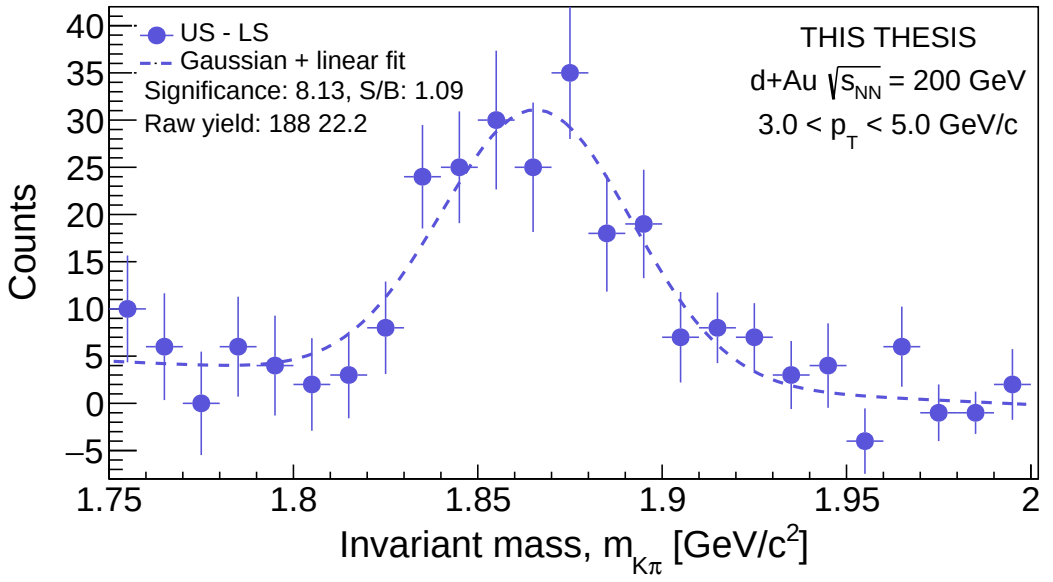

(b) Subtracted distribution together with the fit with Gaussian + linear function.

Fig. A.4: Distribution of invariant mass of Kπ pairs in the p_{T} bin $3 < p_{\mathrm{T}}(\mathrm{D}^0) < 5$ GeV/c with BDT cut value 0.22.